Analysis and Design of a Stationary Magnetic Abrasive Finishing System

by

Thamir Al-Dulaimi

A thesis
Presented to the University of Waterloo
in fulfillment of the
thesis requirement for the degree of
Doctor of Philosophy
in
Mechanical and Mechatronics Engineering

Waterloo, Ontario, Canada, 2018

Examining Committee Membership

The following served on the Examining Committee for this thesis. The decision of the Examining Committee is by majority vote.

External Examiner	Name: Ibrahim Deiab Title: Professor
Supervisor	Name: Behrad Khamesee Title: Professor
Internal Member	Name: Sanjeev Bedi Title: Professor
	Name: William Melek Title: Professor
Internal-external Member	Name: Eihab Abdel-Rahman Title: Professor

Author's Declaration

I hereby declare that I am the sole author of this thesis. This is a true copy of the thesis, including any required final revisions, as accepted by my examiners.

I understand that my thesis may be made electronically available to the public.

Abstract

Magnetic Abrasive Finishing (MAF) is a very effective technique used in precision surface finishing and polishing processes. It is defined as one of the advanced and nonconventional finishing processes, which is used to improve the characteristics of a finished surface. This technique utilizes a macro-size mixture of iron and abrasive particles moving in a magnetic field to remove material from a workpiece surface at the Nano or Micro scale. The MAF process can produce a finished surface by means of relative motion between a magnetic abrasive and the workpiece surface. The magnetic abrasive is suspended in a magnetic field which is generated by the electromagnets located underneath the workpiece.

In this study, a finishing apparatus using a rotating magnetic field, with stationary electromagnets and workpiece, is developed for surface finishing. This system utilizes a rotating magnetic field to control the magnetic force and dynamic motion of a macro-size mixture of iron and abrasive particles. As opposed to conventional finishing processes, this approach eliminates any mechanical motion of the electromagnets and the workpiece, to make the system more controllable and reliable. The mechanism and characteristics of this system are summarized in this study. The finite element method is used to analyze the magnetic flux distribution, magnetic flux density, and magnetic force in the working area. Thus, this study conducts a novel design based on using stationary equipment and a finishing process carried out by regulation of magnetic field. In this design, the magnetic field rotates where the other parts are stationary (the electromagnets and also the workpiece). Consequently, regulating the magnetic field is used to control the magnetic force, which represents the cutting force. This enhances the accuracy and controllability of the process and improves the quality of the final product; and it also can be considered a trial to reduce the mechanical power consumption by eliminating any mechanical motion.

Further, an optimization approach is used to determine the optimum design configuration of the electromagnet to maximize the finishing force in the working zone. The optimum dimensions are then used in the fabrication process of the electromagnets for the finishing system setup. Accordingly, experiments are also carried out to finish different materials such as, titanium, aluminum, composite material, polyurethane and Polytetrafluoroethylene (PTFE). The Taguchi systematic technique is used to design the experiments to optimize the process parameters of the finishing process. The Stationary Magnetic Abrasive Finishing (SMAF) process setup of the optimal electromagnet configuration is applied to finish a titanium (CP Grade 2) specimen and the average surface roughness (Ra) is improved from 4.156 µm to 1.94 µm. Also the variation of temperature in the interfering zone between the Titanium specimen and the magnetic abrasive particles is measured using a thermal camera. The measurement shows that the variation during the operation running time (60 mins) is just 14˚C, with temperature change from (23 – 37˚C). This change has an insignificant effect on the surface characteristics and quality.

Moreover, a proposed approach is conducted to measure the magnetic force applied on particles. The experimental results of the force measurement are compared with the finite element simulation results. It is shown that there is good agreement between these results, with an average error percentage of 3.5%.

Acknowledgements

I would like to I would like to thank my supervisor, Dr. Mir Behrad Khamesee for the support and motivation he has provided me throughout the years of my PhD study. I would also like to show gratitude to my committee members: Dr. Sanjeev Bedi, Dr. William Melek, and Dr. Eihab Abdel-Rahman. I would also like to thank my external examiner Dr. Ibrahim Deiab for attending my defense. I want to thank my colleagues Mohammad Al-Mashagbeh, David M. B. Dombroski, Moein Mehrtash, Xiaodong Zhang, Yuze Huang, Ehsan Asadi, Hassan Askari, Roberto Ribeiro, and Heng Zhang for the help in my research. My thanks also to Dr. James Tung, Dr. Usman Ali, Dr. Issam Aljubury and Chi-Hsiang Liao for their support.

My sincere thanks to my parents, my brothers and my sisters, I'm greatly thankful to their kind support.

My deep thanks of gratitude to my wife, my daughters; Rahma and Marya, and my son Abdulrahman for their encouragement and support. I would like to say this success is a result of their dedicated effort.

This research has been supported by University of Baghdad/ Baghdad/ Iraq, my sincere gratitude to them.

Table of Contents

Author's Declaration ..... **iii**
Abstract ..... **iv**
Acknowledgements ..... **vi**
Table of Contents ..... **vii**
List of Figures ..... **xi**
List of Tables ..... **xvi**
Chapter 1 ..... **1**
Introduction **1**
1.1. Background 1
1.2. Overview of Abrasive Finishing Processes (AFP) 2
1.2.1. Process Principles Classification 3
1.2.2. Abrasive Particle State Classification 4
1.3. Material removal mechanism in Abrasive Finishing Processes 5
1.4. Magnetic Abrasive Finishing 7
1.5. Surface Roughness terminology 9
1.6. The proposed system overview 11
1.7. Thesis Objectives and Outlines 12
1.8. Thesis Contributions 14
Chapter 2 ..... **16**
Literature Review **16**
2.1. Introduction 16
2.2. Permanent Magnet 16
2.3. Electromagnets 19
2.3.1. Electromagnet with Direct Current (DC): 19
2.3.2. Electromagnet with Alternating Current (AC): 21
2.4. Conclusion and Motivation 21
Chapter 3 ..... **23**
Experimental Setup **23**
3.1. Introduction 23
3.2. Controlling and MATLAB-Simulink 23

3.2.1. Control and Communication Setup 23
3.2.2. Simulink - Pulse Width Modulation (PWM) 28
3.2.3. Simulink for Four-Coil Configuration 32
3.3. Coils Configuration 36
3.3.1. Three-Coils Configuration 36
3.3.2. Four-Coil Configuration 37
3.4. System Setup 39
3.5. Experimental Outcomes using Four-Coils Configuration 40
3.6. Conclusions 41
Chapter 4 43
Design and Optimization of Electromagnetic Actuator 43
4.1. Introduction 43
4.2. Modeling and Electromagnet Parametric Optimization 44
4.2.1. Governing Equations and Magnetic Force 44
4.2.2. Electromagnet Design 46
4.2.3. Thin shell finite solenoid formula 48
4.2.4. Finite element simulation 49
4.3. Verification of optimization results 51
4.4. Best alignment angle of the electromagnets 54
4.5. Geometry of the extended core 56
4.6. Magnetic Force Measurement 59
4.7. Experimental Results 62
4.8. Temperature Variation 63
4.9. Conclusions 65
Chapter 5 66
System Modeling 66
5.1. Introduction 66
5.2. System Description 66
5.3. Finite Element Model 68
5.4. Magnetic Field Analysis 70
5.5. Electromagnets configuration setup 77
5.5.1. Magnetization effect on the magnetic field 78
5.5.2. Best configuration of the electromagnets to maximize B_{xy} component 79

5.6. Analysis of cutting forces and metal removal 81
5.6.1. Modeling of the normal component (F_{mz}) 82
5.6.2. Modeling of the Tangential component (F_{mt}) 85
5.6.3. Modeling of abrasive particle 85
5.7. Metal Removal 89
5.8. Conclusion 91
Chapter 6 93
Fuzzy Logic Prediction Model 93
6.1. Introduction 93
6.2. Experiments Parameters 94
6.3. Taguchi Method 96
6.4. Fuzzy Logic 97
6.5. Membership Function 100
6.6. Structure of Fuzzy Rules 103
6.7. Defuzzification 105
6.7.1. Mean of Maximum (MOM) 105
6.7.2. Center of Area (COA) 106
6.8. Results 106
6.9. Fuzzy logic Model Accuracy and Error 110
6.10. Parametric Effects 111
6.10.1. Applied Voltage 112
6.10.2. Frequency of electromagnet energizing 112
6.10.3. Operating Time 113
6.10.4. Particle Size 114
6.11. Conclusions 114
Chapter 7 115
Implementations of SMAF Technique 115
7.1. Introduction 115
7.2. Thin Film Material 115
7.3. Composite Material 117
7.4. Internal Surface of a Thin Tube 118
7.5. Tiny Channels 119
7.6. Special Materials 121

7.6.1. Titanium 121
7.6.2. Inconel 122
7.7. Conclusion 123
Chapter 8 124
Conclusions and Future Work 124
8.1. Thesis Conclusions 124
8.2. Future research 126
References 127
Appendix A 135
List of Publications 135
Appendix B 136
On-axis and off-axis Magnetic Field Formula 136
Appendix C 140
Experimental results 140

List of Figures

Figure 1.1: Classifications of Abrasive Finishing Processes (AFP) [9]…….... 2

Figure 1.2: Schematic of Grinding Process as an Example of a Motion-Copying-Process……..3

Figure 1.3: Schematic of Pressure-Copying-Processes Examples……4

Figure 1.4: Schematic of AFP Finishing Conditions…… 6

Figure 1.5: Schematic Illustrates the Interaction Phases of Abrasive Particle (a) Kinematics of Abrasive, (b) Finishing Force Components on the Abrasive, (c-e) Interaction Phases Between Abrasive and Workpiece Surface (Reproduced From [9])……6

Figure 1.6: Model of a Single Abrasive Particle Scratching (Reproduced from [12])…… 7

Figure 1.7: Examples of Existing Maf Methods, (a): Fixed Magnetic Source with Rotated Work Piece Internal Surface Finishing. (b): Fixed Magnetic Source with Rotated Work Piece External Surface Finishing. (c): Rotated Magnetic Source with Fixed Work Piece……8

Figure 1.8: Microscopy and Scanning Electron Microscopy of (a) Iron Particle (Dia. 150~300 μm), and (b) White Alumina (Wa) Magnetic Abrasive (Mean Dia. 80 μm, Aluminum Oxide (Al2o3): ≤10 μm) [7]……9

Figure 1.9: Schematic of Surface Profile and Roughness (Reproduced from [17])…….. 10

Figure 2.1: Configuration of Magnetic Abrasive Flexible Brushes (MAFB) [24]…… 17

Figure 2.2: Flexible Magnetic Brush and Dispersion of Magnetic Force [28]……... 17

Figure 2.3: Schematic of Processing Principle and Photograph of Experimental Setup with Double Pole-Tip Sets [31]…… 18

Figure 2.4: Vibration-Assisted Magnetic Abrasive Finishing Setup [37]…….. 20

Figure 2.5: Schematic of Processing Principle And Photographs of Finishing Surface [6]…….....21

Figure 3.1: Flow Chart of the Control and Communication Setup……23

Figure 3.2: System Components…… 24

Figure 3.3: Residual Magnetism Shown with Particles Sticking to the Coil Core…… 25

Figure 3.4: B-H Curve of Hysteresis Loop for a Ferromagnetic Material [44]…….. 25

Figure 3.5: L298 – Multiwatt 15 Dual Full-Bridge Driver……26

Figure 3.6: Pre-Programmed Functions Block for the Chip L298……..27

Figure 3.7: Pulse Width Modulation [46]……... 28

Figure 3.8: Simulink Block Diagram for PWM……. 29

Figure 3.9: Zoom-in the First Segment of PWM Block Diagram…….. 30

Figure 3.10: Input Breakdown for Switch Function……..... 30

Figure 3.11: Screen Shot of Analog Wave and Outputs of Switch Block…… 30

Figure 3.12: Zoom-in Second Segment of PWM Block Diagram……...31
Figure 3.13: Four-Coil Configuration Hanging Above Maps…… 32
Figure 3.14: Two-Coils Hanging Above Maps……33
Figure 3.15: Simulink Block Diagram for Four-Coil Configuration……...34
Figure 3.16: Amount of Particles Resting on the Core of the Coil Due to the Residual Magnetism….. 34
Figure 3.17: Three-Coils in Linear Alignment…… 36
Figure 3.18: Three-Coils in Triangular Alignment…… 37
Figure 3.19: Four-Coils in Horizontal Configuration……. 37
Figure 3.20: Four-Coils with Extended Core…… 38
Figure 3.21: Six-Coil Configuration……... 38
Figure 3.22: Schematic of the Smaf Apparatus…….. 39
Figure 3.23: Four-Coil Configuration, (a) Coils Hang Under The Workpiece and Maps, (b) Coils are Located Above the Workpiece…….. 40
Figure 3.24: Sem Photographs of the Surface Before and After the Maf Process……..41
Figure 4.1: Basic Parameters of the Finite Solenoid……45
Figure 4.2: Verification of *B* with Different Values of *I*…….. 47
Figure 4.3: Magnetic Gradient Versus the Parameters of Coil Geometry A and B……..48
Figure 4.4: Magnetic Flux Distribution Contour for Iron Core and Iron Particle……..... 49
Figure 4.5: The Coil Parameters (With Iron Core)……... 52
Figure 4.6: The Value of Fabry Factor for a Uniform Current Density Coil [59]……..... 53
Figure 4.7: Schematic of Electromagnet Aligned with Angle Θ from Z Axis……. 54
Figure 4.8: The Variation of Force Components with Respect to Angle Θ…… 55
Figure 4.9: The Variation of Force Components, the Tangential (*Fxy*) and the Normal (*Fz*) with Respect to Angle Θ…… 55
Figure 4.10: Magnetic Particles Found to Be Outside of the Working Area…… 56
Figure 4.11: The Effect of the Core Tip Fillet Radius on B. (a) R = 0, (b) R = 4 Mm, (c) R = 8 Mm. 57
Figure 4.12: Variation of Magnetic Force in the Working Area with Respect to the Geometry of the Extended Core (a) Cylindrical Geometry, (b) Cylindrical -Chamfered Geometry, and (c) Square-Chamfered Geometry…… 58
Figure 4.13: Variation of Magnetic Force in the Working Area with Respect to the Air Gap Distance58
Figure 4.14: Optimum Dimensions of the Electromagnet Parameters……... 59
Figure 4.15: Optimum Configuration of the System Setup…… 59
Figure 4.16: Force Measurement Experimental Setup……60

Figure 4.17: A Comparison of Magnetic Force Versus Excitation Current for Different Axial Air Gaps Based on Experimental Force Measurement and *Fem* Results…… 61
Figure 4.18: Schematic of the Smaf Proposed System…….. 62
Figure 4.19: 3D Photographs of Polished Surfaces (a) Before and (b) After the Finishing Process…. 63
Figure 4.20: Thermal Images of Titanium Cp Grade 2 Sample at Different Times During the Finishing Process……... 64
Figure 5.1: System Description…… 66
Figure 5.2 : The Electromagnetic Coils Alignment……... 67
Figure 5.3: The Physical System Setup…… 67
Figure 5.4: Magnetic Field Components *Bz* and *Bx* of Different Distance above the Electromagnet Coil (From 1mm-5mm), Air-Core……71
Figure 5.5: Magnetic Field Components *Bz* and *Bx* for Different Distance above the Electromagnet Coil (from 1-5mm), Iron - Core……..…71
Figure 5.6: Photograph of the Setup Used to Measure *B*, 1) 3-D Position Motor of Micromanipulator. 2) Mp-285 Controller. 3) Electromagnet (Air Core Shown). 4) Gauss Meter Probe. 5) Motorized Micromanipulator. 6) Power Supply. 7) Gauss Meter…….. 72
Figure 5.7: Electromagnet with/without Iron Core, and Assembled…… 72
Figure 5.8 : *Bx* Component for Electromagnet with/without Iron Core, (A) Air-Core, (B) Iron-Core, (C) Factor (B Iron/B Air), (D) Average Factor Curve……... 73
Figure 5.9: *Bz* Component for Electromagnet with/without Iron Core, (a) Air-Core, (b) Iron-Core, (c) Factor (B Iron/B Air), (d) Average Factor Curve……74
Figure 5.10: (a) Normb Average Factor and Curve Fit, (b) Normb Error……... 76
Figure 5.11: (a) *Bz* Average Factor and Curve Fit, (b) *Bx* Average Factor and Curve Fit, (c) Error of *Bz*, (d) Error of *Bx*……76
Figure 5.12: a) 3-Coils in Triangular Setup, b) 4-Coils Horizontal Configuration, c) 4- Angled Coils Configuration, and d) 6-Coils Configuration……77
Figure 5.13: Variation of the Magnetic Field Lines When They Pass Through the Iron Particle…….. 78
Figure 5.14: The Increment of the Magnetic Flux Density *B* Within the Iron Particle…….. 79
Figure 5.15: Variation of *B* Values with Respect to the Position Along X Axis for the Two Electromagnets Aligned Along X Axis……... 80
Figure 5.16: Variation of *B* Values with Respect to the Position Along the Red Dashed Line for the Two Electromagnets Aligned on X and Y Axes…… 80
Figure 5.17: The Flexible Magnetic Abrasive Brush (Fmab)……81

Figure 5.18: Schematic of (MAF) with Details of Forces on A Single Abrasive Particle…… 81
Figure 5.19: Schematic of the Area A of (FMAB) According to the Cantor of Magnetic Field …….. 83
Figure 5.20: Aluminum Oxide Abrasive Particle…….. 86
Figure 5.21: Penetration of a Tetrahedral Magnetic Abrasive Particle: (a) Depth Of Penetration, (b) Projected Area Of Indentation, And (c) Projected Area of Penetration [64]…… 86
Figure 5.22: A Nanohardness Test Illustrates the Indentation Profiles of Different Radii [65]…….87
Figure 5.23: Example of the Variation of Penetration Depth With the Indentation Load [67]……... 88
Figure 5.24: Forces on a Single Abrasive Particle……..89
Figure 5.25: The Variation of Force Tangential Component on The Surface of the Workpiece…….... 90
Figure 5.26: Comparison Between Calculated and Simulation Values of Force Component……91
Figure 6.1: The Morphology of Al Sample Surface (a) and (c) Before, and (b) and (d) After…….95
Figure 6.2: Gaussian Membership Function For Input Parameters (a) Applied Voltage (b) Frequency (c) Time (d) Particle Size……101
Figure 6.3: Triangular Membership Function for Output Parameters (a) Average Surface Roughness (b) Percentage of Surface Roughness Reduction……101
Figure 6.4: Gaussian Parameters……102
Figure 6.5 : Demonstrated Example of MOM……... 105
Figure 6.6: Demonstrated Example of COA……..105
Figure 6.7: Predicted Average Surface Roughness by Fuzzy Logic with Respect to Parameters (a) Applied Voltage and Particle Size, (b) Applied Voltage and Time, (c) Applied Voltage and Frequency, (d) Particle Size and Frequency, (e) Time and Particle Size, (f) Time and Frequency……108
Figure 6.8: Predicted Reduction Percentage of Surface Roughness by Fuzzy Logic with Respect to Parameter Changing (a) Applied Voltage and Particle Size, (b) Applied Voltage and Time, (c) Applied Voltage and Frequency, (d) Particle Size and Frequency, (e) Time and Particle Size, (f) Time and Frequency……...109
Figure 7.1: Applying Smaf to Modify the Surface Roughness of Aluminum Foil……116
Figure 7.2: 3D Photographs of Finished Surface of Aluminum Foil (a) Before and (b) After Finishing Process…… 116
Figure 7.3: Applying Smaf to Modify the Surface Roughness of BLT Slab……..117
Figure 7.4: 3D Photographs of Finished Surface of BLT Slab (a) Before and (b) After……..…...118
Figure 7.5: Applying Smaf to Modify the Surface Roughness of an Aluminum Tube…….. 118
Figure 7.6: 3D Photographs of the Internal Finished Surface of Aluminum Tube (a) Before and (b) After Finishing Process…….. 119

Figure 7.7: Applying Smaf to Modify the Surface Roughness of an Aluminum U-Shaped Groove. 120
Figure 7.8: 3D Photographs of the Finished Surface of Aluminum U-Shaped Groove (a) Before and (b) After Finishing Process……. 120
Figure 7.9: Applying Smaf to Modify the Surface Roughness of Titanium Sample……...121
Figure 7.10: 3D Photographs of the Finished Surface of Titanium Sample (a) Before and (b) After Finishing Process……. 122
Figure 7.11: 3D Photographs of the Finished Surface of Inconel Sample (a) Before and (b) After….122

List of Tables

Table 3.1: Function of the L298 [45]……..27

Table 3.2: General Pattern for Four-Coils Configuration…….35

Table 4.1: Simulation Results ……50

Table 4.2: Simulation Results with Respect to Constant (*lw*) and (*P*) …….. 51

Table 4.3: Simulation Results with Respect to Variable (*lw*) and (*P*) ……... 52

Table 4.4: Comparison Between Measured and Simulation Values of Particle Force …… 61

Table 4.5: Experimental Conditions …..…….…... 62

Table 5.1: Fit Functions and Maximum Error……... 75

Table 6.1: Parameters and Levels Used in the Experiments...…….……..……...94

Table 6.2: Experimental Layout Using an L9 Orthogonal Array…….....…… 97

Table 6.3: Experimental Layout and Results Based on Taguchi L9 OA……..……...97

Table 6.4: Parameters and Levels Used for the Prediction Model…….....98

Table 6.5: Fuzzy Linguistic and Variables Characteristics of the Parameters …….....99

Table 6.6: Input Factors and Levels for the Prediction Model.……..……...…..99

Table 6.7: Output Factors and Levels for the Prediction Model ……..100

Table 6.8: Input and Output Factors and Levels for the Prediction Model According to L25 Taguchi OA ……..…103

Table 6.9: Rules for the Fuzzy Logic Prediction Model According to L25 Taguchi OA ……...104

Table 6.10: Accuracy and Error Percentage of the Fuzzy Logic Prediction Model According to L9 Taguchi OA ……..……110

Chapter 1

Introduction

1.1. Background

A high-quality surface with a low value of surface roughness and high dimensional accuracy is required for products in different applications such as aerospace equipment, medical instruments, semiconductors, automobiles, tools and dies, among others. The modern manufacturing industries are dependent on advanced materials like alloys of hard materials, glass, ceramics, and composite materials, to produce components with a complex shape for these applications. Final finishing of these materials is difficult due to high hardness and toughness, as well as the shape complexity of the products [1]. The final operation in manufacturing of components is the finishing process and it requires approximately 15% of the total manufacturing cost [2]. One promising precision surface finishing technique is abrasive finishing. It is widely used to finish the complex shapes of hard materials while providing precise tolerances that can be required in advanced engineering applications [3].

Magnetic fields have assisted in a wide spectrum of manufacturing processes such as finishing, cleaning, deburring, and burnishing of difficult to machine materials [4-6]. They have been used in a number of machining and abrasive finishing techniques to control the effective parameters of these processes, such as finishing force and applied voltage. Magnetic Abrasive Flow Machining (MAFM), Magnetic Float Polishing (MFP), Magnetorheological Abrasive Flow Finishing (MRAFF), and Magnetic Abrasive Finishing (MAF) are some examples of these abrasive machining processes [3-6]. Additionally, abrasive finishing utilizing magnetic fields have also been used to overcome the limitations of traditional finishing processes, in terms of accuracy, shape complexity, and cost. Traditional finishing processes cannot finish complex shaped workpieces, for example, cooling holes in turbine blades having diameters less than two millimeters [4-7]. The cutting energy in traditional finishing methods, which use rigid tools, is mainly used to overcome the cohesion forces of the machined material. Also, mechanical properties of the finished part can be affected by surface cracks and internal stresses due to external forces applied by the high-strength rigid tools. Furthermore, the finished material's properties can also be affected by microstructural changes due to excessive heat which is generated during performing of the finishing processes, especially when most of the cutting energy is transferred into heat and absorbed by the workpiece [4-7]. These limitations become substantial factors during micromachining processes which are used to fabricate micro-components or to create micro-features on macro/micro-parts [8].

1.2. Overview of Abrasive Finishing Processes (AFP)

Generally, a finishing process can be defined as a removing of a thin layer of a material with a Micro or Nano scale in the form of fine chips. This process may be required to improve the workpiece surface characteristics and quality, and also to refine the product tolerances in order to fulfill the manufacturing requirements [4-7]. AFP is usually used for products which have already been machined by other methods. Compared to rigid-tool-finishing processes, AFP utilizes abrasive particles in finishing or polishing the workpiece to improve the surface texture. Using abrasive particles as a multi-edged cutting tool lends to the finishing process' unique attributes, in comparison to rigid-tool-finishing-processes. These attributes can be summarized as follows [9]:

1. Modifying the surface texture and quality.
2. Reduction in surface damage and residual stresses.
3. Minimizing of the heat-affected zone extents.
4. Enhancing the geometrical tolerance.

There are many criteria which can be considered in classifying AFP into different categories. These criteria are; the fundamental principles of the process, state of the abrasive particles, the tools used, and finishing methods, as illustrated in Figure 1.1 [9].

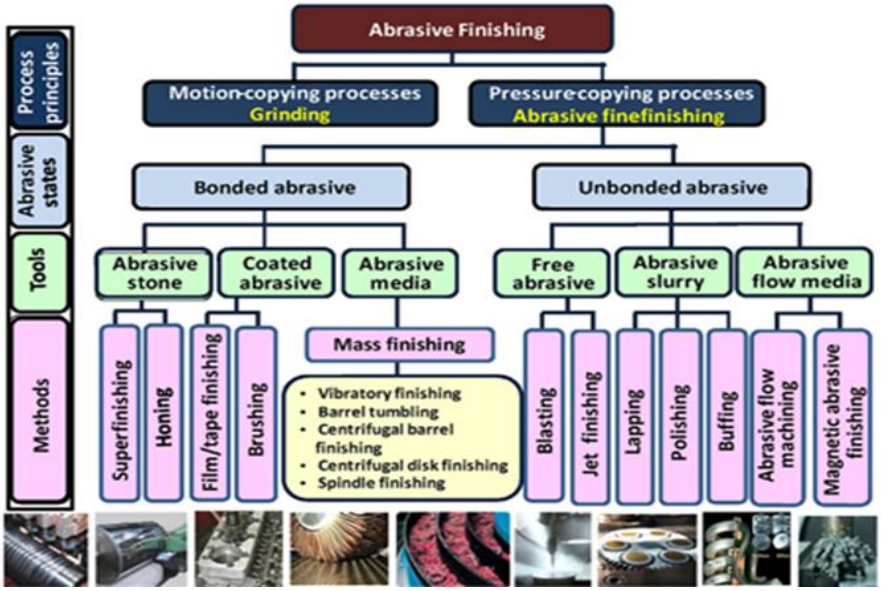

Figure 1. 1: Classifications of Abrasive Finishing Processes (AFP) [9].

1.2.1. Process Principles Classification

According to the fundamental principles of the process, AFP is classified into two main categories [10]:

a. Motion-copying-processes

In this category, material is removed to a specific depth of cut. This helps to control the dimensions of the finished part accurately. The grinding process can be considered as an example of this kind of process due to use of a grinding wheel as a bonded abrasive tool, as shown in Figure 1.2, representing a motion-copying-process. The grinding wheel rotates in a range of 20-140 m/s which is considered high speed relative to the other finishing processes [11].

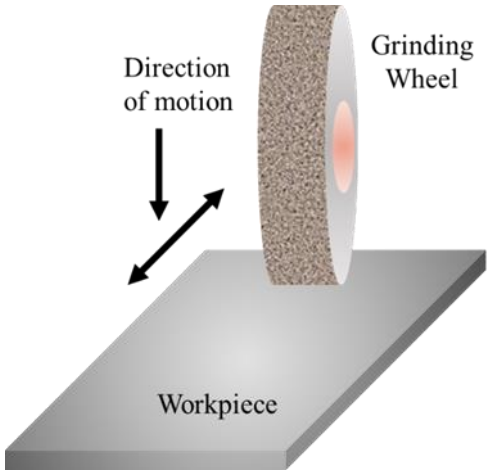

Figure 1. 2: Schematic of grinding process as an example of a motion-copying-process.

b. Pressure-copying-processes

The work principle of this category is based on using the pressure of a finishing tool against the finished surface to remove the material. This helps to obtain the desired surface geometries and to modify the surface integrity, however it cannot be used to control the dimensional accuracy. Many of the AFP such as honing, lapping, polishing, and superfinishing can be considered good representative examples of this category [9]. Figure 1.3 provides a schematic of the pressure-copying-processes examples.

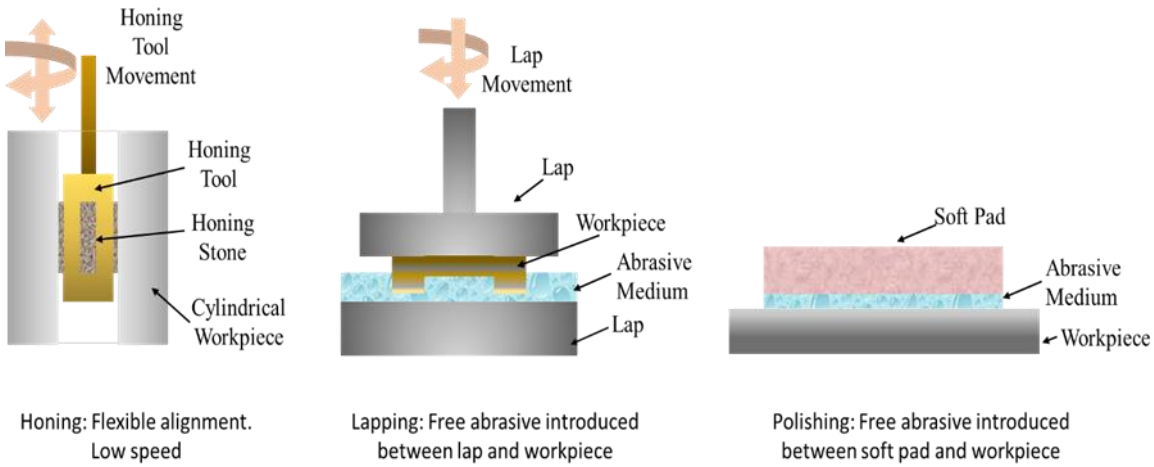

Figure 1. 3: Schematic of pressure-copying-processes examples.

Honing is an abrasive finishing process using abrasive particles to accomplish the finishing process. The abrasive particles (grains) in honing are fixed in a bonded small stone tool as with the grinding wheel. However, there are two features that distinguish honing from grinding. Honing is usually used to finish internal cylindrical surfaces, and its tool is flexibly aligned to the finished surface. The typical surface speed range is 0.2-2 m/s [11].

In the lapping technique, the abrasive particles are suspended in a liquid lubrication medium between lap (or laps) and the surface of the workpiece. Compered to honing, lapping is a gentler process due to the low surface removal rate per pass. It is also used for flat surfaces which require high tolerance [11].

Similar to lapping, polishing utilizes free (un-bonded) abrasive particles to perform a finishing process. The free abrasive particles are inserted under a comfortable pad to apply a gentle pressure on the workpiece surface and reduce the penetration depth of individual grains [11].

1.2.2. Abrasive Particle State Classification

According to the abrasive particle state, AFP can be classified into two categories; bonded and un-bonded [9]:

a. Bonded Abrasive

This contains a bonded abrasive in the form of abrasive stones, abrasive media, and coated abrasives. The main feature of items in this AFP category is that the abrasive particles perform the finishing process as a fixed matrix. Abrasive stone is usually used in honing and it includes granules, bonding elements, and pores, whereas abrasive media is composed of a core of polymer wrapped with the abrasive bond. The polymer core is available in different shapes such as spheres, cylinders, and triangles.

In coated abrasives, the abrasive particles are bonded to a flexible substrate such as paper or plastic tape using adhesives. They are usually used in honing and superfinishing.

b. Un-bonded Abrasive

Un-bonded abrasive means that the abrasive particles freely move on the workpiece surface to accomplish the finishing operation. Based on that, the abrasive tools can be divided into three groups. The first group is the free abrasives which are used in finishing processes such as blast finishing. The second group is abrasive slurries which are usually used in polishing and lapping processes. Lastly, the third group is abrasive flow media which are used in magnetic abrasive finishing and abrasive flow machining. In some AFP, the abrasive particles are mixed with ferromagnetic particles, just like magnetic abrasive finishing. Whereas, in other AFP, viscous liquid carriers are used to carry the abrasive particles, such as in abrasive flow machining [11].

1.3. Material removal mechanism in Abrasive Finishing Processes

To understand the material removal mechanism in AFP, interaction between the abrasive particles and the finished surface of the workpiece must be understood. This interaction is described on a microscopic level and the overall finishing process is defined by this level, including the cutting force and the rate of the metal removal per single abrasive particle. The main boundary conditions of AFP, as shown in Figure 1.4, include the finishing forces which contain the normal and tangential components (F_n and F_t) respectively. Also, it includes the kinematic boundary conditions which are described by identifying the abrasive particle path and its penetration depth (depth of cut) on the finished surface. Further included is the energy bound, as the abrasive particle comparatively slides on the workpiece surface with energy due to the finishing forces and sliding velocity [9].

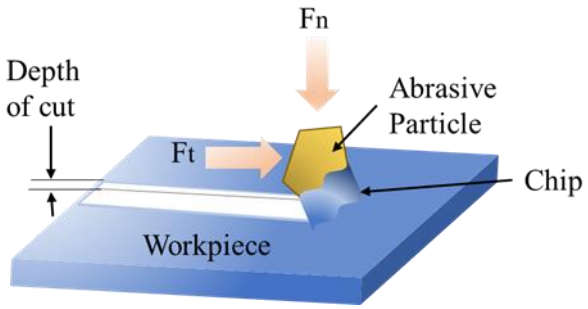

Figure 1. 4: Schematic of AFP finishing conditions.

The interference between the abrasive particle and the workpiece surface during the finishing process can mainly be divided into three phases; fatigue, cutting, and rolling. As illustrated in Figure 1.5, the angle α represents the impact angle of the momentum or velocity of the abrasive particle measured with respect to the normal direction of the workpiece surface. This angle dictates which phase is applicable during the machining process. When angle α is small, Figure 1.5 (c), the abrasive will be indented into the workpiece surface and will push the material around the dent, in the case of a ductile material. If the workpiece is brittle, cracks might initiate underneath the dent, then propagate under the effect of frequent bombardment of the abrasive particle. This will lead to removal of the material from the workpiece surface [9].

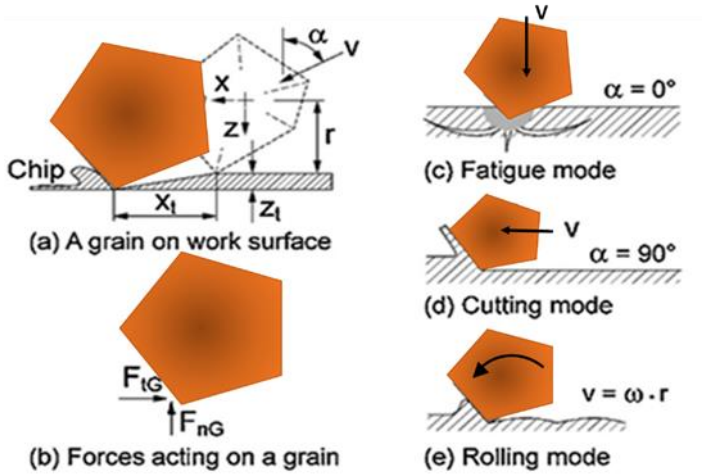

Figure 1. 5: Schematic illustrates the interaction phases of abrasive particle (a) Kinematics of abrasive, (b) Finishing force components on the abrasive, (c-e) Interaction phases between abrasive and workpiece surface (Reproduced from [9]).

At higher α, there are two expected scenarios for the abrasive particle kinematics behavior based on the kind of particle rotation. The first scenario is when the particle rotation is restricted, as shown in Figure 1.6. In this case, it can be noticed that most of the abrasive particle momentum in the tangential direction contributes in performing the finishing task by making scratches on the finished surface and removing the material in the form of tiny chips. The second scenario is when the particle rotation is free, as illustrated in Figure 1.5 (e). In this situation, the abrasive particles hit the surface and roll over making imprints on the finished surface. This leads to improving the surface profile [9].

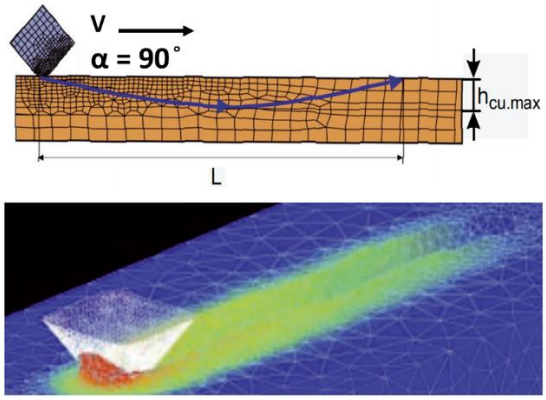

Figure 1. 6: Model of a single abrasive particle scratching (Reproduced from [12]).

1.4. Magnetic Abrasive Finishing

Magnetic Abrasive Finishing (MAF) is a micromachining process. It can be considered as a pressure-copying-process, and is an advanced and non-traditional finishing process developed to produce a high quality finished surface efficiently and economically [6]. In the MAF technique, a workpiece is placed within a magnetic field which is produced by a permanent magnet or an electromagnet. The working gap between the workpiece and the magnetic source is filled with the Magnetic Abrasive Particles (MAPs) as shown in Figure 1.7. Applying a relative motion between the magnetic source and the workpiece makes MAPs scratch the surface of the workpiece and remove a thin micro or nano layer in the form of fine chips [4-7].

MAF can be used, as shown in Figure 1.7, for the internal and external surfaces of complex shapes and tubes, which are difficult to finish using the conventional finishing processes. MAF can be used for magnetic or non-magnetic materials and can also be used for flat surfaces.

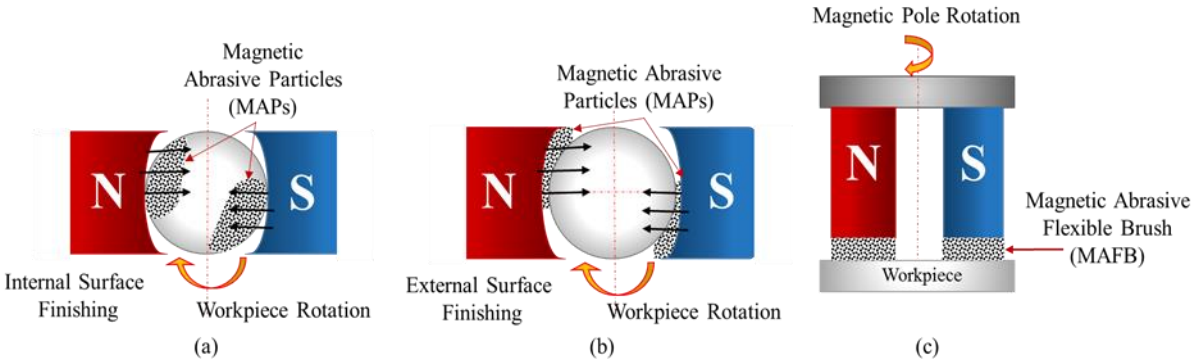

Figure 1. 7: Examples of existing MAF methods, (a): Fixed magnetic source with rotated work piece internal Surface Finishing. (b): Fixed magnetic source with rotated work piece external Surface Finishing. (c): Rotated magnetic source with fixed work piece.

In the MAF process, a magnetic force is used as a cutting (finishing) force in order to produce precision surfaces with high quality [13]. Finishing force in the MAF technique represents magnetic force which is produced by a magnetic field. The magnetic field can be controlled by regulating the exciting current of the electromagnetic coil which is mainly provided by a direct current (DC) power supply, so the magnetic force (finishing force) can be regulated and controlled. This regulation and controlling can be considered an important feature of the MAF technique for fine finishing without damaging surface topography [14]. Another main feature of the MAF technique is that no rigid tools are required to perform the finishing process. These features make the MAF technique different from the traditional methods of finishing processes, such as grinding, honing, and lapping, which normally use a rigid tool to perform the finishing process. Therefore, in traditional finishing processes, the finished surface will be subjected to substantial normal stresses. These stresses may cause micro-cracks and other defects which reduce the strength of the finished parts. Thus, in the MAF technique the formation of microcracks on the finished surface of the workpiece, which are mainly caused by the normal stresses, are minimized [5].

In MAF processes, an abrasive material called Ferromagnetic Abrasive Particles or Magnetic Abrasive Particles (MAPs) [7] is used. These particles are generally used with fine and hard granular abrasive particles such as Al_2O_3, SiC, CBN, or diamond, as shown in Figure 1.8.

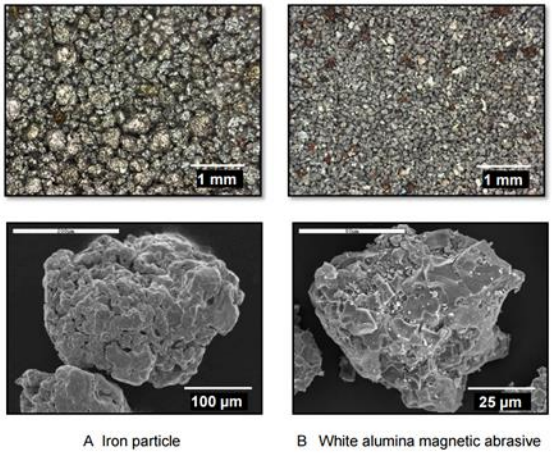

Figure 1. 8: Microscopy and scanning electron microscopy of A) iron particle (dia. 150~300 µm), and B) white alumina (WA) magnetic abrasive (mean dia. 80 µm, aluminum oxide (Al2O3): ≤10 µm) [7].

To successfully perform the finishing operation for the workpiece surface, the motion of Magnetic Abrasive Particles (MAPs) should be controlled. This represents a critical task since MAPs are suspended in the magnetic field which is generated by an electromagnet [15]. Manipulating the magnetic field in the working area drags MAPs to the targeted finishing area and performs the surface finishing operation. The magnetic field is generally controlled by the geometry and arrangement of the electromagnets, as well as the geometry of pole tips attached to the electromagnets [7].

This research develops a new finishing method featuring the use of a rotating magnetic field to improve the finishing efficiency of the produced part. Further, it explains the processing principles of the newly developed finishing method and describe the surface finishing characteristics. The metal removal and finishing mechanism also is investigated and described.

1.5. Surface Roughness terminology

One of the main objectives of this thesis is improving the finished surface roughness and characteristics. Thus, it is important to define the fundamental terminology of the surface roughness. There are many terms related to surface roughness and surface finishing often used to describe and quantify the finished surface characteristics and smoothness. The concepts of these terms can be identified according to the American Standard B46.1 of Surface Texture as follows [16]:

- Surface texture

Surface texture represents the surface pattern observed on a primary surface. This pattern might be repetitive or random due to the roughness, waviness, lay, or flaws.

- Real Surface

The term real surface refers to the superficial layer which surrounds the body and isolates it from its ambient medium. This layer represents, without any distortion, the structural deviations which are mainly consisting of surface roughness, waviness, and the surface details.

- Roughness

Roughness represents the surface texture contrasts which are formed as a result of the manufacturing and machining processes. Figure 1.9 illustrates profiles of roughness (width and height). Roughness width denotes the distance between the contiguous peaks which represent the pattern of the surface roughness. Whereas, Roughness height refers to the vertical distance of the peak-to-valley for the local surface profile.

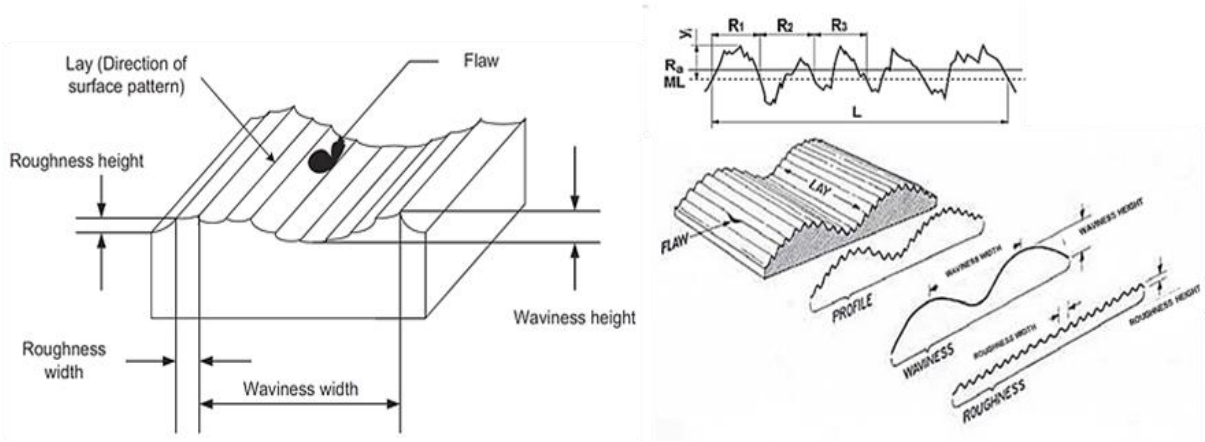

Figure 1. 9: Schematic of surface profile and roughness (Reproduced from [17]).

- Roughness sampling length (L)

This is the length of the surface sample for which average roughness is intended to be determined. This length is specified in order to characterize the surface contrasts and whether they are to be classified as roughness or waviness.

- Waviness

This represents the wider spaced element of the surface texture profile. It can be formed from machining conditions or vibration chatter. The waviness width is the width of this element of the surface texture, while waviness height is the peak-to-valley distance of the global surface profile.

- Average Roughness (R_a)

This refers to the arithmetic mean roughness value of the deviation of the roughness profile from the mean surface line (*ML*). It is also defined as the arithmetic average or center line average. R_a can be computed as [17]:

$$R_a = \frac{1}{L}\int_0^L |y(x)|dx \tag{1.1}$$

where *Ra* refers to the arithmetic average deviation, *L* is the length of the surface sample, and *y* is the ordinate of the surface profile curve.

- Root-mean-square (rms) roughness (R_q)

This is the standard deviation of the height distribution (roughness structure). R_q can be calculated from the formula:

$$R_q = \sqrt{\frac{1}{L}\int_0^L y^2(x)dx} \tag{1.2}$$

- Maximum peak-to-valley height (R_{max})

This is the distance between two lines which include the highest and lowest points on the surface profile. These two lines must be parallel to the *ML*.

- Lay

This is the direction of the prevailing surface profile which is formed due to the machining process.

- Flaws

These are unwanted distortions in the surface topography.

1.6. The proposed system overview

The proposed setup is a stationary system that depends on using a rotating magnetic field to move MAPs on the workpiece surface and control the finishing process. In addition to a flat surface, this setup is examined to ensure it is applicable to finish a component with a complex shape such as: femoral components of knee prosthetics, grooves of ring seals, and surface and initial edges of cutting tools.

This system does not require any mechanical moving parts to perform the finishing process. It depends on use of a rotating magnetic field which can be obtained by energizing the electromagnets sequentially via controlling their duty cycle and on-time interval. In most of the previous work in the literature, the

electromagnets are activated by using a direct current (DC) power supply. However, using DC power supply causes two essential problems: coil heating, which may damage the electromagnet, and exhaustion of the abrasive particles' cutting edges due to continuous use of the same particles [18]. Thus, using the proposed technique for energizing the electromagnets can solve these problems and overcome the drawbacks.
Furthermore, the main features of the proposed system includes:

1. **A wide range of surface roughness:** By using a different mesh size of MAPs, with regulating the magnetic field and magnetic force (cutting force), it is possible to produce finished surfaces with a wide range of surface roughness for different applications.
2. **Cutting force control:** CFC is obtained by controlling the depth of penetration of the abrasive particle in the workpiece surface. This depth represents the thickness of the metal removal layer and it depends on the normal component of the cutting force (magnetic force), as explained in Chapter three.
3. **Cost saving:** In terms of cost and economic factors, the proposed system can be considered a cost saving system as it does not require a motor or any mechanical moving parts. Thus, the system setup cost and maintenance cost can be reduced.
4. **Size and mobility:** The developed system is smaller in size compared with previous (similar) finishing systems. Furthermore, it can be considered a portable system, since there is no need for a motor or machining equipment to connect to it. So the developed system is lightweight, portable and whisper-quiet.

1.7. Thesis Objectives and Outlines

This study aims to propose a novel magnetic abrasive finishing design using stationary equipment whereby the machining process is carried out by regulation of magnetic fields without using any mechanical moving parts. A rotating magnetic field, which is obtained by energizing the electromagnets sequentially via control of the duty cycle, and on-time interval, for each electromagnet, was used. Thus, regulating the magnetic field allows control of the magnetic force which, in this case, represents the cutting force. This enables automating of the performance of the finishing process. Further, it enhances the accuracy and controllability of the process, and it also improves the quality of the final product. From another perspective, it also minimizes the mechanical power consumption by elimination of any mechanical motion.

The designing process involved several steps including development of a simulation and mathematical model for the metal removal mechanism and magnetic and cutting force calculation of the MAF process. In addition to design and optimization of the electromagnetic actuator and fabrication of the experimental setup. Moreover, studying the effect of the process parameters (such as applied current, frequency of the rotating of the magnetic field, and magnetic abrasive particles), and characterizing of the finished surface with respect to the roughness profile and surface textures is done.

This thesis is organized as follows:

Chapter 1 presents a brief overview of the abrasive finishing processes and their classifications of applications. The MAF process is defined briefly with an overview of the proposed system and its features. Also, the fundamental terminology of the surface roughness is clarified. The thesis objectives and scope are also presented.

Chapter 2 presents various techniques of MAF, and different types of finishing mechanisms. It points out the necessity of the research described in this thesis due to showing that most of the previous work has involved a relative (non-stationary) motion between the magnetic source (electromagnet or permanent magnet) and the workpiece.

Chapter 3 provides the details of the Stationary Apparatus Magnetic Abrasive Finishing (SMAF) technique and the communication between its different components. It explains the possibility of using stationary electromagnets and a workpiece by manipulating the excitation current to produce a rotating magnetic field. Various physical configurations of the electromagnet coils are presented.

Chapter 4 discusses the design and optimization approach used to optimize the geometry of the electromagnet. This approach is carried out in two stages. In the first stage, the integrated formula of a thin shell solenoid is used to obtain the gradient of the magnetic field at any point on the axis of a finite solenoid. In the second stage, a parametric study is carried out using a finite element simulation. Moreover, a new approach is conducted to measure the magnetic force experimentally using an ATI force sensor. The results are verified using a finite element simulation. Also the variation of temperature in the interfering zone between the workpiece and the magnetic abrasive particles is measured using a thermal camera.

Chapter 5 explains the fundamental models used to represent the relationship between the main parameters of SMAF. The Finite Element Method started with classical Maxwell's equations, as the governing equations, used to find the solutions of parameter to analyze the variation of the magnetic field

(B) in the working gap with respect to the magnetization effect of the particles and the electromagnets' angle of alignment. Further, the magnetic force (cutting force) is also analyzed with its components, the normal F_{mz}, and tangential F_{mt} to determine their sufficient magnitude to remove the material from the workpiece surface.

Chapter 6 presents a fuzzy logic model for predicting the output parameters of the SMAF process based on experimental results. A fuzzy logic model using 25 fuzzy rules is developed to predict the average surface roughness and the reduction percentage of the surface roughness for a given input set of applied voltage, electromagnet energizing frequency, operating time, and size of abrasive particles. The Taguchi orthogonal array technique is chosen to design the experiments and build the fuzzy logic predicted model.

Chapter 7 examines the performance of the SMAF technique. This technique is applied to perform the finishing process for different materials, and different shapes and geometries. SMAF is first applied to finish the surface of a thin film sheet of aluminum foil, followed by a composite material sample of BLT slab, an internal surface of 10 mm diameter aluminum tube, and a U-shaped 2 mm × 2 mm tiny channel of an aluminum slab. Additionally, the proposed technique is applied to perform a surface finishing process for "hard-to-machine" materials, Titanium and Inconel.

Chapter 8 presents the conclusions of this thesis and recommendations for future work. So far, this research has resulted in the publication of 2 journal articles and 1 conference paper. Also 1 journal article is now under review. A list of publications related to this research is provided in Appendix A.

1.8. Thesis Contributions

The design and development of the stationary magnetic abrasive finishing apparatus includes contributions in the following areas:

- Developing a novel design of a stationary magnetic abrasive finishing system that utilizes a rotating magnetic field to move MAPs on the workpiece surface and control the finishing process. As opposed to the conventional finishing processes, this system does not require any mechanical moving parts to perform the finishing process. It depends on using a rotating magnetic field which can be obtained by energizing electromagnets sequentially while controlling their duty cycle and on-time interval.
- Developing a model to calculate the cutting force per single abrasive particle, and a novel approach to measure this force experimentally.

- Design and optimization of an electromagnetic actuator used as a magnetic field source (to produce a rotary magnetic field).
- Developing a fuzzy logic prediction model to predict the average surface roughness of the finished surface.
- Applying the developed technique successfully in different surface finishing applications, for flat surfaces such as thin film materials, and a sample of BLT ceramic slab, and also for difficult-to-reach areas, such as internal surfaces of a thin tube, and tiny channels. Additionally, it is applied to hard-to-machine materials including Titanium and Inconel.

Chapter 2

Literature Review

2.1. Introduction

Henry P. Coats was the first to mention Magnetic Abrasive Finishing (MAF) in his patent in 1938 in the USA. Later MAF was further developed by researchers in the former USSR and Japan [19]. Many studies have been conducted to investigate the MAF process parameters and performance. Some of the studies employed permanent magnets as a magnetic field source, while others used electromagnets with direct current (DC) or alternating current (AC).

2.2. Permanent Magnet Based MAF Process

The first attempt to explain the basic principles of the Magnetic Abrasive Finishing (MAF) process was done by Shinmura T. et al. [19-20] where they confirmed experimentally in a model test that the Magnetic Abrasive Particles (MAPs) supply enough pressure to finish the work surface corresponding to the strength of the applied magnetic field. They described the internal finishing process of a stainless steel tube by MAF. They also studied the effect of process parameters that could affect the final surface roughness. They found that the strength controlling of magnetic force is dependent on the material, shape and size of the workpiece, and the shape and size of the permanent magnet. The experimental results showed that the surface roughness was improved up to 0.1μm Rmax. Yamaguchi H. et al. [21-23] proposed an internal MAF process using a rotating magnetic pole with a new technique of magnetic field assisted finishing. The relationship between the magnetic field, force on the abrasive, and the abrasive behavior were explained in this study in addition to the effect of the abrasive behavior regarding surface modifications. They found that the quality of the finished surface depends on the volume of lubricant which affects the abrasive contact with the workpiece surface and changes the finishing force acting on the abrasive, which controls the depth of cut.

A mechanism of a planar magnetic abrasive polishing process for a nonmagnetic material, stainless steel was done by Mori T. et al. [24]. They examined the formation of a Magnetic Abrasive Flexible Brush (MAFB), and how the normal force pushes the abrasives on the brush end to indent into the material surface of the workpiece. The results of this study illustrated that MAPs penetrate the surface of the workpiece with a depth of penetration which is proportional with the magnetic force. Therefore, MAF is a penetration process not just a frictional process.

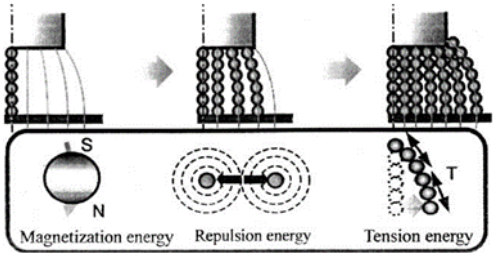

Figure 2. 1: Configuration of Magnetic Abrasive Flexible Brushes (MAFB) [24].

The MAF process was proposed by Wang and Hu [25] to produce high quality finished inner surfaces of tubes. They showed that there is an optimal magnetic abrasive particle size, 30–50%, for the abrasive/ferromagnetic volume ratio. This study concluded that the Material Removal Rate (MRR) increased with the increasing of the rotational speed of the magnetic pole. MAF was also used for the internal finishing of capillary tubes by Yamaguchi H. et al. [26-27]. They studied the factors affecting the conditions of a uniform internal finishing process, particularly the magnetic field and MAPs. This study concluded that the pole arrangement can be adjusted to control the magnetic field, in addition to controlling the MRR which leads to uniformity in the finished surface. Furthermore, they illustrated that the finishing characteristics are influenced by the supplied amount of MAPs and the magnetic force acting on it. In another study, Lin C.T. et al. [28] used a permanent magnetic finishing mechanism installed in a CNC machining center, as shown in Figure 2.2, to conduct free-form surface abrasion of stainless steel. The operations were performed using the Taguchi experimental design to study the effecting factors inclusive of the working gap, feed rate, and MAPs. The study showed that the working gap has the largest impact on the finishing quality.

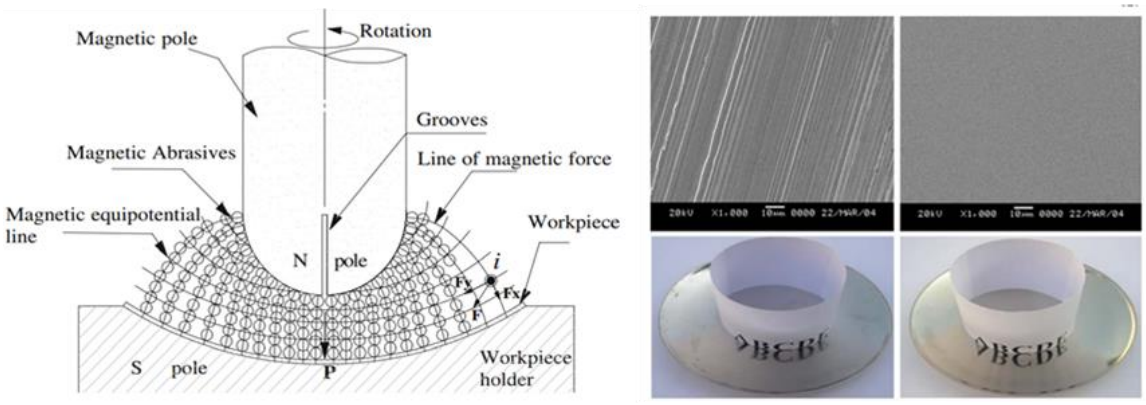

Figure 2. 2: Flexible magnetic brush and dispersion of magnetic force [28].

Yamaguchi and Hanada [29] proposed a method to make a spherical magnetic abrasive by means of plasma spray to improve the finishing performance, especially for the internal finishing of capillary tubes. This study illustrated that the thermal conditions of the plasma gas have strong influence on the shapes of the magnetic abrasive but negligible effects on the material structure. To prove that MAF can be used for non-ferrous materials, Kwak J.S. [30] proposed a method to improve the magnetic flux density in magnetic abrasive polishing process for a magnesium specimen. The magnetic flux density for ferrous and non-ferrous materials was simulated. He suggested to increase the magnetic flux density, a practical method that installed a permanent magnet at the opposite side of the work piece to be machined.

Junmo Kang et al. [31] proposed a multiple pole-tip system with a partially heat-treated magnetic tool to achieve the finishing of multiple regions simultaneously in capillary tubes.

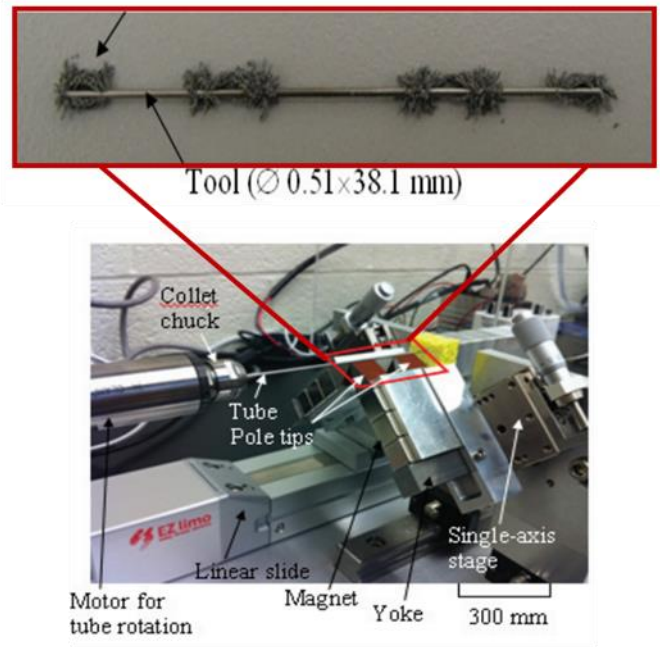

Figure 2. 3: Schematic of processing principle and photograph of experimental setup with double pole-tip sets [31].

2.3. Electromagnets Based MAF Process

The application of the electromagnets in Magnetic Abrasive Finishing (MAF) processes can also be classified into two categories: electromagnet with Direct Current (DC), and electromagnet with Alternating Current (AC).

2.3.1. Electromagnet with Direct Current (DC) MAF Process: Many studies have been conducted to characterize the material removal process and provide a fundamental understanding of the MAF process mechanism. Early research of using the electromagnet with DC in the MAF process was proposed by Kurobe, T. [32]. He developed a polishing setup to perform magnetic field assisted fine finishing. The setup consists of magnetic fluid filled into the grooves in a brass disk covered by a rubber plate having thickness 1 mm. The polishing abrasives were mixed with water and placed in a disk with two electromagnets set above and below it. When DC voltage was supplied, a magnetic field was produced and induced polishing pressure to perform the finishing operation. Yamaguchi H. and Shinmura T. [33] proposed internal use of an MAF process for producing highly finished inner surfaces of tubes used in critical applications including clean gas or liquid piping systems. This study examines, by using scanning electron microscopy, the microscopic changes in the surface texture resulting from the MAF process and the atomic force. Another investigation was done by Jain V. K. et al. [34] to study the effect of working gap and circumferential speed on the performance of in the MAF process. A series of experiments were conducted and showed that working gap and circumferential speed of workpiece were the parameters which significantly influence the material removal, change in surface roughness value (ΔRa), and percentage improvement in surface finish. Chang G.W. et al. [35] described in their study the principles and characteristics of the MAF process with the unbounded mixture of SiC abrasive and ferromagnetic particles with a SAE30 lubricant. Also, they described the mechanisms and finishing characteristics on surface roughness and material removal. Singh D.K. et al. [36] studied the effect of the process parameters which influence the surface roughness quality. They used the Taguchi design of experiments technique to find the important parameters. They found that voltage is the most significant parameter, followed by working gap. At the same time, the effects of grain mesh number, and rotational speed seemed to be very small. A new technique based on using a vertical vibration-assisted magnetic abrasive finishing process was used by Yin S. and Shinmura T. [37]. They applied this technique for the plane and edge surface finishing and deburring of a magnesium alloy. In this technique, a vibrating table was installed on the feeding table and the workpiece was vibrated in the vertical direction by the use of motorized cam systems. A relative motion was obtained consisting of vertical vibration and rotation between the magnetic brush and workpiece. The

finishing experiment results demonstrated that realization of the efficient finishing quality of magnesium alloys is possible by using the MAF process.

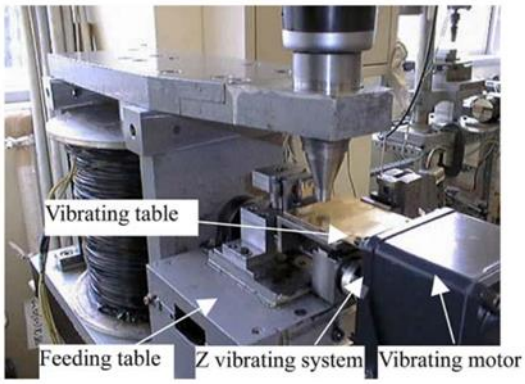

Figure 2. 4: Vibration-assisted magnetic abrasive finishing setup [37].

For complex internal geometries Jha S. and Jain V.K. [38] applied a new precision finishing technique using a magnetorheological polishing fluid (MR) containing carbonyl iron powder and silicon carbide abrasives with mineral oil. Due to the magnetic field, MR fluid exhibited change in rheological behavior which may be used to control the finishing forces, and accordingly, the final surface finish. Singh D.K. et al. [39-40] analyzed microscopic changes in the surface texture resulting from the MAF process to characterize the behavior of abrasive particles during the finishing process. Furthermore, surface roughness measurement, atomic force, and scanning electron microscopy have been used to obtain a better understanding of the finished surface pattern. Also, they tried to provide correlation between the surface finish and the acting forces. They used a resistance type force transducer (ring dynamometer) to measure the normal and tangential magnetic force components with the assistance of Lab-View software. They concluded that both forces and change in surface roughness (ΔRa) increase with the increasing in current and decreasing in the working gap. The surface roughness and material removal in the MAF process have been analyzed by Girma B. et al. [41], by using a response surface method on plane surfaces. This method was used to analyze the influence of various factors on MAF of plane surfaces, and also to obtain optimum parameter levels that give better surface finish and higher material removal. The researchers observed that the surface roughness was significantly influenced by the MAPs grain size, size-ratio, feed rate, and current.

2.3.2. Electromagnet with Alternating Current (AC) MAF Process: The first attempt of using the electromagnet with Alternating Current (AC) in the MAF process was proposed by Shinmura T. et al. [42]. They applied a rotating magnetic field which was obtained by activating three coils arranged in a circular alignment at intervals of 120̊ with a three-phase AC current. Experiments were conducted for an internal finishing of cylindrical work pieces. It was concluded that as compared with application of a static magnetic field, stock removal was increased by using a rotating magnetic field, but surface finish was reduced. Shinmura T. et al. [43] also proposed a new finishing process by applying a rotating magnetic field with six coils installed on a circular yoke. The coils were energized with a three-phase AC current. Experiments were conducted to finish the internal surface of a stainless steel tube from 4 µm of surface roughness to 0.4 µm. A new ultra-precision magnetic abrasive finishing process using an alternating magnetic field was described by Yanhua Zou et al. [6], as shown in Figures 2.5. They investigated the effect of finishing parameters such as rotational speed of magnetic pole, and alternating current frequency, on the metal removal rate and final surface finishing. Furthermore, they studied the effect of cutting fluid and proved that neat cutting oil is more suitable for this processing than water-soluble cutting fluid and silicone fluid.

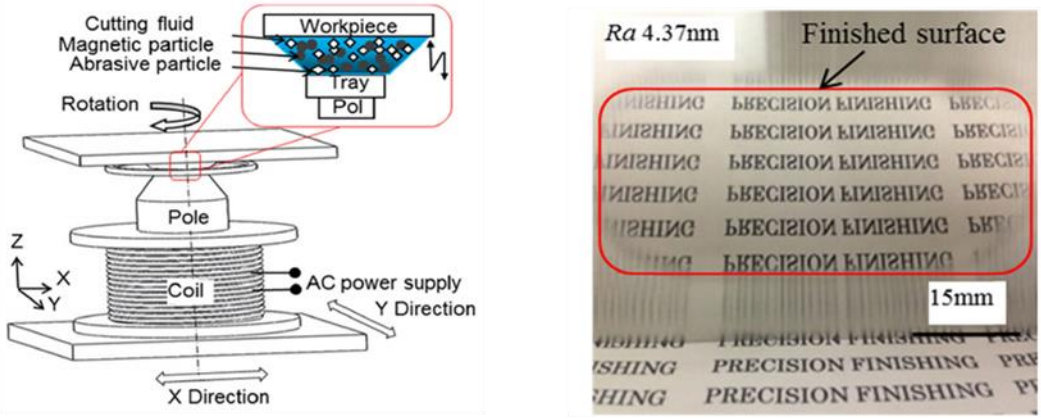

Figure 2. 5: Schematic of processing principle and photographs of finishing surface [6].

2.4. Conclusion and Motivation

This chapter presents various techniques of Magnetic Abrasive Finishing (MAF), and different types of finishing mechanisms. In conclusion, most of the previous work in the field of MAF, whether it

was an experimental work or modeling and simulation work, has involved a relative motion between the magnetic source (electromagnet or permanent magnet) and the workpiece. This motion can be obtained generally by using a motor or machining equipment like a lathe machine and milling machine. Some applications used a stationary magnetic source with a rotating workpiece as in [34-35], while others used a rotating magnetic source with a stationary workpiece, as in [23-24]. Thus, in all applications, a mechanical motion which is produced by a motor or machining equipment was required even when the electromagnet with alternating current was used. The requirement of the mechanical motion might be considered as a limitation for this method. This required motion affects the flexibility of mobility of the MAF system setup. Moreover, it affects the setup cost and machining operation cost due to its power consumption. Also, it requires a maintenance cost to improve the equipment effectiveness and achieve the desired surface roughness. On the other hand, using an electromagnet with direct current can cause essential problems regarding coil heating, which may damage the electromagnet, and exhaustion of the abrasive particles' cutting edges due to continuous use of the same particles. All these considerations represent motivation factors to investigate MAF setup modification through inclusion of a stationary system. The proposed setup implements a rotating magnetic field with stationary equipment whereby the finishing process is to be carried out by the regulation of a magnetic field without using a motor or any mechanical moving parts. The conducted system uses a proposed technique for energizing the electromagnets sequentially, with control of the duty cycle and on-time interval for each electromagnet in order to overcome the drawbacks mentioned. Also, the proposed system has smaller size compared with the previous (similar) finishing systems. Furthermore, it can also be considered to be a portable system, since there is no need for a motor or machining equipment to connect to it.

Chapter 3

Experimental Setup

3.1. Introduction

This study describes research on manipulating and controlling the magnetic field such that the magnetic particles will travel between the electromagnets, while the electromagnets and workpiece remain stationary. Several experimental setups for the mechanics of MAF have been analyzed. The objective of the research is to prove the concept that, by fixing both the coils and the work piece, the magnetic particles will move around from electromagnet to electromagnet or at least move around such that they can also perform magnetic abrasive finishing.

3.2. Controlling and MATLAB-Simulink

3.2.1. Control and Communication Setup

To perform experiments and test the concept, a control module which controls the electromagnets is essential; otherwise there would only be thought experiments and no concrete proof and data. Figure 3.1 is a simple flow chart of the communication from the MATLAB file to the physical system. In this application, the electromagnets are controlled through the use of a dSPACE machine, shown in Figure 3.2, and programs written in Simulink.

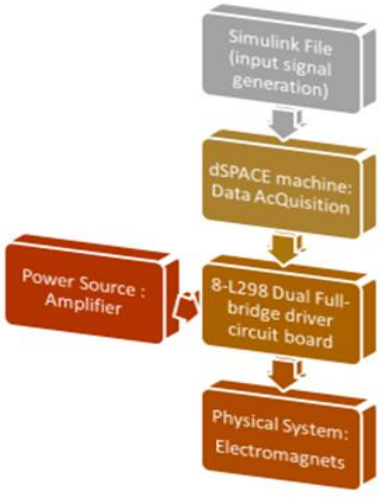

Figure 3. 1: Flow chart of the control and communication setup.

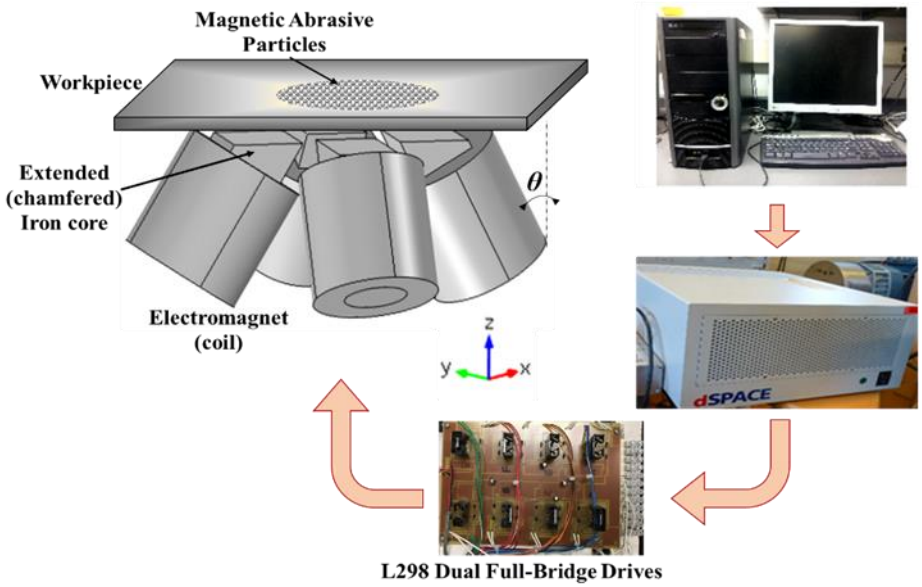

Figure 3. 2: System components.

Here, the dSPACE serves as a data acquisition device and the data source comes from the Simulink file. This section covers the communication and control setup, the necessity of using the L298 Dual Full-Bridge Driver, and the approach used to create pulse width modulation (PWM) in Simulink. It finishes with a discussion of the test of the Full-Bridge Driver and PWM Simulink file. Simulink, software that is part of MATLAB, is used primarily to simulate a system based on a mathematical model that the user builds depending on the application. It is a very powerful tool for engineering design applications. Before getting into the details of the Simulink file, this section explains the issue faced when the dual Full-Bridge Driver is not used during experiments. This is followed by how the L298 Full-Bridge Driver resolve the problem.

A coil becomes an electromagnet when a current is passed through its wire; a magnetic field is created and as a result magnetic attraction or repulsion occurs. Similar to a permanent magnet, an electromagnet has 2 poles, one pole on each side, North (N) and South (S). The electromagnetic coil used has an iron core. The problem becomes apparent when the magnetic particles start to stick to the core of the coil, as shown in Figure 3.3, even if no current is passing through the coil.

Figure 3. 3: Residual magnetism shown with particles sticking to the coil core.

This problem occurs because, during the operation, the particles that are going to scratch the surface of the workpiece are stuck on the coils. This makes the process less efficient and also wastes these particles. Secondly, the group of particles that stick onto the coil stay on it. As time passes, most of the mobile particles are accumulated on the coil and become immobile. This renders the operation useless. This phenomenon is due to the residual magnetism that is in the core of the electromagnetic coil which is made of iron, a ferromagnetic material, and the magnetic particles. This happens to ferromagnetic materials when they are always charged in a single direction of current leading to having a single pole facing the particles. Without the Dual Full-Bridge Drive, the current would go into the coil in a single direction while only one pole would always face the magnetic particles. Based on the Hysteresis Loop in Figure 3.4, the experiment runs in the first or third quadrant only.

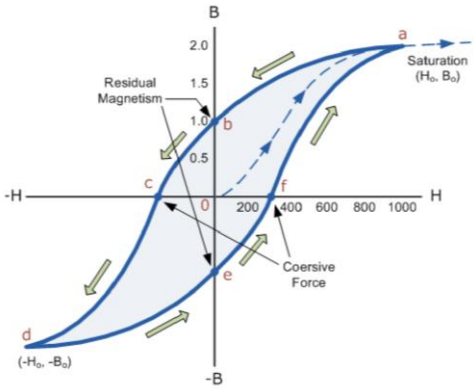

Figure 3. 4: B-H curve of Hysteresis Loop for a ferromagnetic material [44].

When no current goes through it, the state of the coil is located at point “b” or point “e” of Figure 3.4. In order to fully remove the residual magnetism, the current has to pass through the coil in the opposite direction as well, and so going through the Hysteresis Loop and not only one portion of it.

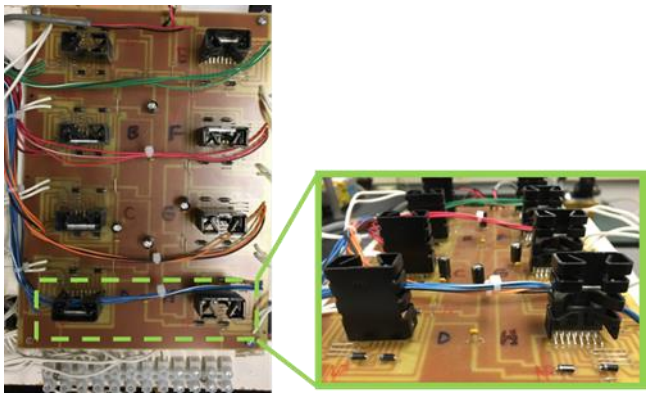

Figure 3. 5: L298 – Multiwatt 15 Dual Full-Bridge Driver.

How does the L298 – Multi-watt 15 Dual Full-Bridge Drive solve the problem with the residual magnetism? The key components on the circuit board, shown in Figure 3.5, include eight L298 – Multi-watt 15 Dual Full-Bridge Driver. This chip is capable of controlling the direction of the rotation of the motor. Figure 3.6, illustrates the pre-programmed functions block for the chip L298. The function corresponds to a motor, but the L298 basically controls the direction of the current, which then controls the direction of the rotation of the motor, either forward or reverse. This feature solves the residual magnetism problem, but it is important to be able to manipulate the direction of the current. This can then control the polarity of the coils: either North (N) or South (S) Pole. Recalling the B-H curve in Figure 3.4, with this chip point “c” and point “f” can be reached. The coils then no longer stay within a single quadrant, first or third. They can have states in all four quadrants.

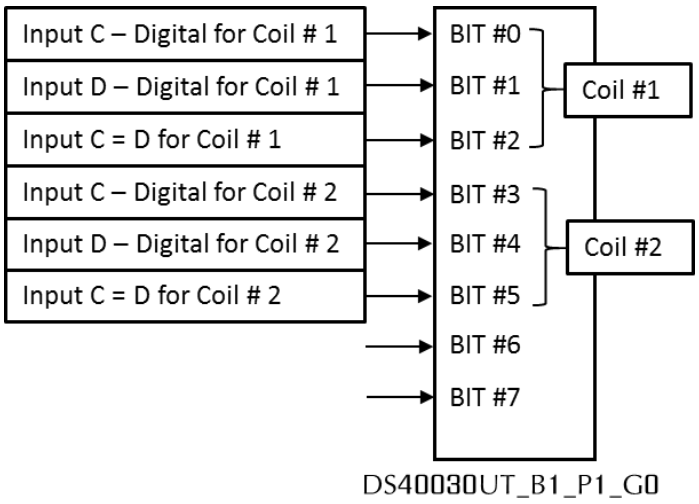

Figure 3. 6: Pre-programmed functions block for the chip L298.

Table 3.1: Function of the L298 [45].

Inputs (V, C & D)		Function
V = H	C = H; D = L	Forward
	C = L; D = H	Reverse
	C = D	Fast Motor Stop
V = L	C = X; D = X	Free Running Motor Stop
L = Low [0]	H = High [1]	X = Don't care

As shown in Table 3.1, the inputs are C and D. The values of High (H) and Low (L) are one (1) and zero (0) respectively. The chip works with the digital signal. This creates another issue in the input/output communication between the Simulink + dSPACE and the L298 Dual Full-Bridge Driver. From the Simulink file, if the input signal is analog, for example a sinusoidal wave, the chip is unable to perform its function. A method used to convert an analog signal into a digital signal is Pulse Width Modulation (PWM), discussed next.

3.2.2. Simulink - Pulse Width Modulation (PWM)

In simple terms, PWM converts an analog signal into a digital signal of 0 and 1. The overall time period of when the signal becomes 1 is called a duty cycle. If half of the time, the PWM signal is “on”, or 1, its duty cycle would be 50 percent. Therefore, as an example, with 5 volts of power supply, the device with 50 percent duty cycle would get 2.5 volts (half of the power supply). It would be the duty cycle times the voltage or power supply. This method is programmed in Simulink and analyzed here.

A PWM signal is obtained through comparison between an analog signal and a saw tooth wave signal. The logic is as follows: at time t, compare the analog signal to the sawtooth signal. Consequently, if the analog signal is larger than the signal of the sawtooth at time t, then the output gives 1 and vice versa. An example of a sinusoidal wave is shown in Figure 3.7. The green signal represents the sine wave (analog signal) and the blue signal in the same graph is the sawtooth signal. On the lower graph, in the same figure, the result of the comparison is shown in the magenta color signal of value zero or one.

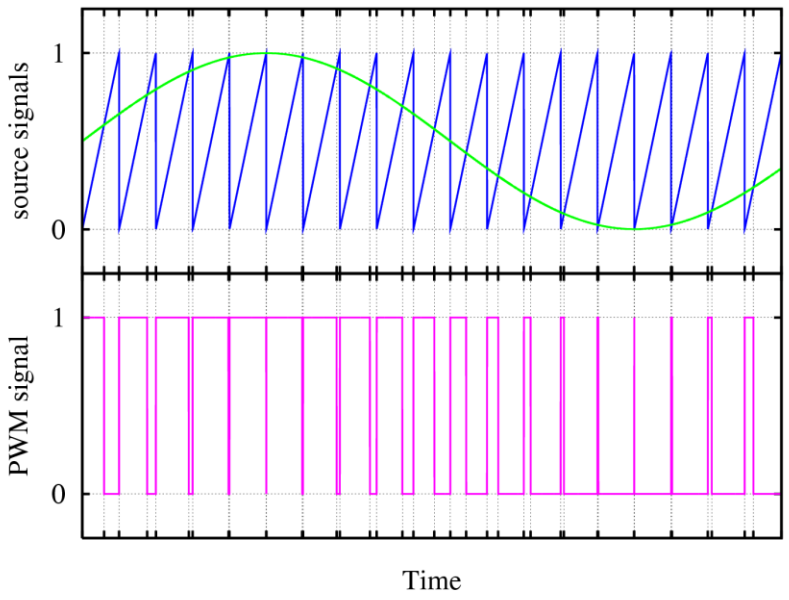

Figure 3. 7: Pulse Width Modulation [46].

Figure 3.8 is a screen shot taken from the Simulink file program based on the logic explained above.

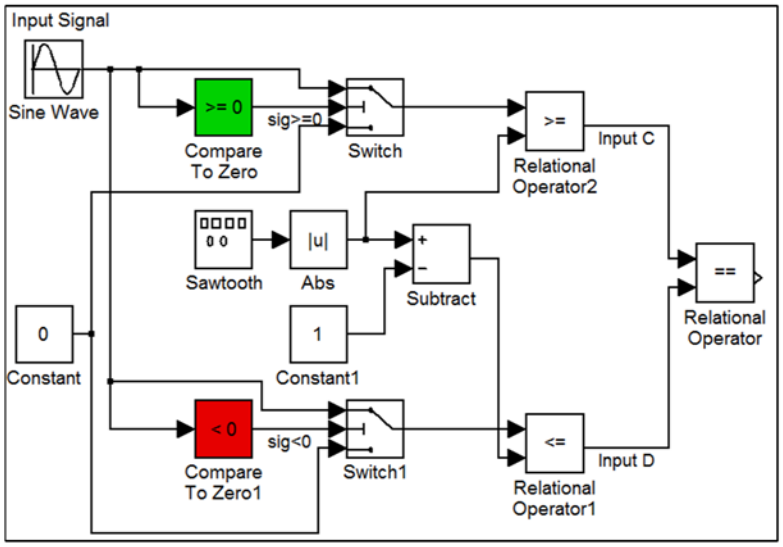

Figure 3. 8: Simulink Block Diagram for PWM.

First, the positive and the negative analog values are separated through the comparison with zero ("Compare To Zero") which will later be compared with positive sawtooth and negative sawtooth signals, respectively. A positive value will later become the input C (forward) and the negative value becomes input D (reverse). In Figure 3.9, this comparison block outputs the logic of the comparison. If the analog signal is equal or larger than zero, it will output the logic of 1, otherwise the output is 0, similarly for the negative values. The "Switch" function in Simulink will act as a "sorter." It has 3 inputs as shown in Figure 3.10. The middle input takes the logic from the comparator. If it receives a 1 from the "Compare To Zero" block, the Switch block enlarged and illustrated in Figure 3.9 will output the top input. If it receives a 0, it will output the bottom input which, in this case, is always 0. This is illustrated through the plot function block "Scope" in Figure 3.11.

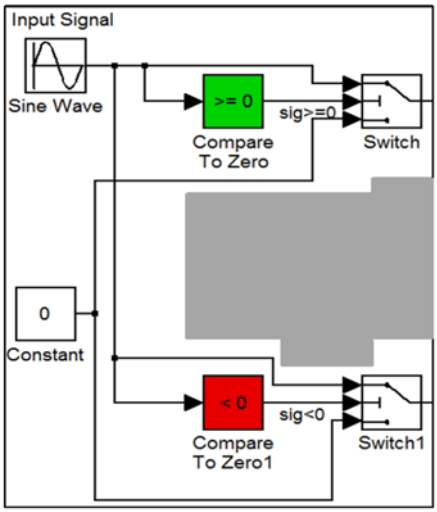

Figure 3. 9: Zoom-in the first segment of PWM Block Diagram.

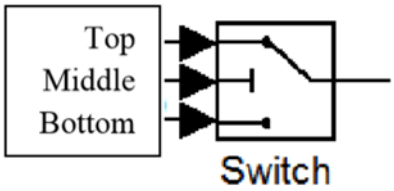

Figure 3. 10: Input Breakdown for Switch Function.

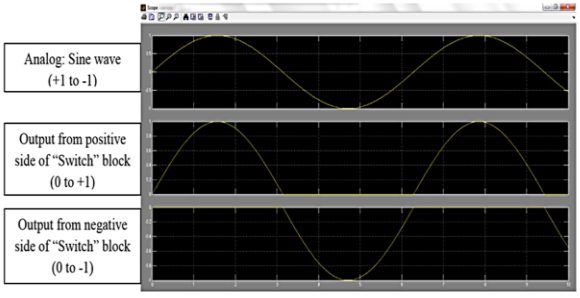

Figure 3. 11: Screen shot of analog wave and outputs of Switch Block.

In Figure 3.11, the sawtooth wave form is generated and since this block also generates a value that oscillates between +1 and -1, it needs to be separated into positive sawtooth wave form (0 to +1) and negative sawtooth wave form (0 to -1). "Abs" is a function block that puts everything in absolute value.

This later goes to a “Relational Operator” that will compare the purely positive or purely negative analog signal shown in Figure 3.12 with respect to a sawtooth signal, therefore resulting in a PWM signal for input C and input D, which later goes to the L298 Dual Full-Bridge Driver. As a convention, to match the functions described in the spec sheet of the chip, a positive analog signal is in charge of the forward motion, and a negative signal is in charge of the reverse motion.

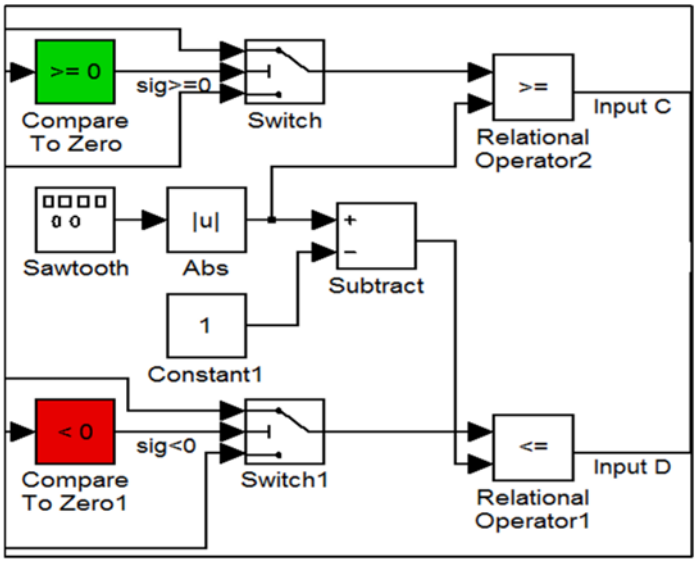

Figure 3. 12: Zoom-in second segment of PWM block diagram.

In order to prove that this logic works, a simple motor is used to test the L298 Dual Full-Bridge Driver and the Simulink model of PWM. The input is an analog sinusoidal wave. It was observed that the motor rotates from the static condition, first in one direction, accelerates and then decelerates, until it stops completely. When arriving at the point where the sine wave goes to negative sine, the motor goes in the opposite direction at the same pace of acceleration and deceleration as the positive signal. Besides physical observation, a voltmeter is placed across the motor. It shows that, as the motor turns faster, the voltage increases positively or negatively and slows down, as does the voltage shown on the voltmeter, until a stop with zero volts. Hence, this shows that both PWM Simulink program and the L298 Dual Full-Bridge Driver work well with each other. Thus, the L298 Dual Full-Bridge Driver fulfill their function of changing the direction of the current, resulting in a change in the direction of rotation of the motor.

3.2.3. Simulink for Four-Coil Configuration

Simulink is needed for another purpose other than converting an analog signal into a digital signal. It allows one to program the desired signal and thus control the electromagnets, (e.g., timing when they are on or off). The challenge involves designing a signal such that the pattern of the magnetic field generated at each coil can move the magnetic particles from point A to point B horizontally, and not vertically. In this section, the Simulink model is created based on a four-coil configuration. Figure 3.13 shows one of the physical setups of the four-coil configuration. If all coils hanging above the particles are activated at the same time, there will be only an up and down motion of the particles. Later during the experiment, even if the coils are activated one after another, with coils hang vertically above the magnetic particles, the particles still move only up and down (see Figure 3.14). The abrasion process will not occur in this case. This section emphasizes the pattern of the signal designed and provides an overall look at the Simulink file for the four-coil configuration. See Figure 3.13 for an example of the four-coil configuration setup.

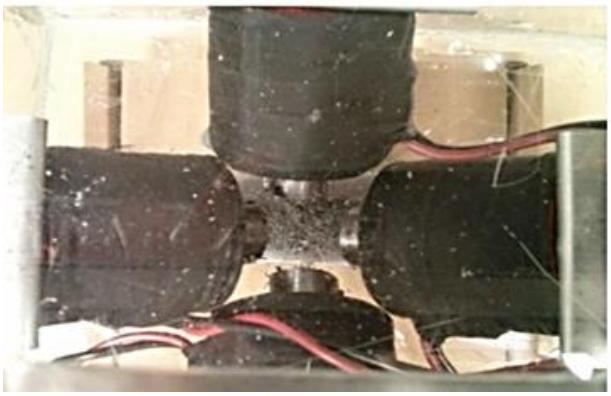

Figure 3. 13: Four-coil configuration hanging above MAPs.

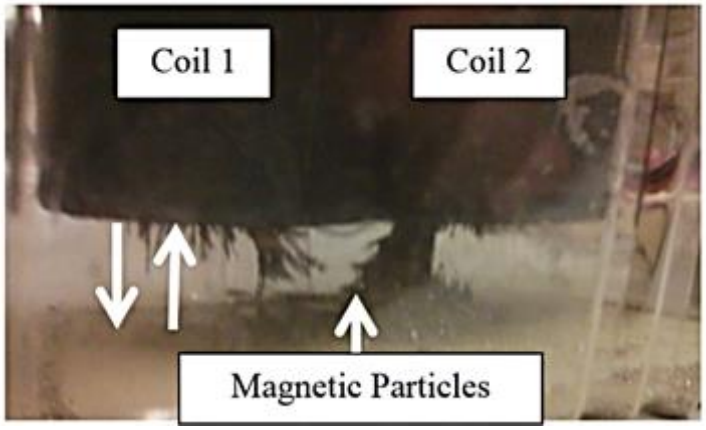

Figure 3. 14: Two-coils hanging above MAPs

The algorithm of conversion from analog signal to digital signal through PWM is incorporated into the overall Simulink file for the four-coil configuration shown in Figure 3.15. It is reduced into a simple block circled by an orange rectangle.

On the left of Figure 3.15, the four blocks circled by a purple rectangle are the general pattern of the signal for each coil. In other words, it dictates when the current passes through the coil and when it does not. With the four-coil configuration, the particles need to move from one coil to the neighbouring coil to allow for some abrasion process by the particles motion. The ideal pattern is to ensure that there is a motion in the particles and that there is no residual magnetism within each coil. To avoid residual magnetism, an equal amount of time must be spent on the positive signal and negative signal. Note in Figure 3.15 that, there are four blocks circles by green rectangles. During the initial test runs of the Simulink model, magnetisation is not created. The coils run based on the signals coming from the blocks circled with a purple rectangle, producing the general pattern.

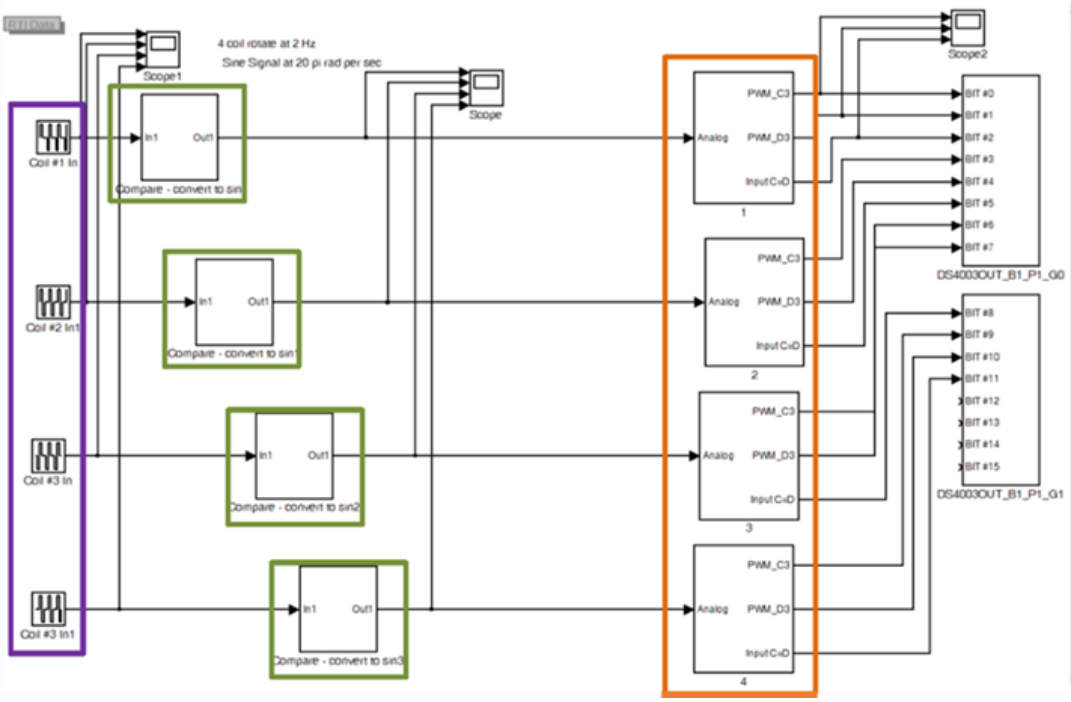

Figure 3. 15: Simulink block diagram for four-coil configuration.

After each experiment, there was still a small residual magnetism even if the direction of the current was continuously changing to ensure an equal amount of time spent on a North Pole and South Pole as illustrated in Figure 3.16.

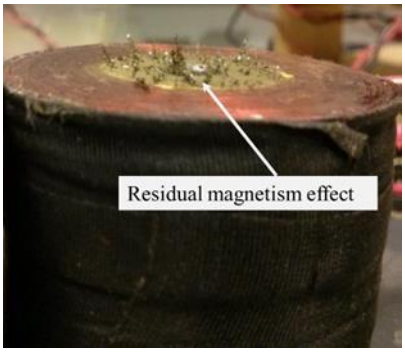

Figure 3. 16: Amount of particles resting on the core of the coil due to the residual magnetism.

To further reduce the residual magnetism, an additional subsystem block was introduced to each coil signal algorithm, encircled by the green rectangle in Figure 3.15. The main idea was to change a constant +1 or constant -1 signal into a high frequency sinusoidal wave that goes from +1 to -1 for the duration when the main pattern shows +1 or -1. The idea was to prevent letting the coils remain idle in a single polarity for too long. An attraction force is needed from the coils, but they should not stay in single polarity. They need to change polarity between North and South rapidly for the period that each coil is activated. For the reminder of the thesis, this sine wave frequency, the rate at which the polarity changes, is called the coil frequency.

To make magnetic particles move, only two neighbouring coils will be activated or become electromagnets at any given time. For example, Coil 1 and 2, at time 1, will have North Pole and the others will be neutral, not activated. At time 2, the next pair of coils, Coil 2 and 3, will have the South Pole. Coil 2 will change from North Pole to South Pole. The general pattern is summarized in Table 3.2. The pattern was programmed and represented by the blocks encircled by the purple rectangle. It is important to note that there is an attraction force to the magnetic particles regardless of which pole the coil has. The alternation of pole, minimizes residual magnetism at the core. To further avoid magnetisation of the electromagnets, the general pattern signal enters a function block that converts a +1 signal or a -1 signal into a high frequency sinusoidal wave that goes from +1 to -1. The transformed signal then enters the PWM conversion block that is explained in Section 3.2.2.

Table 3.2: General pattern for four-coil configuration.

Coil #/ Time	1	2	3	4	5	6	7	8
Coil 1	North	Neutral	Neutral	South	North	Neutral	Neutral	South
Coil 2	North	South	Neutral	Neutral	North	South	Neutral	Neutral
Coil 3	Neutral	South	North	Neutral	Neutral	South	North	Neutral
Coil 4	Neutral	Neutral	North	South	Neutral	Neutral	North	South
Signal for: North Pole = +1, Neutral (no current supply) = 0, and South Pole = -1								

3.3. Coils Configuration

3.3.1. Three-Coils Configuration

This setup, shown in Figure 3.17, was the first trial of the magnetic abrasion finishing operation. It began with three coils set up in a linear alignment as shown in Figure 3.17. The signal from Simulink was set up such that only one coil was active at a time and in the sequence of one after another.

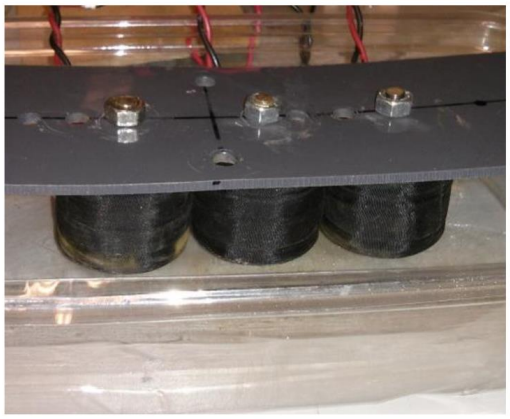

Figure 3. 17: Three-coils in linear alignment.

By observation, the coils were activated one after another and there was minimal residual magnetization on the coils. However, MAPs under the coils only moved up and down, (e.g., up when the electromagnet was active). There was no horizontal motion of the particles. Hence, this configuration was deemed not suitable for magnetic abrasion. The second configuration with three-coils was installed in a triangular alignment as illustrated in Figure 3.18. Similar behaviour of the particles was observed as in the linear setup.

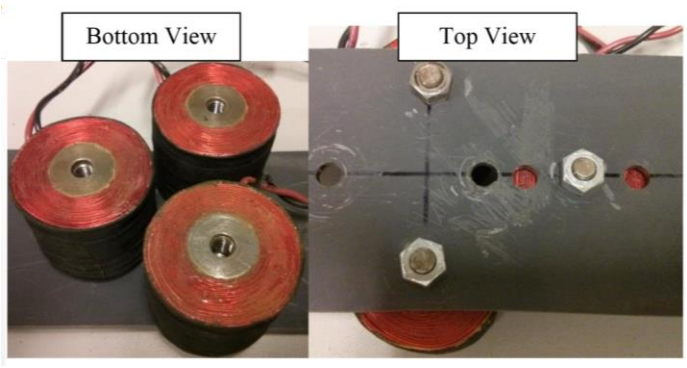

Figure 3. 18: Three-coils in triangular alignment.

3.3.2. Four-Coil Configuration

The following configurations all follow the Simulink program analyzed in Section 3.2.3. The key variation was the magnetic field was generated from various physical setups of the coils. Placing the coils to obtain the best motion for the magnetic particles was a critical issue.

By placing the coils horizontally, as shown in Figure 3.19, the particles started to move but the motion is small and the particles stay around the nearest coil. There was still no distinct motion of the particles going from one coil to the neighboring coil.

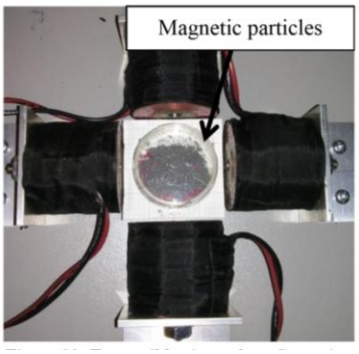

Figure 3. 19: Four-coils in horizontal configuration.

To improve the particles' movement, an extension of the core was added, as shown in Figure 3.20. A screw was added to each coil at its center tip. The goal was to focus the magnetic field. With a flat surface, the magnetic flux leaked, thus explaining the weak motion of the particles.

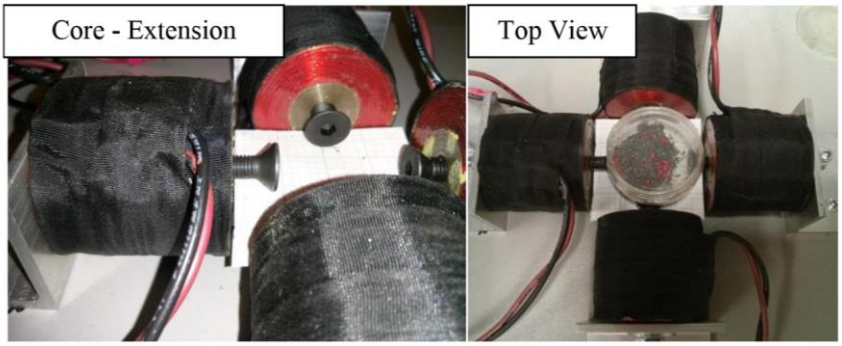

Figure 3. 20: Four-coils with extended core.

Out of curiosity, a six-coil configuration was created, as shown in Figure 3.21. A rough sketch of the magnetic field of the configuration was made, and a rough circular magnetic field was created. Not surprisingly, a circular pattern made of magnetic particles was created. In addition, the particles travelled from one coil to the next but did not travel to all coils, staying close to two or three coils. It was interesting to observe the circular pattern created by the magnetic particles.

Figure 3. 21: Six-Coil Configuration

3.4. System Setup

The configuration of four coils was used in the SMAF apparatus. The apparatus structure was made from aluminum to ensure no magnetization effect could be generated due to the structure frame since aluminum is a non-ferromagnetic material.

The apparatus contains four columns, as illustrated in Figure 3.22, and each column holding a movable arm carried an electromagnet at the end. The movable arm is easily moved up and down, front and back, or adjusted with an angle according to the workpiece geometry. The arm can be fixed to the column with two screws to prevent loosening during the operation running. The column also has many slots to hold the workpiece or workpiece holder and improve fit-up.

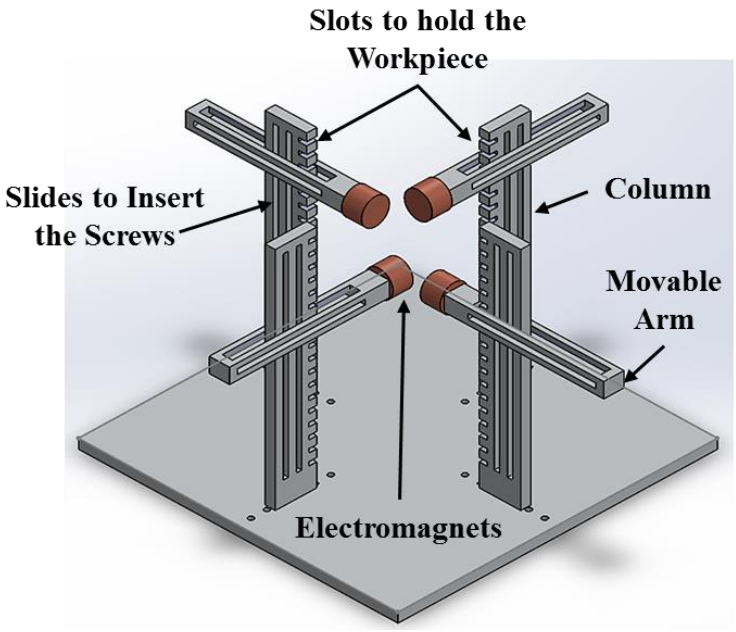

Figure 3. 22: Schematic of the SMAF apparatus.

To make the apparatus set up adjustable and suitable to finish assorted workpiece geometries, the electromagnetic coils can be located under or above the workpiece and MAPs, as shown in Figure 3.23. In this configuration, instead of setting up the coils horizontally planar, the arms are set at an angle θ which is to be optimized later in Chapter 4 (it will be seen to be approximately 60° from the plane).

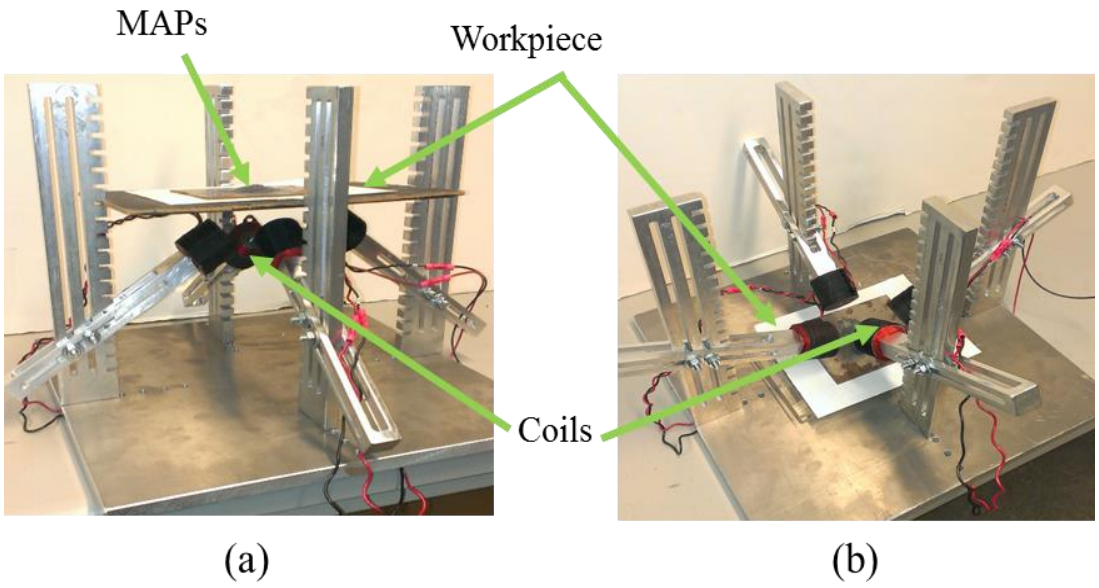

Figure 3. 23: Four-coil configuration, (a) Coils hang under the workpiece and MAPs, (b) Coils are located above the workpiece.

3.5. Experimental Outcomes using Four-Coils Configuration

The MAF process was applied to finish an Aluminum workpiece. The process parameters were 28 Volts applied for 30 min with 2 Hz frequency. Figure 3.24 shows scanning electron microscope (SEM) photographs of the surface before and after the MAF process to understand the wear pattern on the surface at the Micro/Nano level.

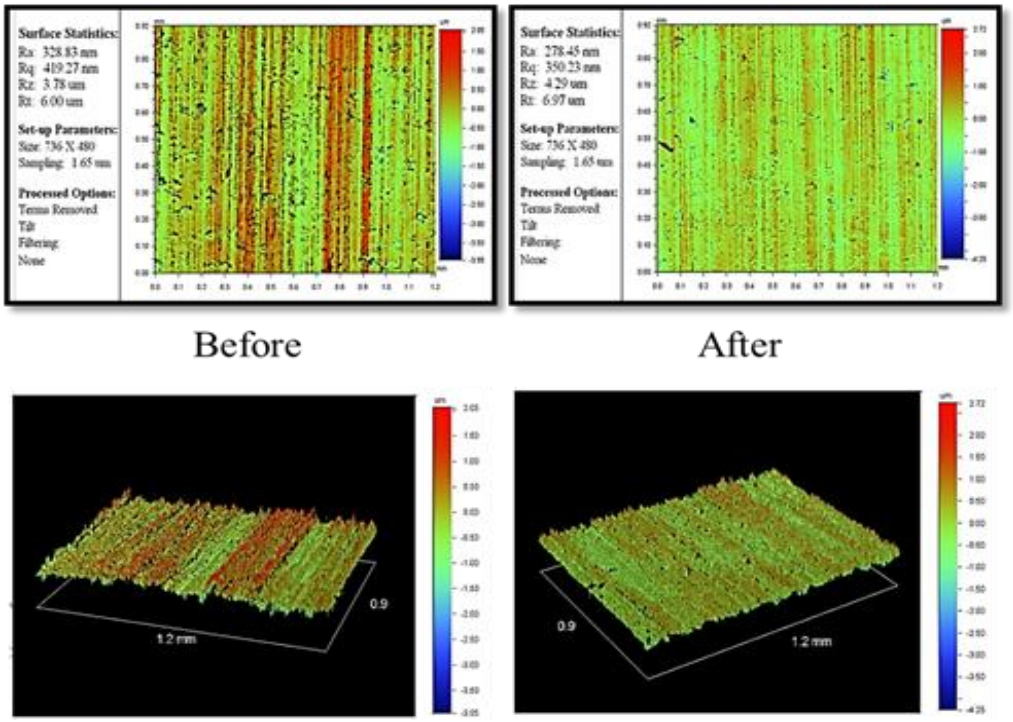

Figure 3. 24: SEM photographs of the surface before and after the MAF process.

SEM photographs of the surface show deeper scratches and dents made as the ferrous particles pressed on the magnetic abrasive. The Maps used were Iron particles mixed with sand, which were available in the lab. It was concluded that the magnetic force generated with Iron particles was sufficient to remove the peaks and improve the surface roughness from 328.83 nm to 278.45 nm.

3.6. Conclusions

This chapter explains the possibility of using stationary electromagnets and a workpiece by manipulating the excitation current to produce a rotating magnetic field. Various physical configurations of the coils included: from three coils to six coils, vertical coils, horizontal coils and coils elevated at an angle pointed toward the particles. The different setup configurations were controlled through a MATLAB-Simulink program. A data acquisition device called dSPACE was used as a companion in order to run the

experiment. L298 Multi-watt 15 Dual Full-Bridge Driver were used to resolve the issue with residual magnetism.

The hysteresis loop provided explained why the issue with residual magnetism occurres: the fact that the current passes through coils in only one direction. The Full-Bridge Driver allowed a bi-directional control of the current. Using this chip significantly reduced the accumulation of magnetism at the core of the coil.

Several physical configurations were investigated: three-coil configuration, four-coil configuration and six-coil configuration. In the four angled-coil configuration, with coils hanging above or lying under the magnetic particles, there was an issue with uneven distribution of particles. A number of particles were found outside of the abrasion zone, making the abrasion process less efficient. By extending the core of each coil, this problem was avoided, and the extended core kept the magnetic particles closer to the abrasion zone. This modification also refocused the magnetic field generated at each coil and prevented leakage of magnetic flux.

Lastly, the four-coil configuration aligned by 30° with the Z-axis (approximately 60° from the plane) was the best choice to carry out the experiments and to prove the concept.

The results show that, by using stationary electromagnets and a workpiece, the magnetic particles can perform the finishing process. The movement of the magnetic particles becomes possible by regulating the exciting current of the coils in order to produce a rotating magnetic field.

Chapter 4

Design and Optimization of Electromagnetic Actuator

4.1. Introduction

Magnetic force, in the SMAF technique, represents the finishing force. Basically, the main components of the cutting force which are responsible for removing the material and complementing the finishing process are the normal and tangential cutting forces [47]. Many studies have been conducted to model and measure the finishing force in the working area. Mori et al. [24] developed a model to determine and measure the finishing force depending on the number of abrasive particles in the finishing zone and explained how the magnetic abrasive flexible brush forms using an energy method. Ganguly et al. [48] established a method to measure and separate the finishing force components based on the signal of the magnetic force. Furthermore, they examined the effect of the finishing parameters, such as the air gap and ferromagnetic particle size, on the finishing force and surface roughness. Kala and Pandey [49] carried out their experimental work using a double disk magnetic abrasive finishing process to measure the torque and finishing force using a dynamometer (Shunk: DELTA sensor). They found that the working gap affects the normal finishing force and finishing torque. Controlling the finishing force depends on controlling the magnetic field, so MAF does not need cutting tools with a numerical controller [50]. Moreover, the finishing force applies a pressure on the abrasive particles and this pressure is a function of the magnetic field density, permeability of the macro-size mixture of abrasive particles, and the amount of this mixture. The magnitude of the applied pressure should be sufficient for the abrasive particles to penetrate into the workpiece [51]. The movement of the macro-size mixture of abrasive particles on the workpiece surface, under the effect of the applied pressure, produces a temperature rise in the interfering zone due to friction [52]. This thermal variation might negatively affect the quality of the finished surface.

This concept has been studied by many researchers to study the effect of this factor on the finishing mechanism and finished surface quality. Hou and Komanduri [53] conducted a theoretical model to calculate the flash temperature produced by an assumed heat source as a small disk sliding on the workpiece surface. They found that the flash temperature is a function of the sliding speed of the presumed disk, finishing pressure, and the length of the scratch that is produced by the movement of the abrasive particles on the workpiece surface during the finishing process. They showed that the temperature variation can reach

up to 980˚C under the finishing conditions of 5.24 m/s sliding speed, and 0.5-1.2 T magnetic field range, using unbounded Cr_2O_3 abrasive particles to finish a workpiece of Si_3N_4. Kumar and Yadav [52] proposed a finite element model to determine temperature variation during the finishing process of the Si_3N_4 workpiece using unbounded Cr_2O_3 abrasive particles. They determined the temperature variation to be within the range of 150-800˚C under the machining condition of 5305-6366 rpm electromagnet rotating speed and 0.8-1.0 T magnetic flux density. Mulik and Pandey [54] investigated the interfering zone between the magnetic abrasive finishing brush and the workpiece surface. They found that the temperature range was 31-42˚C during the MAF process with the finishing conditions of 0.2 T magnetic flux density and 180-450 rpm rotational speed of the magnet.

The optimization approach of the electromagnets is carried out in two stages. In the first stage, the integrated formula of a thin shell solenoid has been used to obtain the gradient of the magnetic field at any point on the axis of a finite solenoid. Whereas, in the second stage, a parametric study, is carried out to optimize the geometry of the electromagnet using a finite element simulation. Moreover, a new approach was used to measure the magnetic field experimentally. Also, the variation of temperature of the Titanium CP grade 2 workpiece was measured using a thermal camera.

4.2. Modeling and Electromagnet Parametric Optimization

Since the cutting force in the MAF technique depends on the gradient of the magnetic field, as illustrated in Equation (4.1), one of the most important and effective considerations for producing a magnetic field is the design of the electromagnet and the geometry of the solenoid configuration. The other design considerations, which affect the cutting force, are the amount of current passing through the coil of the electromagnet, and the internal magnetization of the ferromagnetic particles in the macro-size mixture (of iron and abrasive particles).

4.2.1. Governing Equations and Magnetic Force

The magnetic force *F* which acts on the macro-size mixture of iron and abrasive particles can be expressed as the gradient of the magnetic potential energy [55]:

$$F_m = \int_V (M \cdot \nabla) B_{ext} \, dV \tag{4.1}$$

and

$$(M \cdot \nabla)B_{ext} = \left(M_x \frac{\partial}{\partial x} + M_y \frac{\partial}{\partial y} + M_z \frac{\partial}{\partial z}\right) B_{ext_x} \hat{\boldsymbol{x}} + \left(M_x \frac{\partial}{\partial x} + M_y \frac{\partial}{\partial y} + M_z \frac{\partial}{\partial z}\right) B_{ext_y} \hat{\boldsymbol{y}} + \left(M_x \frac{\partial}{\partial x} + M_y \frac{\partial}{\partial y} + M_z \frac{\partial}{\partial z}\right) B_{ext_z} \hat{\boldsymbol{z}} \quad (4.2)$$

where F_m is the magnetic force acting on the macro-size mixture of iron and abrasive particles in the working area, B_{ext} is the external magnetic field, M is the magnetization of the ferromagnetic particles, and V is the volume of the ferromagnetic abrasive particle. The particles (iron particles) can be considered as a magnetic dipole under the effect of the external magnetic field (B_{ext}).

Variation of B_{ext} in the working area can be evaluated by using the formulation of magnetic field density (B) of a finite solenoid acting on an external axial point [56] as illustrated in Figure 4.1.

$$B = \frac{\mu_o \, IN}{2(r_o - r_i)} \left[X_2 \ln \left(\frac{\sqrt{r_o^2 + X_2^2} + r_o}{\sqrt{r_i^2 + X_2^2} + r_i} \right) - X_1 \ln \left(\frac{\sqrt{r_o^2 + X_1^2} + r_o}{\sqrt{r_i^2 + X_1^2} + r_i} \right) \right] \quad (4.3)$$

where B is the magnetic field at any point on the axis of the solenoid (T), μ_o is the permeability constant, I is the current in the wire (A), N is the number of turns of wire per unit length in the solenoid. r_i, is the inner radius (m). r_o, is the outer radius (m) and $X1$ and $X2$, are the distances, on axis, from the ends of the solenoid to the magnetic field measurement point (m).

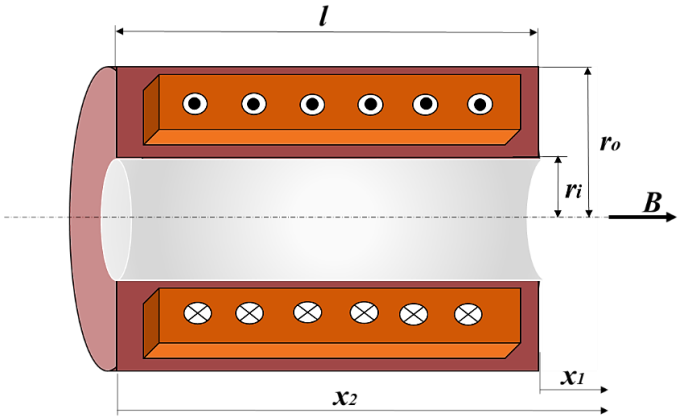

Figure 4. 1: Basic parameters of the finite solenoid.

4.2.2. Electromagnet Design

It is very important to optimize the electromagnet parameters in order to produce a sufficient magnetic field in the working area and accomplish the finishing process. The electromagnet geometry ratio and the aspect ratio should be defined to describe the geometry of the solenoid configuration. In Equations (4.4) and (4.5), α represents the ratio of the outer solenoid radius r_o to the inner radius r_i, and β represents the ratio of the solenoid length l to the inner radius r_i. These variables (α and β) represent the optimization parameters.

$$\alpha = \frac{r_o}{r_i} \tag{4.4}$$

$$\beta = \frac{l}{2r_i} \tag{4.5}$$

The solenoid is considered to have many turns in axial and radial directions. $N_Z = \frac{l}{d_w}$, indicates the number of turns in the axial direction, while $N_r = \frac{r_o - r_i}{d_w}$, indicates the number of turns in the radial direction, where d_w represents diameter of the coil wire (m). The total number of turns will be $N = N_Z * N_r$ and the volume current density will be $NI/[l(r_o - r_i)]$, where I is the coil current. Moreover, coil inductance L can be calculated (in Henrys) as $L = \frac{N^2 \mu A}{l}$, where μ is the absolute permeability of the core material and A is the cross-sectional area of the coil in square meters [57].

The formulation of magnetic field density (B) of a finite cylindrical solenoid is basically used for the air-core solenoid; however, it could be used for the iron-core solenoid if a factor of ($B_{with\ core}/B_{without\ core}$) has been used. This factor represents the relative permeability of the solenoid iron-core, which denotes as μ_{r-core} and $\mu_{r-core} = \frac{\mu}{\mu_o}$, where μ and μ_o represent the iron absolute permeability and free space permeability, respectively [57]. This fact has been verified experimentally, analytically, and numerically before using this formula to identify the optimum parameters for the electromagnet. Experimental verification has been done by applying a DC current with different values, (1, 1.5, and 2 A) with the use of a Gauss meter to measure B for different points along the axial (on-axis) direction of an electromagnet with an iron core. Further, the analytical verification has been done by using the formulation of B of a finite cylindrical air-core solenoid while considering the ($B_{with\ core}/B_{without\ core}$) factor. Furthermore, the numerical verification was conducted by using a finite element simulation in COMSOL Multi-Physics. As shown in Figure 4.2, the variation of B can be accepted for these

approaches and this formula can be considered valid to be used to find the optimum parameters of the electromagnet.

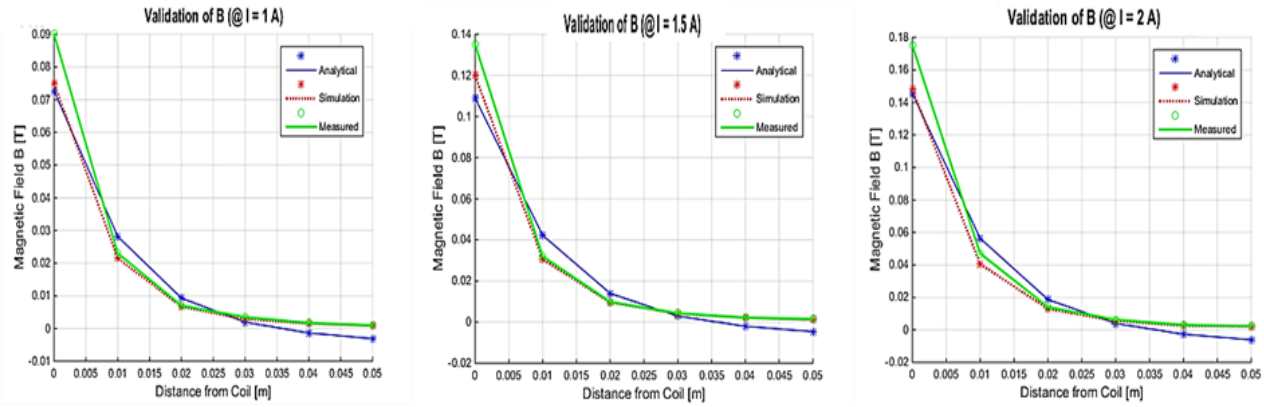

Figure 4. 2: Verification of B with different values of *I*.

The magnetic force F_m acting on the macro-size mixture of iron and abrasive particles to remove the material from the surface of the work piece, is a function of several coil parameters:

$$F_m = f(B_{ext}, I, N_r, N_z, r_i, r_o, l, g, r_w, l_w, \rho) \tag{4.6}$$

where B_{ext} is the external magnetic field (Tesla), I is the current passing through the electromagnetic solenoid (A), *Nr* and *Nz* are the number of turns in the radial and axial directions, respectively, $r_i, r_o,$ and l are the inner radius, outer radius, and length of the electromagnetic solenoid, respectively, in meters, g is the axial air gap distance between the edges of the electromagnetic core and the work piece (meters), r_w and l_w are the radius and length of the wire used to wind the electromagnetic solenoid, , respectively, in meters, and ρ is the resistivity of the wire (Ω m). The number of coil turns can be adjusted to fit the electromagnet dimensions. In this case the number of turns was chosen to be 1000 turns ($N_Z * N_r = 1000$). The air gap between the electromagnet and the work piece was not expected to exceed more than 10 mm, and therefore the air gap was fixed at 10 mm in order to simplify the optimization process. The wire parameters (r_w, l_w, and ρ) can be determined later, after the optimization, based on the total number of turns and the American Wire Gauge (AWG) standard. By eliminating the known parameters, the axial magnetic force F_m in Equation (4.6) between the electromagnet and the work piece coil is:

$$F_m = f(B_{ext}, I, r_i, r_o, l) \tag{4.7}$$

Due to some design considerations regarding the size of the working area and the total size of the system, the electromagnet volume was fixed at V_c = 50 cm^3 and the wire length was fixed at 500 m.

The optimization process to design the electromagnet for the MAF process was carried out in two stages. In the first stage, the integrated formula of a thin shell solenoid was used to obtain the gradient of the magnetic field at any point on the axis of a finite solenoid. While in the second stage, a parametric study was carried out to optimize the geometry of the electromagnet using a finite element simulation.

4.2.3. Thin shell finite solenoid formula

Variation of B_{ext} in the working area can be evaluated by using the formulation of the magnetic field density (B) of a finite solenoid acting on an external axial point, Equation (4.3) [56], as illustrated in Figure 4.1. It can be seen from Equations (4.1) and (5.2) that F_m depends on the gradient of the magnetic field density (∇B), which means Equation (4.3) can be used to determine the optimization parameters of the coil geometry α and β (Equation (4.4) and (4.5)).

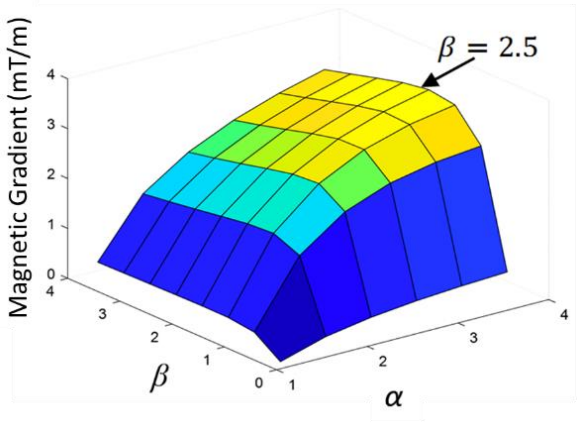

Figure 4. 3: Magnetic gradient versus the parameters of coil geometry α and β

The optimization result is shown in Figure 4.3. It is clear that the maximum magnetic gradient is 3.4 mT/m. It can be noticed that this optimization process gives the optimum value just for β, which is around 2.5. While for α, it is clear that no optimum value exists and the gradient increases when α increases. This is because ($\alpha = \frac{r_o}{r_i}$) and an increasing α occurs when the variation between r_o and r_i increases, or, when r_o

increases and r_i decreases. Decreasing r_i means the magnetic field lines concentrate and in consequence, the magnetic gradient increases [58].

4.2.4. Finite element simulation

To obtain the optimum value of α, a parametric study was carried out to optimize the geometry of the electromagnet with iron core using finite element simulation. The geometry parameters, ($\alpha = \frac{r_o}{r_i}$) and ($\beta = \frac{l}{2r_i}$) were considered in this approach to provide a maximum magnetic force, F_m, on a single iron particle in the working area. The following assumptions were considered during the FEM simulation:

- The diameter of the iron particle was kept fixed as 1 mm.
- The location of the iron particle was kept fixed on the center point of the iron core, also the gap between the particle and iron core was fixed as 10 mm.
- Coil power and current were kept as 2.9568 W and 1.5 A, respectively, according to the power supply and the L298 Dual Full-Bridge Driver. At the same time the number of coil turns N was adjusted according to the geometry parameters α and β (r_o, r_i and l), as illustrated in Table 4.1.

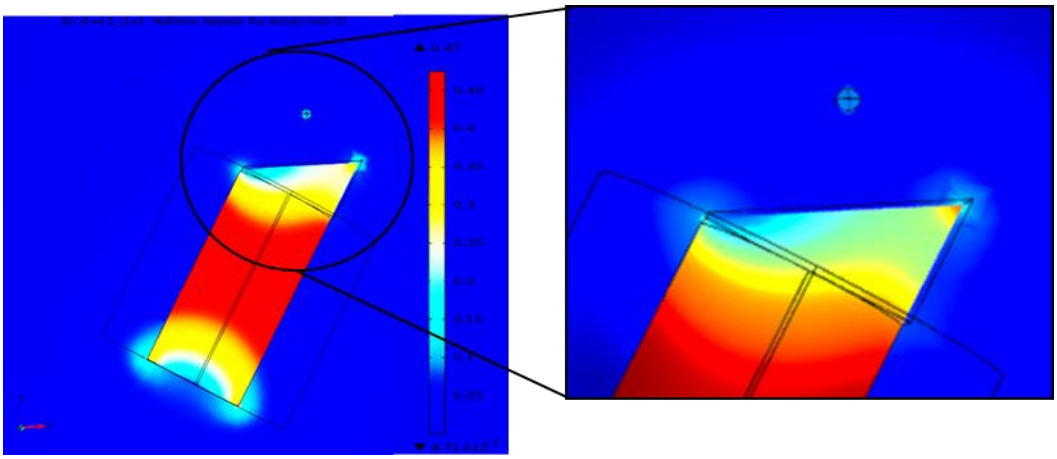

Figure 4. 4: Magnetic flux distribution contour for iron core and iron particle.

Different combinations of the electromagnet geometry parameters α and β (r_o, r_i and l) were considered during the simulation. The variation of α was from 2 - 4 with step 1, in the same manner β varied in the range of 1.5-3 with a 0.5 step. The simulation for this analysis and the magnetic flux distribution contour

for the iron core and the iron particle are shown in Figure 4.4. The simulation results show that the maximum value of the magnetic force F_m (0.463 mN) on the iron particle can be obtained in this case at α = 2 and β = 2.5, as illustrated in Table 4.1.

Table 4.1: Simulation results

β=b/2ri	α=ro/ri	t=ro-ri	b=L [cm]	ro [cm]	ri [cm]	N	Fm [mN]	Coil Power [W]
1.5	2	0.5	1.5	1	0.5	367	0.403	2.95683
		1	3	2	1	184	0.166	2.95683
		1.5	4.5	3	1.5	122	0.0591	2.94877
	3	1	1.5	1.5	0.5	275	0.238	2.95414
		2	3	3	1	138	0.0908	2.96488
		3	4.5	4.5	1.5	92	0.0305	2.96488
	4	1.5	1.5	2	0.5	220	0.159	2.95414
		3	3	4	1	110	0.0542	2.95414
		4.5	4.5	6	1.5	73	0.0165	2.9407
2	2	0.5	2	1	0.5	367	0.438	2.95683
		1	4	2	1	184	0.166	2.96488
		1.5	6	3	1.5	122	0.0553	2.94877
	3	1	2	1.5	0.5	275	0.254	2.95414
		2	4	3	1	138	0.0906	2.96488
		3	6	4.5	1.5	92	0.0287	2.96488
	4	1.5	2	2	0.5	220	0.168	2.95414
		3	4	4	1	110	0.0542	2.95414
		4.5	6	6	1.5	73	0.0156	2.94071
2.5	**2**	**0.5**	**2.5**	**1**	**0.5**	**367**	**0.463**	**2.95683**
		1	5	2	1	184	0.163	2.96488
		1.5	7.5	3	1.5	122	0.0507	2.94877
	3	1	2.5	1.5	0.5	275	0.266	2.95414
		2	5	3	1	138	0.089	2.96488
		3	7.5	4.5	1.5	92	0.0264	2.96488
	4	1.5	2.5	2	0.5	220	0.174	2.95414
		3	5	4	1	110	0.0533	2.95414
		4.5	7.5	6	1.5	73	0.0144	2.94071

The results of the simulation approach confirmed the optimum value of β to be equal to 2.5 and provided the optimum value of α as 2. Further provided are the electromagnet geometry parameters (electromagnet dimensions) r_o, r_i and l as *1, 0.5* and *2.5 cm* respectively.

4.3. Verification of optimization results

To verify the optimization results which were obtained from both approaches, the optimized values were compared with the optimal values of the typical geometry of the ferromagnetic core coil formulas. These formulas were defined as ($2r_i \cong 0.6r_o$) and ($\frac{l}{l_c} = 0.7 \sim 0.9$) [58], where l_c represents the length of the ferromagnetic core. Before verifying the optimization results, the number of turns *N* was adjusted to ensure fit for the total sectional area of the winding, for specific values of the total wire length (l_w), α and β.

Therefore, the number of turns (*N*) and the total wire length (l_w) were calculated according to:

$$N = \frac{4l(r_o - r_i)}{\pi d_w^2}\lambda \tag{4.8}$$

$$l_w = 2\pi N\left(r_i + \frac{r_o - r_i}{2}\right) \tag{4.9}$$

where λ represents the space factor which is defined as the ratio of active section of the winding to the total section of the winding area, and its value varies between 0.8 - 0.9 depending on the winding technique.

Two approaches were carried out to verify the optimum values. In the first approach, after calculating *N* and l_w according to Equation (4.8) and (4.9), *N* was changed relative to the change of the outer diameter. The total wire length (l_w) and coil power (*P*) were kept constant and a finite element simulation was carried out to verify the magnetic force F_m. In this approach, β and *l* were kept as 2.5 for both, while α was changed from 2 - 3 with step 0.5. As illustrated in Table 4.2, the magnetic force F_m decreases as *N* decreases, because as shown in Equation (4.6), F_m depends on *N*. Also, the induced voltage *V* depends mainly on the number of turns of the coil, $V = NA\frac{dB}{dt}$, and since the total wire length is constant, as the outer radius increases the number of turns decreases.

Table 4.2: Simulation results with respect to constant (l_w) and (*P*)

β=b/2ri	α=ro/ri	t=ro-ri	b=L [cm]	ro [cm]	ri [cm]	N	F_m [mN]	Coil Power [W]
2.5	2	0.5	2.5	1	0.5	612	0.488	9.20376
2.5	2.5	0.7	2.5	1.25	0.5	542	0.407	9.2296
2.5	3	1	2.5	1.5	0.5	461	0.304	9.24394

In the second approach, after calculating N and l_w according to Equations (4.8) and (4.9), the finite element simulation was carried out to verify the magnetic force F_m. Similar to the first approach, β and l were kept as 2.5 for both, while α was changed from 2 - 3 with step 0.5. N and l_w were changed relative with the change of the outer diameter and according to that, coil power (P) was also changed. As illustrated in Table 4.3, the magnetic force F_m increases as N increases. Accordingly, the optimum values of the electromagnet geometry parameters (α, β, l, r_o, and r_i) for the current case to maximize the magnetic force in the working area are (*3, 2.5, 2.5 cm, 1.5 cm,* and *0.5 cm*), respectively.

Table 4.3: Simulation results with respect to the variables (l_w) and (P)

β=b/2ri	α=ro/ri	t=ro-ri	b=L [cm]	ro [cm]	ri [cm]	N	F [mN]	Coil Power [W]
2.5	2	0.5	2.5	1	0.5	612	0.488	9.20376
2.5	2.5	0.7	2.5	1.25	0.5	857	1.021	15.0364
2.5	3	1	2.5	1.5	0.5	1224	2.143	24.54357

Applying the obtained values of (r_o, r_i, l_c and l) of the current case, as illustrated in Figure 4.5, to the typical geometry parameters of the ferromagnetic core coil formulas, ($2r_i \cong 0.6r_o$) and ($\frac{l}{l_c} = 0.7 \sim 0.9$) [58], l_c is considered in this case as 3.5 cm. The results were ($r_i = 0.333r_o$) and ($\frac{l}{l_c} = 0.714$). These results were deemed acceptable and valid.

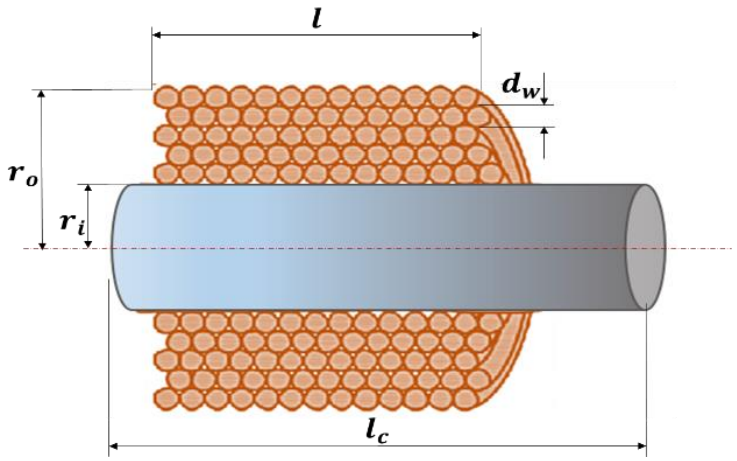

Figure 4. 5: The coil parameters (with iron core)

Furthermore, the Fabry factor (Geometry factor) *G (α, β)* shows that the maximum value of *G* = 0.179, as illustrated in Figure 4.6. In other words, the *G* factor of the optimal electromagnet geometry, from the power consuming point of view, should be around this value [13-14]. Applying the *G* factor formula, Equation (4.10), to the optimized values which are obtained from the optimization process (*α = 3* and *β = 2.5*), the result was *G = 0.175*. This result can also be deemed acceptable, with confidence.

$$G(\alpha,\beta) = \frac{1}{5}\left(\frac{2\pi\beta}{\alpha^2-1}\right)^{\frac{1}{2}} \ln\frac{\alpha+\sqrt{\alpha^2+\beta^2}}{1+\sqrt{1+\beta^2}} \tag{4.10}$$

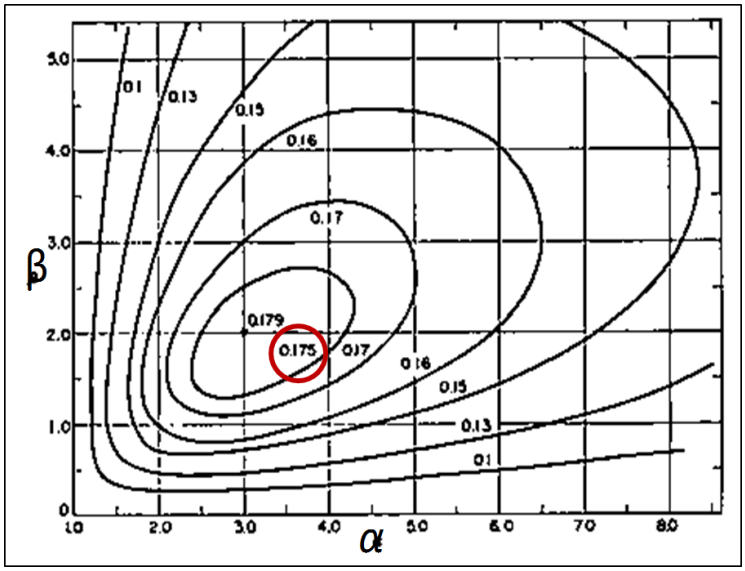

Figure 4. 6: The value of Fabry factor for a uniform current density coil [59].

The final step in building the electromagnetic coil with the previous dimensions was to determine the AWG wire that would fit these dimensions. The given value of the current was 1.5 A, and the approximate value of AWG wire which can sustain this current is either AWG22, or AWG24. The diameter of the AWG22 wire is ($d_w = 0.64$ mm) and it can sustain current up to 5 A. Alternatively, AWG24 wire diameter is ($d_w = 0.51$ mm) and it can sustain current up to 2.1 A. Therefore, it was necessary to determine the number of turns in the radial ($N_r = \frac{r_o - r_i}{d_w}$) and axial ($N_z = \frac{l}{d_w}$) directions and the total number of turns($N = N_r \times N_z$), then compare the results with the optimized value of the number of turns. Thus, ($N_{AWG22} \cong 610$) and

($N_{AWG24} \cong 960$) and it is clear that the nearest value to the optimized number of turns ($N = 1224$) is N_{AWG24} as illustrated in Table 4.3.

4.4. Best alignment angle of the electromagnets

To obtain a maximum *B* which could provide a maximum amount of the tangential *(Fm_t)* magnetic force component, angle θ of alignment for the electromagnet with the *Z* axis was examined for optimization. Optimal value of the magnetic force tangential component means to obtain a maximum amount of tangential force which must be sufficient to remove the material from workpiece surface tangentially.

The angle of alignment θ was varied from 0˚- 60˚, using a finite element simulation, and the magnetic force components were determined for each angle with respect to the iron particle. It was found that at θ= 30˚, F_t would be at its maximum value, providing the greatest assistance in performing the finishing process. as shown in Figures (4.7 - 4.9).

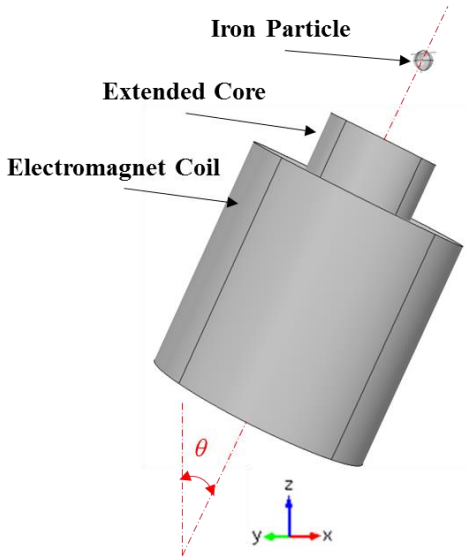

Figure 4. 7: Schematic of electromagnet aligned with angle θ from Z axis.

Tthe normal magnetic force component represents (*Fz*), whereas, the tangential component represents the resultant of (*Fx* and *Fy*) acting in the tangential direction. To accomplish the finishing process, both components are important, however, the tangential component must be greater than the normal one to force an abrasive particle to slide on the workpiece surface and remove the material instead of penetrating and sticking in the surface.

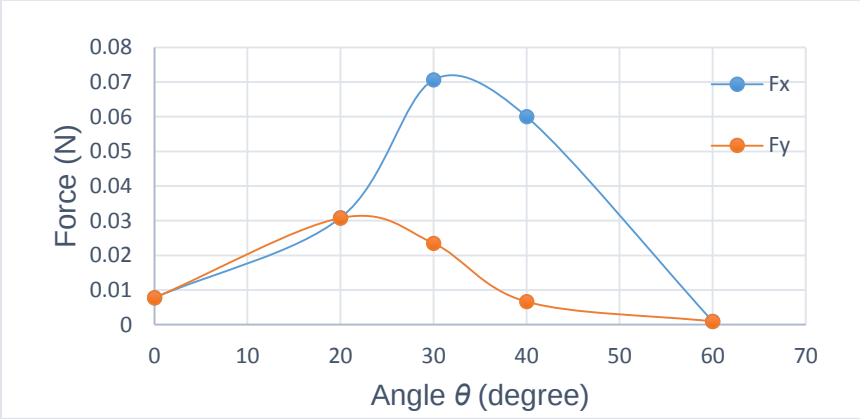

Figure 4. 8: The variation of force components with respect to angle θ.

Therefore, as one can notice from Figures 4.8 and 4.9 at $\theta = 30^{\circ}$ the tangential component is at a maximum value and is also larger than the normal component. A given electromagnet can thus be considered to be at the alignment angle.

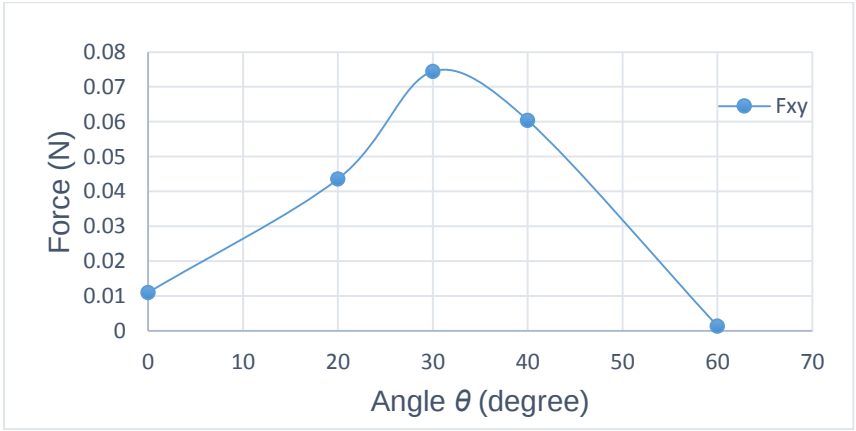

Figure 4. 9: The variation of force components, the tangential (Fxy) and the normal (Fz) with respect to angle θ.

4.5. Geometry of the extended core

In order to concentrate the magnetic field in the working area and reduce the leakage of magnetic flux, an extended iron core was proposed for the electromagnet. It was observed that, without using the extended core, the magnetic particles were attracted to the pole of the electromagnets, which is physically located on both ends of the coils. Because of this, half of the particles were found to be outside of the working area (where the abrasion needs to occur), as illustrated in Figure 4.10. This problem was solved by extending the core of the electromagnets by *1 cm*, so the total length ($l_c = 3.5cm$), and adjusting the angle of alignment θ of the electromagnet with the *Z* axis.

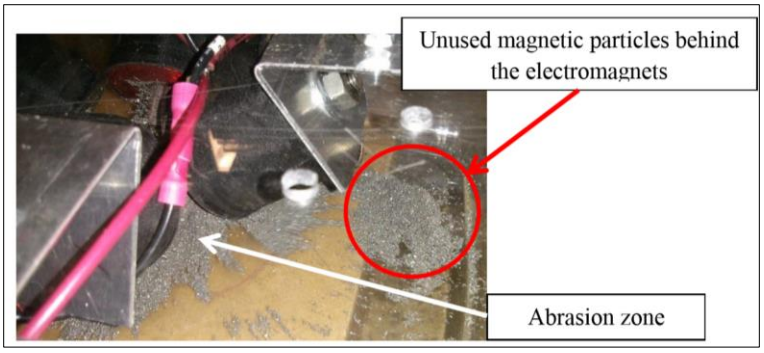

Figure 4. 10: Magnetic particles found to be outside of the working area.

To design an optimum geometry of the extended core (shape and dimensions), different configurations of the core tip were investigated, regarding the length of the extended tip, the core tip fillet radius, and the cross-sectional area. To determine the length of the extended tip, the typical geometry parameters of a ferromagnetic core coil formula, $(\frac{l}{l_c} = 0.7{\sim}0.9)$ [58] were considered, as long as the optimized value of l= 2.5 cm, and the extended tip is 1 cm, and the total core length $l_c = 3.5$ cm are determined at optimum.

Furthermore, the effect of the core tip fillet radius on the magnetic field was studied using a finite element simulation. It was found that the core tip fillet radius would significantly affect the distribution of the magnetic field lines in the working area. Consequently, increasing the tip fillet radius would decrease the

magnetic field line density in the machining zone, and the best fillet radius was r = 0, as shown in Figure 4.11.

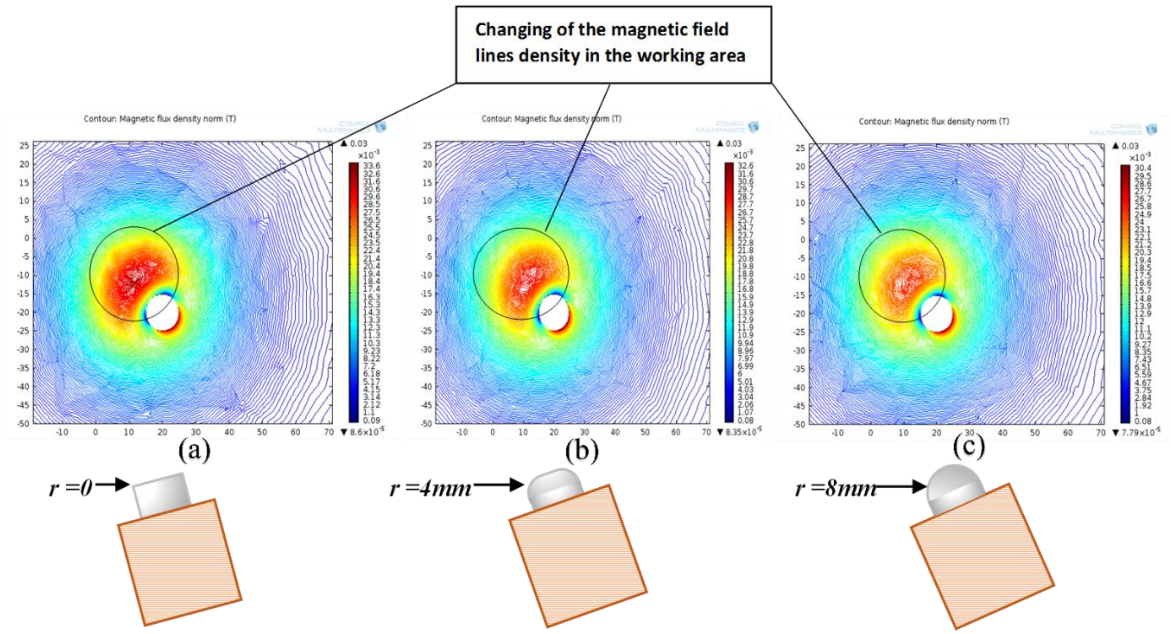

Figure 4. 11: The effect of the core tip fillet radius on B. (a) r = 0, (b) r = 4 mm, (c) r = 8 mm.

Similarly, the effect of the cross sectional area of the extended core was investegated using a finite element simulation (COMSOL Multiphysics). Three different geometries of the extended core were used to clarify how the magnetic field and force change with respect to a change of these geometries. The first is a cylindrical geometry, then cylindrical-chamfered geometry, and lastly square-chamfered geometry, as illustratied in Figure 4.12. It was observed that the square-chamfered geometry was the best in terms of the force uniformity in the working area. This uniformity was required to produce a uniform magnetic force and as a result a uniform finished surface.

Moreover, the effect of the distance between the work piece and the extended core of the electromagnet was investigated. This distance represents the air gap and it was required to find the magnetic force distribution in the working zone and air gap. A finite element simulation was used to study the magnetic force distribution in the working zone with respect to the change of the air gap distance. Three different values of air gap distance were used, 3, 5, and 7 mm. As illustrated in Figure 4.13, the reduction of the air gap produced a uniform distribution of magnetic force in the working area. On the contrary, it was found

that increasing the air gap concentrated the magnetic force at some points, which negatively affected the requirment of uniformity of the finished surface.

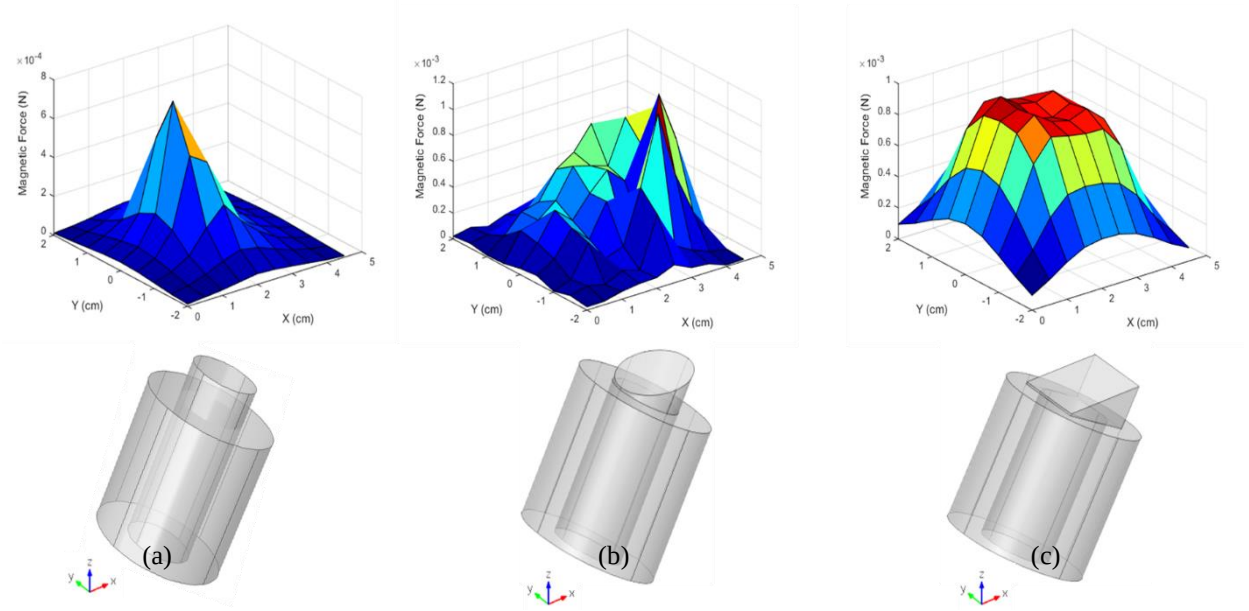

Figure 4. 12: Variation of magnetic force in the working area with respect to the geometry of the extended core (a) Cylindrical geometry, (b) Cylindrical -chamfered geometry, and (c) Square-chamfered geometry

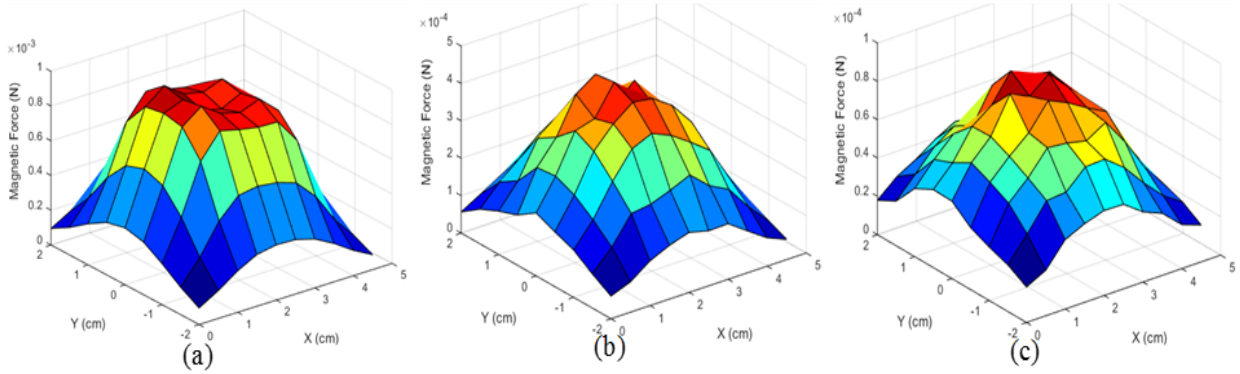

Figure 4. 13: Variation of magnetic force in the working area with respect to the air gap distance

(a) Air gap of 3 mm, (b) Air gap of 5 mm, and (c) Air gap of 7 mm

Thus, the optimum dimensions of the electromagnet parameters were found to be as illustrated in Figure 4.14, and the optimum configuration of the system setup will be as iluustrated in Figure 4.15.

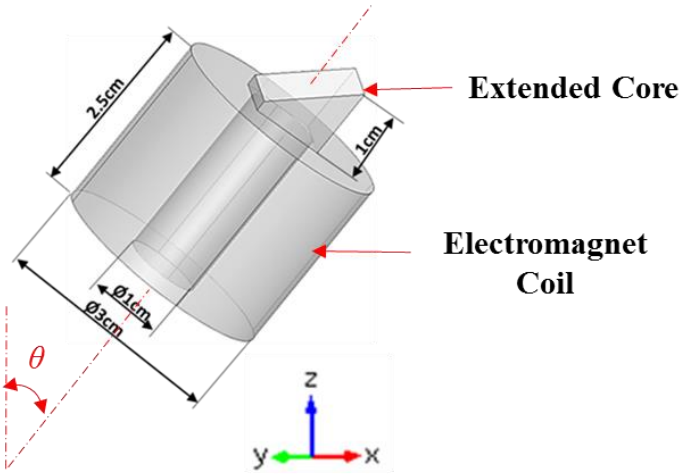

Figure 4. 14: Optimum dimensions of the electromagnet parameters.

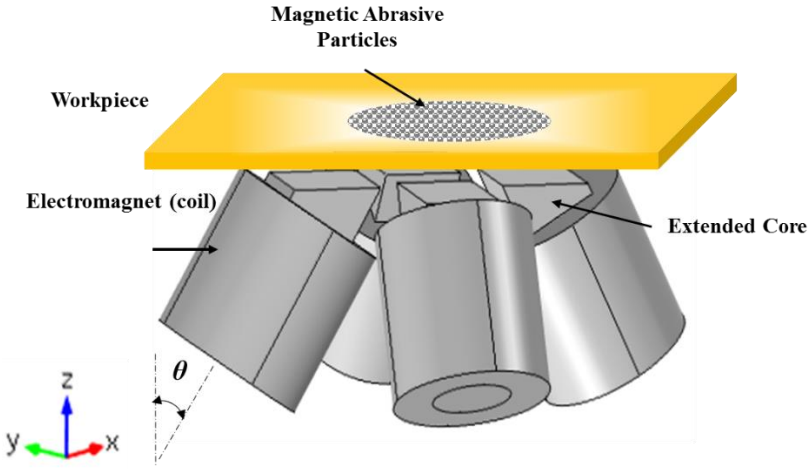

Figure 4. 15: Optimum configuration of the system setup

4.6. Magnetic Force Measurement

The magnetic force between the electromagnetic and a macro-size mixture of iron and abrasive particles, which provides the finishing force, was measured and compared with the numerical values which were obtained from the finite element simulation. Next, a new approach was proposed to determine the

magnetic force applied on just a single particle. Measuring the applied magnetic force on a single particle would require a device with very high accuracy due to the very small size of the particle and the coinciding magnitude of the required force. Therefore, it was proposed to use a simple technique to measure the force approximately using an ATI force sensor. As illustrated in Figure 4.16, the process involved a piece of tape filled with magnetic abrasive particles laid on an aluminum sheet fixed to the holder of the sensor. An electromagnet with an iron core was set underneath the aluminum sheet with a specific air gap (Z). DC current was applied to activate the electromagnet and the magnetic force produced between the iron particles (on the tape) and the electromagnet (with iron core) was measured by the ATI force sensor.

The measured force represented the total force and in order to find the magnet force applied on a single particle, the number of iron particles on the tape was required to be determined. It was assumed that the iron particles have a spherical shape and the average radius of the particle (r_p) was 0.25 mm. Thus, the number of the particles were determined by dividing the total area of the piece of tape, which is (15 mm × 25 mm), by the cross sectional (projected) area of a single particle ($\pi\ r_p^2$). The filled area was assumed to be 75% of the total area in order to compensate for observable unfilled gaps between the particles on the tape.

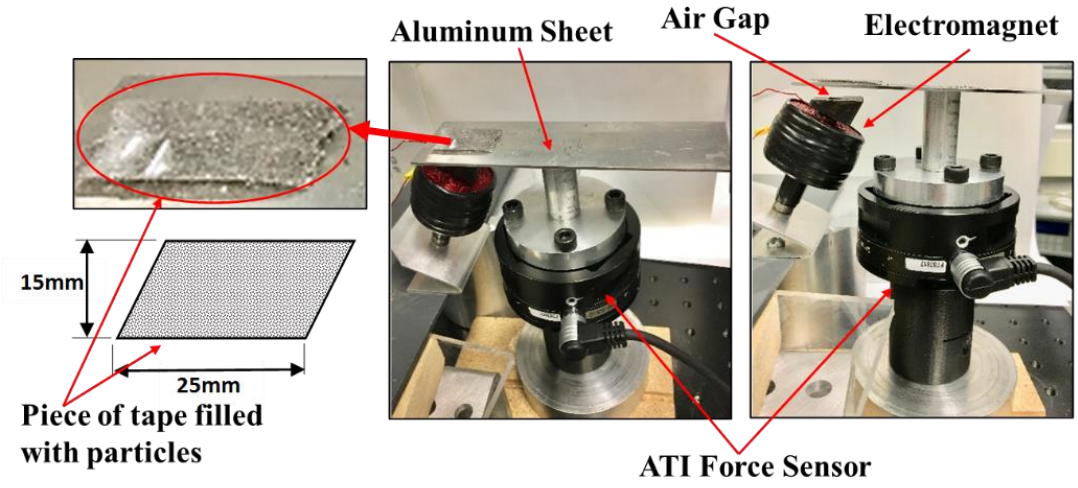

Figure 4. 16: Force measurement experimental setup

Based on that, the number of particles was determined according to the following equation:

$$Particle\ Number = \frac{(15\ mm\ \times\ 25\ mm) \times 0.75}{\pi\ rp2} \cong 1400$$

To verify the accuracy of this approach, three different values of air gap (Z) were considered (3, 5, and 7 mm) with three different values of the applied current (1, 1.5, and 2 A). The results of this approach are as illustrated in Table 4.4.

Table 4.4. Comparison between measured and simulation values of particle force

Air gap (Z) [mm]	Current (I) [Ampere]	Total Measured Force (F_T) [mN]	Particle Force [mN]	
			Simulation	Measured (F_T / Particles Number)
3	2	762.8	0.5253	0.5448
	1.5	438.4	0.3023	0.2743
	1	213.54	0.1420	0.1525
5	2	552.3	0.3915	0.3940
	1.5	325	0.2221	0.2327
	1	140	0.1004	0.1000
7	2	542.2	0.3705	0.3879
	1.5	300	0.2133	0.2142
	1	143.2	0.1002	0.0892

Figure 4.17 shows a comparison of the experimental results of the force measurement with the FEM results. Generally, it can be said that there is a good agreement between the obtained results with an average error percentage of approximately 3.5%.

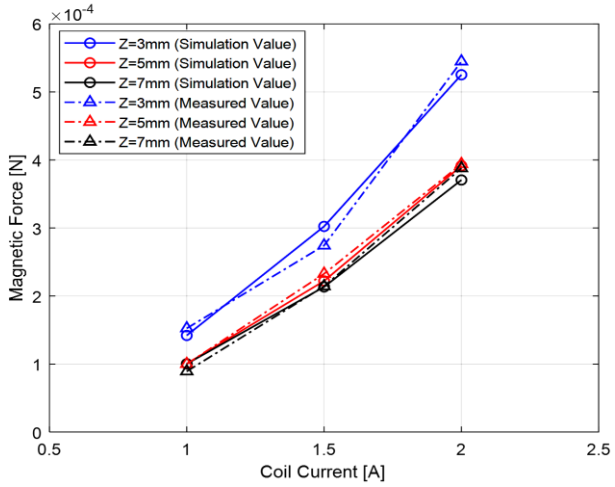

Figure 4. 17: A comparison of magnetic force versus excitation current for different axial air gaps based on experimental force measurement and FEM results

4.7. Experimental Results

The electromagnets were fabricated based on the optimum design parameters as shown in Figure 4.14. Outer and inner diameter of the coil were 3 cm and 1cm, respectively, while the length of the coil was 2.5 cm and the length of the iron core with the extended chamfered tip was 1 cm with a chamfer angle of 30°. The number of turns of the coil was 1,050 turns and the wire gauge was 24 (AWG). The experimental setup used for the current study was as illustrated in Figure 4.18. It was developed for a planar finishing process using a rotating magnetic field.

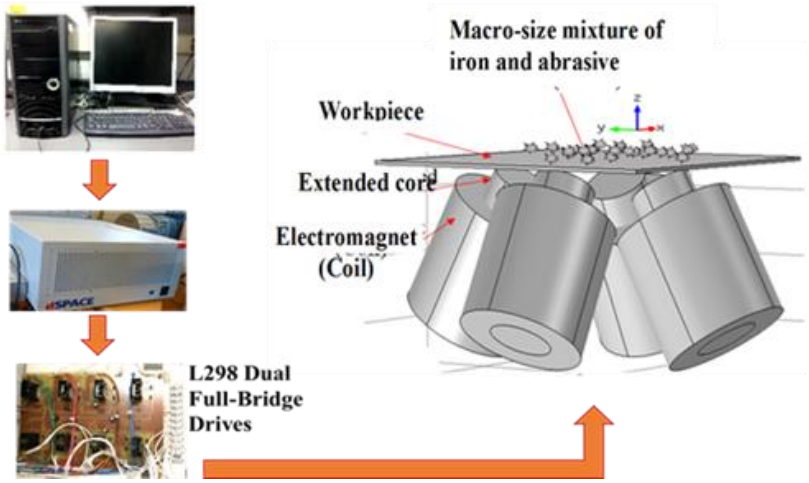

Figure 4. 18: Schematic of the SMAF proposed system

A CP Grade 2 Titanium sample was used as the workpiece, as recently, titanium and its alloys are commonly used in bone implants and some biomedical applications due to its excellent mechanical properties and biocompatibility [67]. The experimental conditions are as illustrated in Table 4.5.

Table 4.5: Experimental conditions

Workpiece	CP Grade 2 Titanium
Abrasive Particles	Al_2O_3, 75 [µm] in mean diameter.
Iron Particles	Fe particles 0.3 [mm] in mean diameter.
Coil activation frequency	2 Hz
Applied voltage	30 V [current passing through the coils ≅1.5 A]
Air Gap	2 mm
Finishing time	60 min

Figure 4.19 shows 3D photographs of the finished surfaces before (a) and after (b) the finishing process. The experimental results showed that under these finishing parameters, the average surface roughness (Ra) was improved from 4.156 µm to 1.94 µm, and the height of the highest peak (Sp) was improved from 21.144 µm to 14.409 µm.

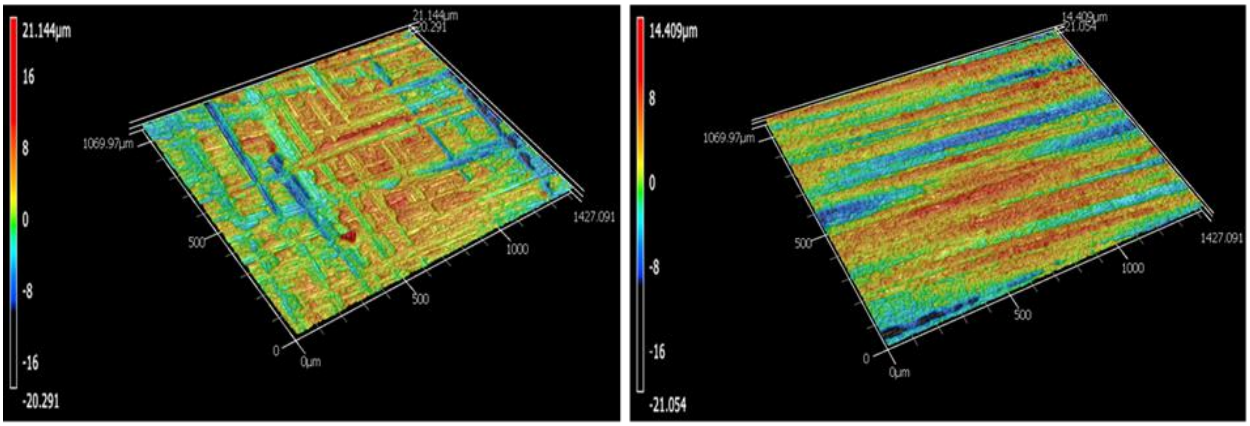

(a) (b)

Figure 4. 19: 3D photographs of polished surfaces (a) before and (b) after the finishing process

4.8. Temperature Variation

As a result of the magnetic abrasive particles movement on the workpiece surface under the finishing pressure, heat flux was generated due to friction in the interfering zone. This heat generation caused a temperature rise which could significantly affect the quality of the finished surface. Temperature variation in the interfering area in some finishing processes can reach up to 980˚C, which can adversely generate thermal and residual stresses in the surface and subsurface of the workpiece [53].

One of the most important advantages of the MAF process is the insignificant effect of the temperature variation, due to the limited raising of the workpiece temperature during the finishing process. In some applications of MAF the range of temperature variation is around 31-42˚C [54]. In this work, the temperature of the interfering zone between the surface of the titanium workpiece and the magnetic abrasive particles was measured using a thermal camera. As illustrated in Figure 4.20, before starting the finishing process (@ Time = 0), the temperature of the titanium specimen was 23˚C. After running the system for 30 minutes (@ Time = 30 mins) the temperature of the titanium specimen raised up to 29.1˚C and within 60 minutes the temperature reached 37.0˚C. This infers temperature variation during the operation time (60

minutes) was 14.0˚C (23.0 – 37.0˚C). During this process, the maximum surface roughness was improved from 262 µm to 177.6 µm. This temperature variation was still under the accepted limit, and represents an insignificant impact on the sample surface characteristics and quality.

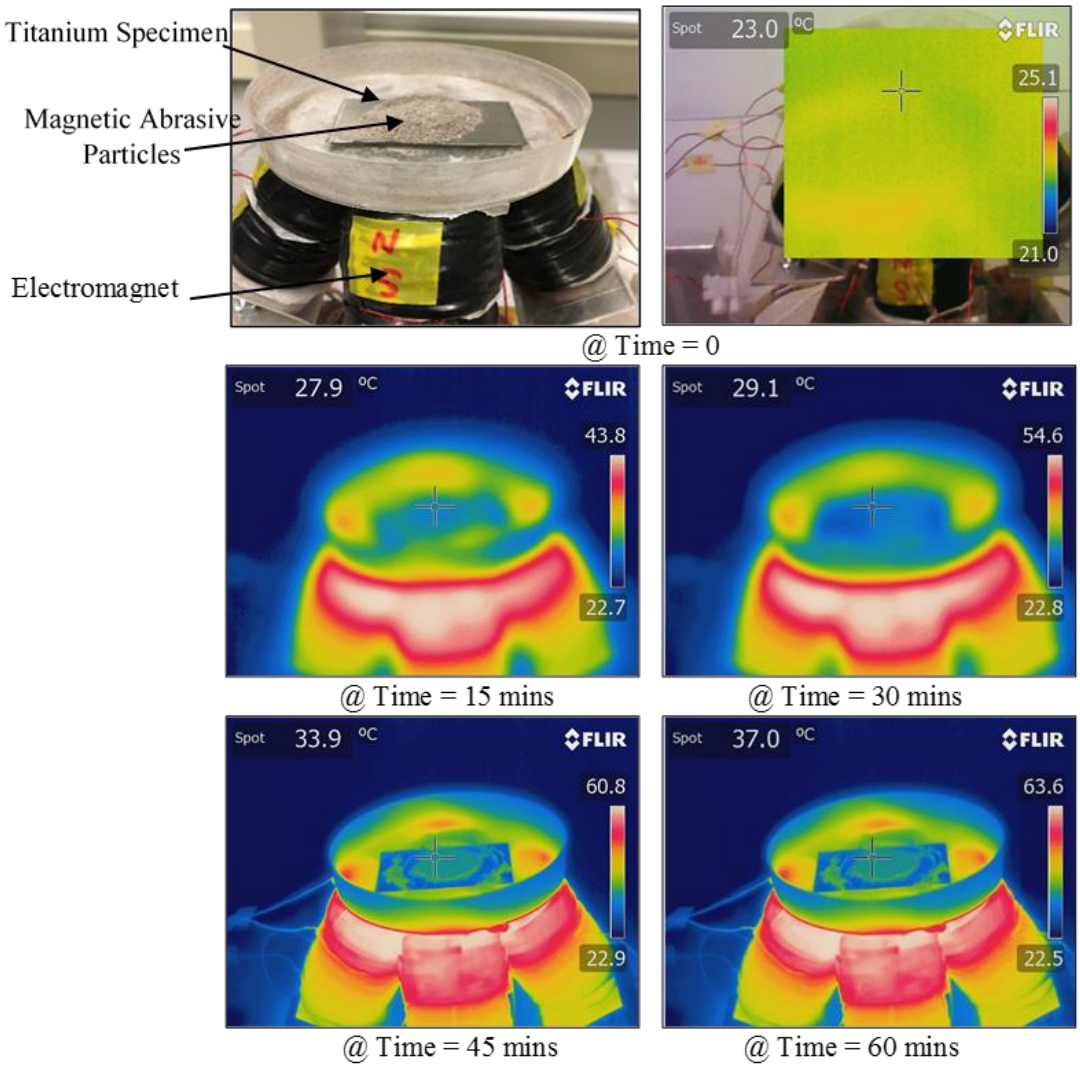

Figure 4. 20: Thermal images of Titanium CP Grade 2 sample at different times during the finishing process.

4.9. Conclusions

In the current study, electromagnet optimal configuration was investigated in order to maximize the finishing force in the working area. The optimization approach used for the electromagnets coil was carried out in two stages. In the first stage, the integrated formula of a thin shell solenoid was used to obtain the gradient of the magnetic field at any point on the axis of a finite solenoid. In the second stage, a parametric study was carried out to optimize the geometry of the electromagnet using a finite element simulation. The electromagnet volume was fixed as *50* cm^3 and the optimum coil parameters were found to be (α=3 and β=2.5), and the Fabry factor (Geometry factor) was G = 0.175. Coil length was l = 2.5 cm and the iron core length l_c was 3.5 cm, with outer and inner diameters of 1.5 cm and 0.5 cm, respectively.

Moreover, a new approach was conducted to measure the magnetic force experimentally using an ATI force sensor. The results were verified using a finite element simulation with percentage error of 3.5%. The MAF process setup of the optimal electromagnet configuration was applied to finish a titanium (CP Grade 2) specimen with finishing conditions of 28 V, applied voltage, 2 Hz electromagnet activation frequency, and 60 mins as the operation time. The abrasive particle was aluminum oxide with 75 µm particle size mixed with 0.5 mm average diameter iron particles. The average surface roughness (Ra) was improved from 4.156 µm to 1.94 µm, and the height of the highest peak (Sp) was improved from 21.144 µm to 14.409 µm. Also, the variation of temperature in the interfering zone between the Titanium specimen and the magnetic abrasive particles was measured using a thermal camera. The measurement showed that the variation during the operation running time (60 mins) was just 14˚C, the temperature change was (23 – 37˚C). This change would have an insignificant effect on the surface characteristics and quality.

Chapter 5

System Modeling

5.1. Introduction

This chapter describes the main components of the Stationary Apparatus of Magnetic Abrasive Finishing (SMAF) and the essential function of each component. In addition, it explains the fundamental models used to represent the relationship between the main parameters of the Magnetic Abrasive Finishing (MAF) process. Furthermore, it describes the modeling and analyzing of the magnetic field in the working area, the cutting forces, and the metal removal mechanism.

5.2. System Description

The system used for this study contains software and many hardware components as illustrated in Figure 5.1. The software component represents a MATLAB-Simulink file. Its primary purpose is to simulate the system based on a mathematical model that governs the main parameters used in this application.

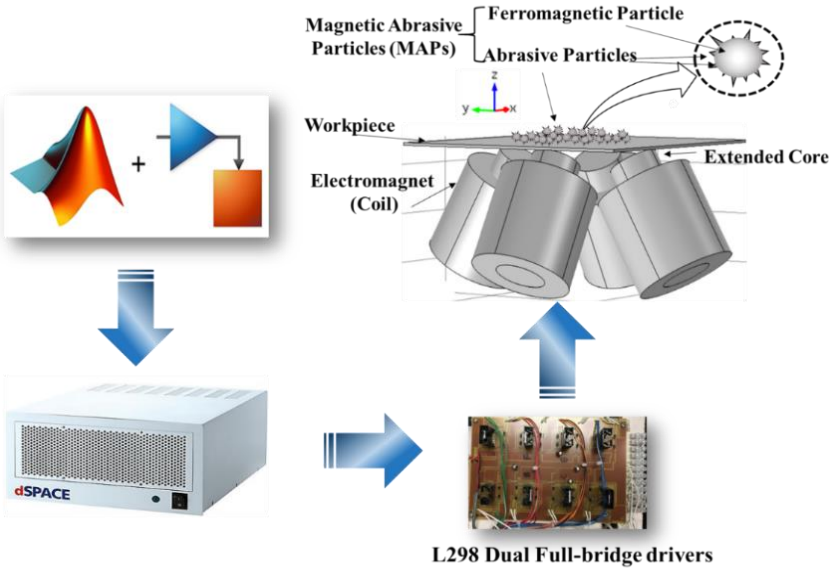

Figure 5. 1: System Description.

The hardware components contain a dSPACE machine which serves as a data acquisition device. The data source comes from the Simulink file. Secondly, there is an amplifier and a power supply which feeds the dSPACE machine and L298 Dual Full-Bridge Driver. The L298 Dual Full-Bridge Driver basically can control the direction of the current, which then controls the polarity of the electromagnet (coils): as either North (N) or South (S) Pole according to the signal pattern illustrated in in Figure 5.2.

The third part of the hardware components, the physical system, contains four-cylindrical electromagnets. Each electromagnet contains a coil with (1000) turns of a copper wire (AWG 22) around an iron core. The diameter of the coil is 40mm and the height is also 40mm. The iron core diameter is 20mm and the height is 50mm. The electromagnetic coils are inclined with respect to the vertical axis with an angle of 30˚. This arrangement is shown in Figure 5.2.

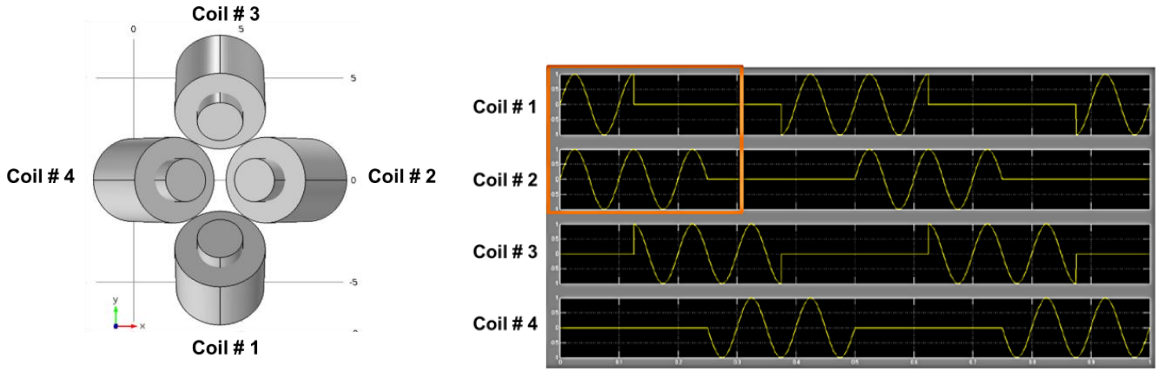

Figure 5. 2 : The electromagnetic coils alignment and signal pattern.

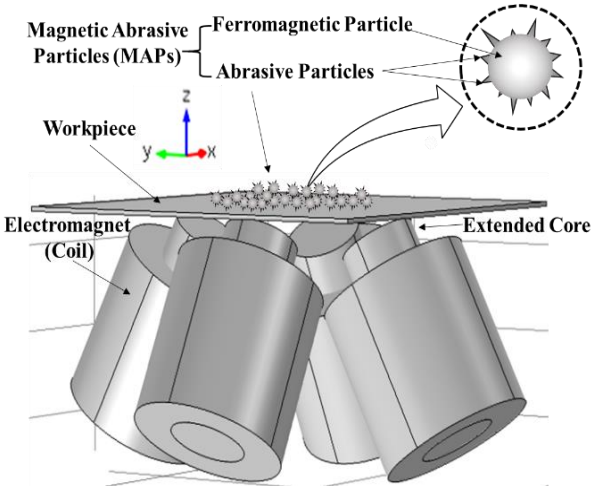

Figure 5. 3: The physical system setup

The workpiece is placed above the electromagnetic coils, as shown in Figure 5.3 and, above the surface of the workpiece, the Magnetic Abrasive Particles (MAPs) are placed in order to perform the finishing process.

5.3. Finite Element Model

There are many reasons why modeling of the MAF process is so difficult including the nonuniform geometry of the magnetic field domain and the working gap, and the nonlinear properties of the magnetic abrasive particles (magnetic particles and abrasive particles). Therefore, some researchers prefer to use the Finite Elements Method instead of the analytical methods to find the parameters solution [61].

The modeling starts with classical Maxwell's equations (5.1- 5.3) as the governing equations of the model.

$$\nabla \times E = \frac{\partial B}{\partial t} \tag{5.1}$$

$$\nabla \times H = J + \frac{\partial D}{\partial t} \tag{5.2}$$

$$\nabla \cdot B = 0 \tag{5.3}$$

where:

E: Electric field vector, *B:* Magnetic flux density vector, *H:* Magnetic flux intensity vector,

J: Electric current density, *D:* Electric flux density vector, and *t:* Time.

Since there is no current through the working gap, it can be considered that $\frac{\partial D}{\partial t} = 0$ and $J = 0$; the process is also assumed to be steady. Therefore, Maxwell's equations (5.1- 5.3) will be [14]:

$$\nabla \times E = 0 \tag{5.4}$$

$$\nabla \times H = 0 \tag{5.5}$$

$$\nabla \cdot B = 0 \tag{5.3}$$

The relationship between *B* and *H* in a vacuum is:

$$B = \mu_o H \tag{5.6}$$

where $\mu_o = 4\pi \times 10^{-7}$ (T·m/A) the permeability of free space.

The working gap is filled with the magnetic abrasive particles MAPs (magnetic particles and abrasive particles), so the magnetic flux density is as in equation (5.6):

$$B = \mu_o(H + M) \tag{5.7}$$

where *M* is the internal magnetization of the ferromagnetic.

And the magnetic field intensity can be expressed as a gradient of magnetic scalar potential ϕ [8]:

$$H = -\nabla\phi \tag{5.8}$$

Since magnetization is:

$$M = \chi H \tag{5.9}$$

So equation (5.7) can be expressed as:

$$B = \mu_o(1 + \chi)H \tag{5.10}$$

Substituting the values of *B* and *H* from equation (5.9) and (5.10) in equation (5.3):

$$\nabla \cdot [\mu_o(1 + \chi)(-\nabla\phi)] = 0 \tag{5.11}$$

But μ_o is constant and $(1 + \chi) = \mu_r$

where μ_r is the relative permeability of MAPs, so (5.11) becomes:

$$\nabla \cdot [\mu_r \nabla\phi] = 0 \tag{5.12}$$

In the cylindrical coordinate system, equation (5.13) is expressed as [61]:

$$\frac{1}{r}\frac{\partial}{\partial r}\left[r\mu_r \frac{\partial\phi}{\partial r}\right] + \frac{1}{r^2}\frac{\partial}{\partial\theta}\left[\mu_r \frac{\partial\phi}{\partial\theta}\right] + \frac{\partial}{\partial z}\left[\mu_r \frac{\partial\phi}{\partial z}\right] = 0 \tag{5.13}$$

Therefore, the components of the magnetic flux intensity *Hr* and *Hz* can be evaluated from [14]:

$$Hr = -\frac{\partial\phi}{\partial r} \tag{5.14}$$

$$Hz = -\frac{\partial\phi}{\partial z} \tag{5.15}$$

The magnetic force F_m can be expressed as the gradient of the magnetic potential energy [62]:

$$F_m = \frac{\mu_o}{2}\nabla\int_v M \cdot H dV \tag{5.16}$$

And due to the small volume of the particle, *V*, the magnetization M, and field intensity H can be considered uniform. So equation (5.16) can be simplified to:

$$F_m = \mu_o V(M \cdot \nabla)H \tag{5.17}$$

Magnetic susceptibility χ should represent the magnetic susceptibility of the ferromagnetic particles and abrasive particles, and it can be obtained by applying Wiedemann's [61], [63]:

$$\chi = \alpha\chi_{ferr} + (1-\alpha)\chi_{abr} \tag{5.18}$$

where, α is the volume fraction of ferromagnetic, and χ_{ferr} and χ_{abr} are the susceptibility of ferromagnetic and abrasive particles, respectively. Also for the relative permeability of magnetic abrasive particles, μ_r, can be obtained from [61], [63]:

$$\mu_r = \alpha\mu_{rferr} + (1-\alpha)\mu_{rabr} \tag{4.19}$$

where, μ_{rferr} and μ_{rabr} are the relative permeability of ferromagnetic and abrasive particles, respectively.

5.4. Magnetic Field Analysis

To analyze the magnetic field, many approaches have been applied, starting with Biot-Savart for on-axis of a single current loop and then for a multi-turn air core solenoid. Next, for off-axis of a single current loop and not only for a multi-turn coil, but also for a multi-layer one, further using superposition. These approaches are presented in Appendix B. It can be noticed that the relationships of determining the magnetic field are considered valid if the core of the solenoid is air, not iron. Thus, in order to make these relationships valid to use for the iron-core solenoid, and, as it is being used in the SMAF system setup, therefore numerical predictions must be developed to determine scaling factors that can be used confidently to quantify the magnetic field for the iron-core solenoid. This concept can be obtained by comparing the magnetic field magnitude of the air-core and iron-core solenoid analytically and experimentally.

Numerically, finite elements analysis was used to determine the magnetic field components within the stated range in relation to the position of the coil, as shown in Figures (5.4 and 5.5).

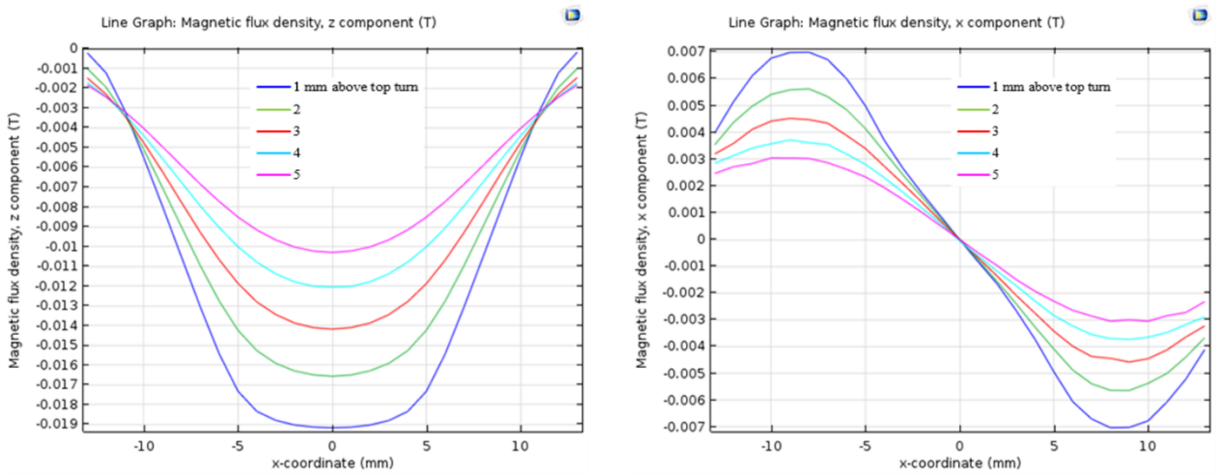

Figure 5. 4: Magnetic field components Bz and Bx of different distance above the electromagnet coil (from 1mm-5mm), air-core.

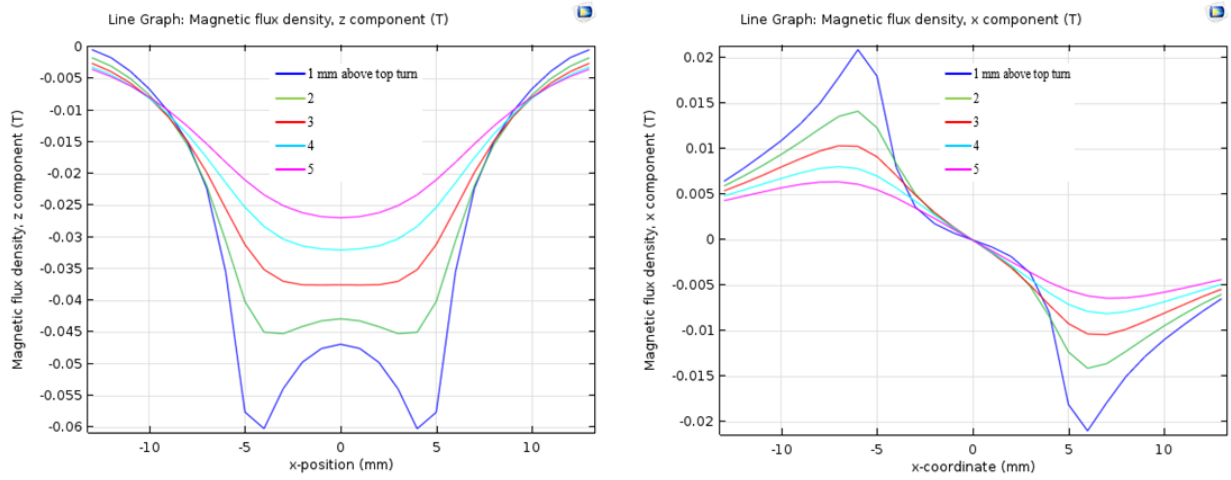

Figure 5. 5: Magnetic field components Bz and Bx for different distance above the electromagnet coil (from 1mm-5mm), iron-core.

Experimentally, the apparatus involved the electromagnet coil construct, with/without iron core, with the equipment shown in Figure 5.6 used to measure the magnetic field components *Bz* and *Bx* within the same range in relation to the position of the electromagnet coil, as was done analytically. Measurements of the *B* components were taken at 1 mm spacing in the x and z directions (x-z plane), at the elevations above the top turn of the coil construct with the results as shown in the following plots in relation to the central axis of the coil. The probe was oriented to obtain measurements in one direction first, then rotated ninety degrees to obtain the other. Figure 5.7 shows the electromagnet with/without iron core, and, assembled.

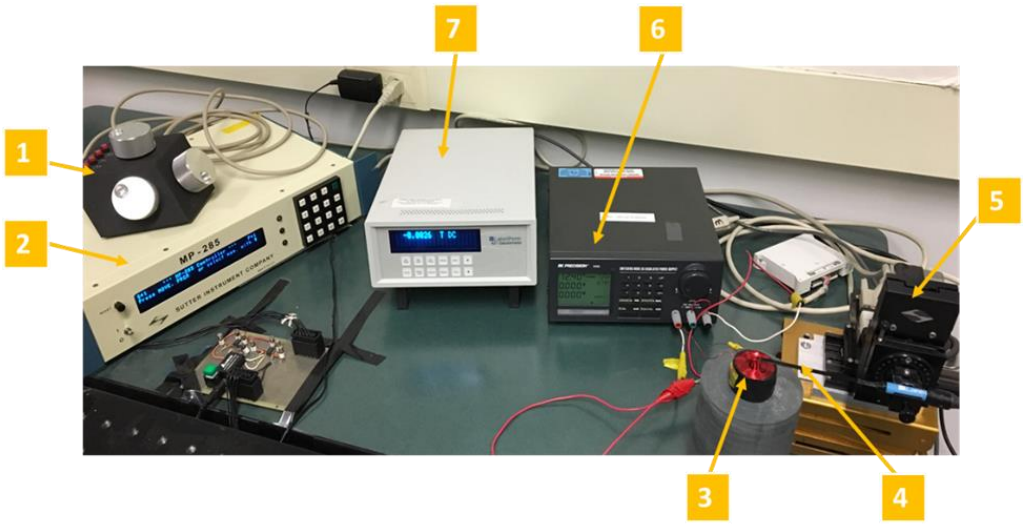

Figure 5. 6: Photograph of the setup used to measure B, 1) 3-D position motor of micromanipulator. 2) MP-285 controller. 3) Electromagnet (air core shown). 4) Gauss meter probe. 5) Motorized micromanipulator. 6) Power supply. 7) Gauss meter.

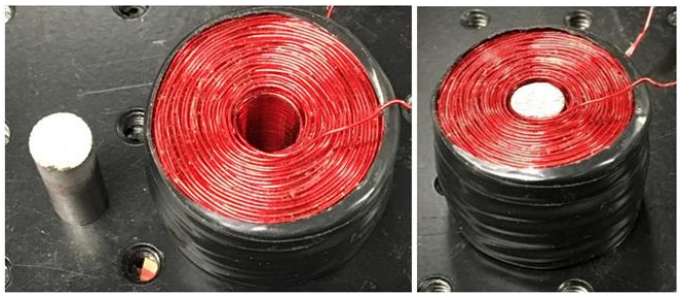

Figure 5. 7: Electromagnet with/without iron core, and assembled

Figures (5.8 and 5.9) show the plotted relations for *Bx* and *Bz*, respectively, with air core, iron core, their ratio, and the average ratio plotted for each.

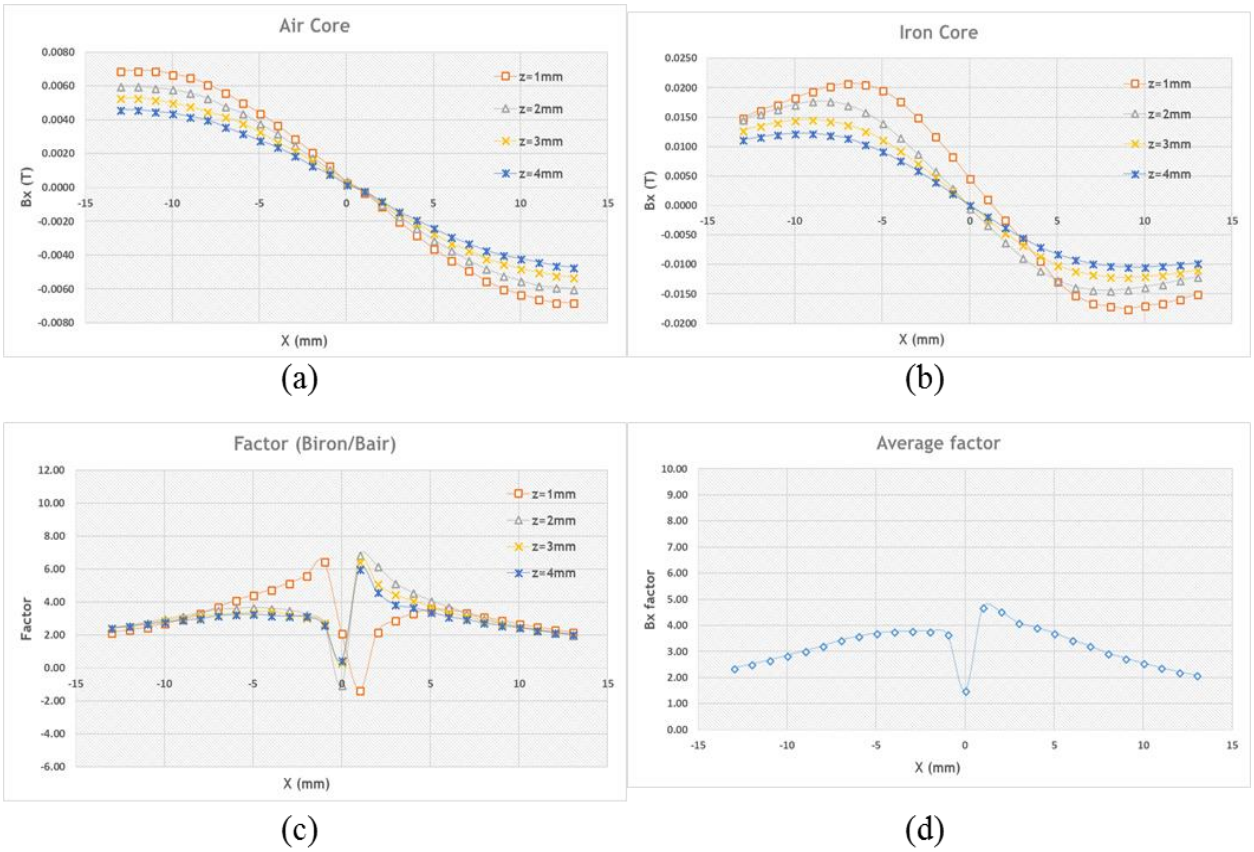

Figure 5. 8 : Bx component for electromagnet with/without iron core, (a) air-core, (b) iron-core, (c) factor (B iron/B air), (d) average factor curve.

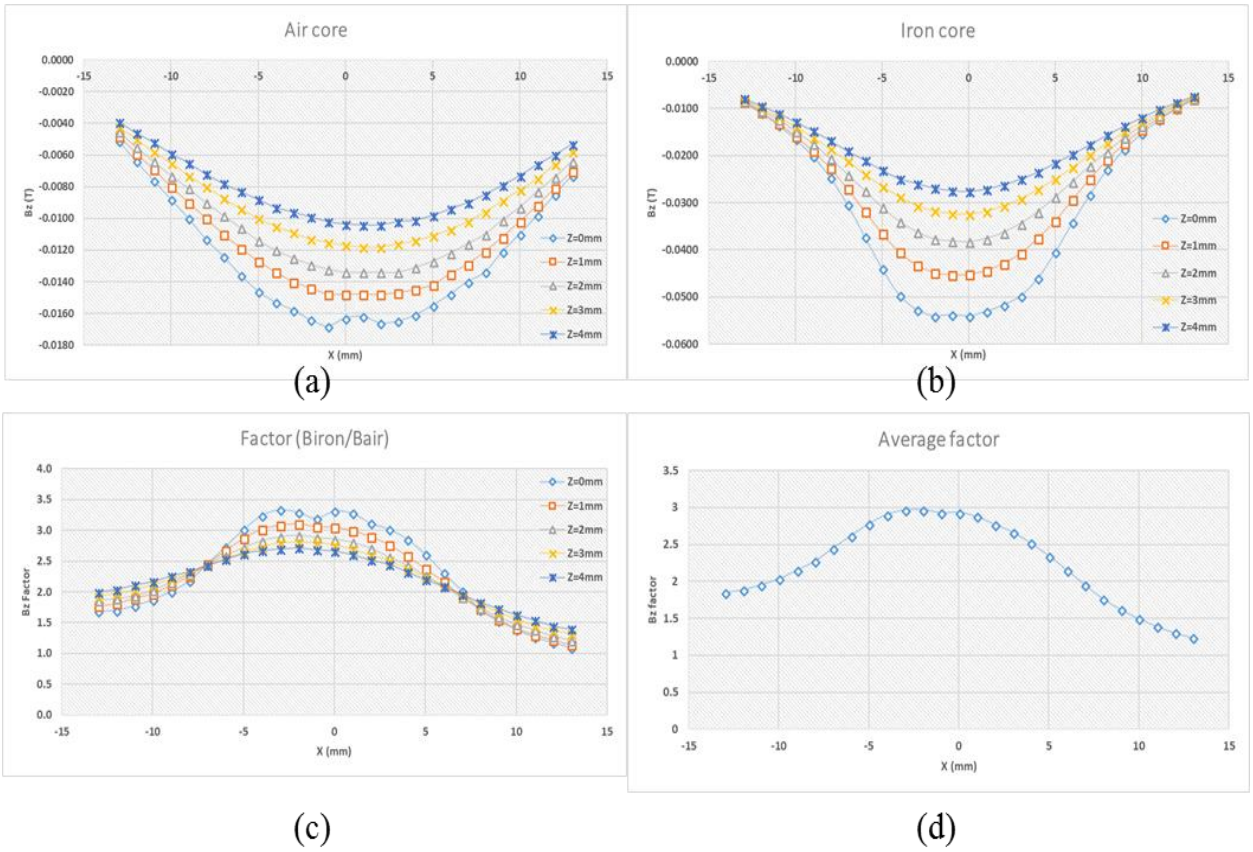

Figure 5. 9: Bz component for electromagnet with/without iron core, (a) air-core, (b) iron-core, (c) factor (B iron/B air), (d) average factor curve.

The above plots and their data were used to determine the equations and variable relations to predict *B* at any point in space above a coil construct with an iron-core. Both the *normB* and the components of *B* were considered for the following. The *normB* used completely raw data as the norm has an inherent ability to accommodate fluctuations, whereas the components used adjusted data from the average factor curves of Figures (5.8 and 5.9). For the *Bx* component, the left half of the curve was mirrored right, and for the z component the two sides were averaged and equated. The norm curve fit used a fifth order polynomial function, whereas the component curves both used a sum of sines function with the 95% confidence interval coefficients as listed in Table 5.1. Also provided are the curve "adjusted R-square" values.

Table 5.1: Fit functions and maximum error.

Fitting Function	Equation	Coefficients
Polynomial (norm)	$Bnorm(x) = ax^4 + bx^3 + cx^2 + dx + e$	$a = 2.632e-05$ $b = 0.0001592$ $c = -0.009772$ $d = -0.04549$ $e = 2.836$ $R^2 = 0.9973$
Sum of Sines (z component)	$B_z(x) = \sum_{i=1}^{2} a_{iz}\sin(b_{iz}x + c_{iz})$	$a_{1_z} = 2.216$ $b_{1_z} = 0.004761$ $c_{1_z} = 1.571$ $a_{2_z} = -0.6371$ $b_{2_z} = 0.2279$ $c_{2_z} = -1.571$ $R^2 = 0.9992$
Sum of Sines (x component)	$B_x(x) = \sum_{i=1}^{2} a_{ix}\sin(b_{ix}x + c_{ix})$	$a_{1_x} = 3.825$ $b_{1_x} = 0.06956$ $c_{1_x} = 1.571$ $a_{2_x} = 0.1074$ $b_{2_x} = 0.6091$ $c_{2_x} = -1.571$ $R^2 = 0.9959$
Maximum error (T)		*Norm*= 0.0045 *Z*= 0.0056 *X*= 0.0040

The equations of fit average factor curves were then used to predict the components of the magnetic field for an iron core electromagnet with the predictions then compared to the experimentally obtained results. The goodness of fit error is plotted as a surface for the *normB* as well as the *Bx* and *Bz* components in

Figures (5.10 and 5.11) for four elevations with the maximum error as shown in red in the figures and at the base of Table 5.1.

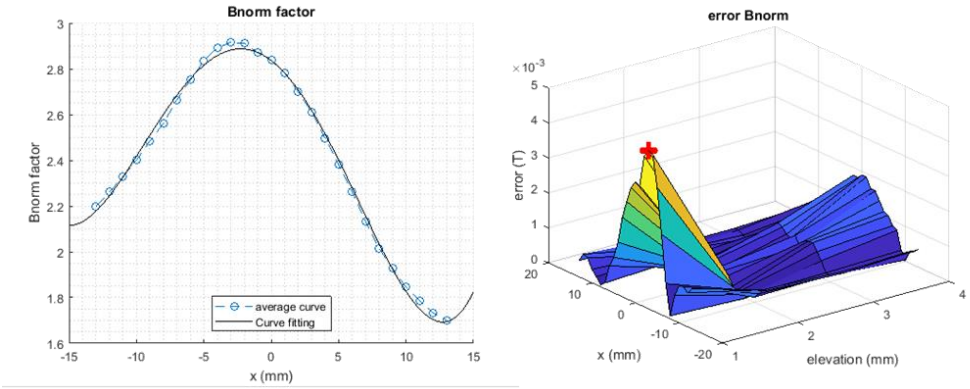

(a) (b)

Figure 5. 10: (a) normB average factor and curve fit, (b) normB error.

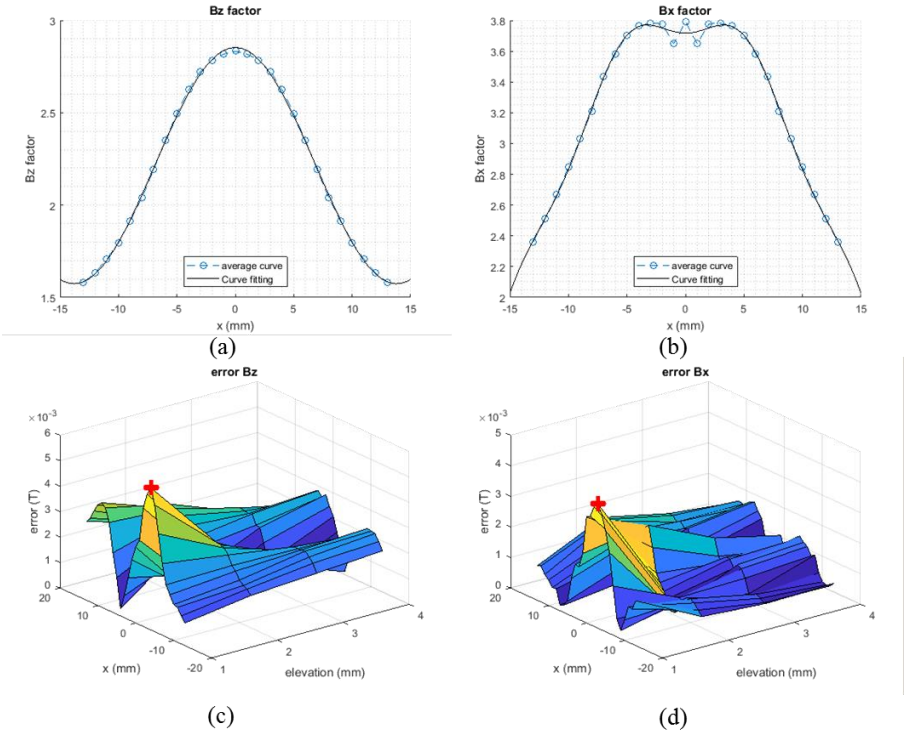

(a) (b)

(c) (d)

Figure 5. 11: (a) Bz average factor and curve fit, (b) Bx average factor and curve fit, (c) error of Bz, (d) error of Bx.

5.5. Electromagnets configuration setup

Various configuration setups were used in order to obtain the optimum movement for the Magnetic Abrasive Particles (MAPs) on the workpiece surface. The aim was to determine how the particles can be moved in a circular or semicircular path on the surface of the workpiece under the effect of the rotating magnetic field to accomplish the process of metal removing and produce a new surface. Therefore, the configurations of three-coils, four-coils, and six-coils were used, as shown in Figure 5.12 (a-d). The configuration of four-angled coils, Figure 5.12 (c), was chosen as the best configuration.

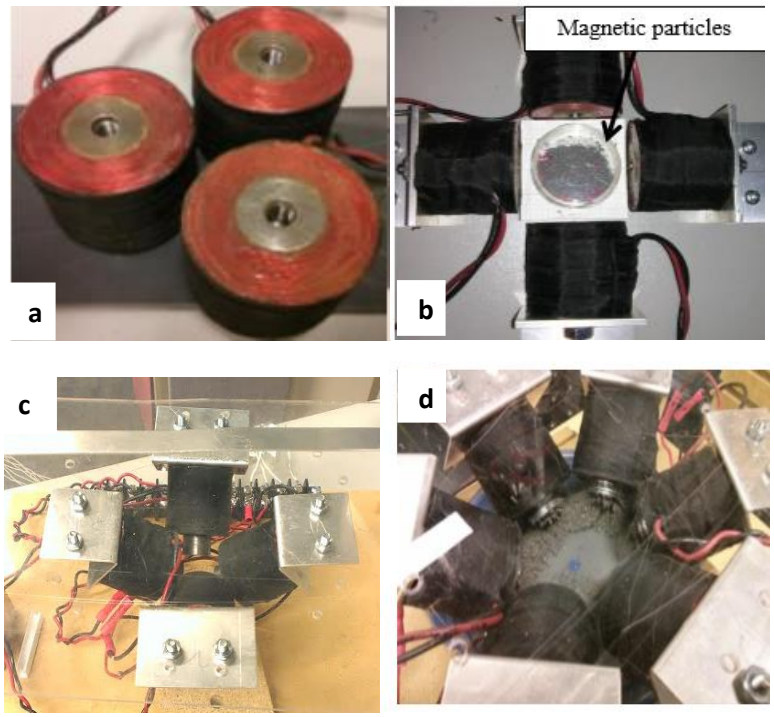

Figure 5. 12: a) 3-coils in triangular setup, b) 4-coils horizontal configuration, c) 4- angled coils configuration, and d) 6-coils configuration.

Studying the variation of magnetic flux density in the working gap between the electromagnet and the workpiece was very important because it significantly affects the magnetic force which controls the quality of the finished surface. So, the variation of magnetic field was studied as follows:

5.5.1. Magnetization effect on the magnetic field

The fundamental relationship between magnetic flux density ***B*** and Magnetic flux intensity ***H*** in the vacuum is according to equation (5.6):

$$B = \mu_o H$$

But the value of ***B*** changes when the ferromagnetic particles are placed in the air gap between the electromagnet and the work-piece, because of the internal magnetization ***M***. The magnitude of B is according to equations (5.7) and (5.9):

$$B = \mu_o (H + M)$$

$$M = \chi H$$

where χ is the magnetic susceptibility of the particle material.

This effect can be clearly noticed by using COMSOL Multiphysics® version 5 simulation software to simulate an electromagnet with an iron particle. Figures (5.13 and 5.14) show how the magnetic field lines can be affected when they pass through the iron particle and the increment of B values.

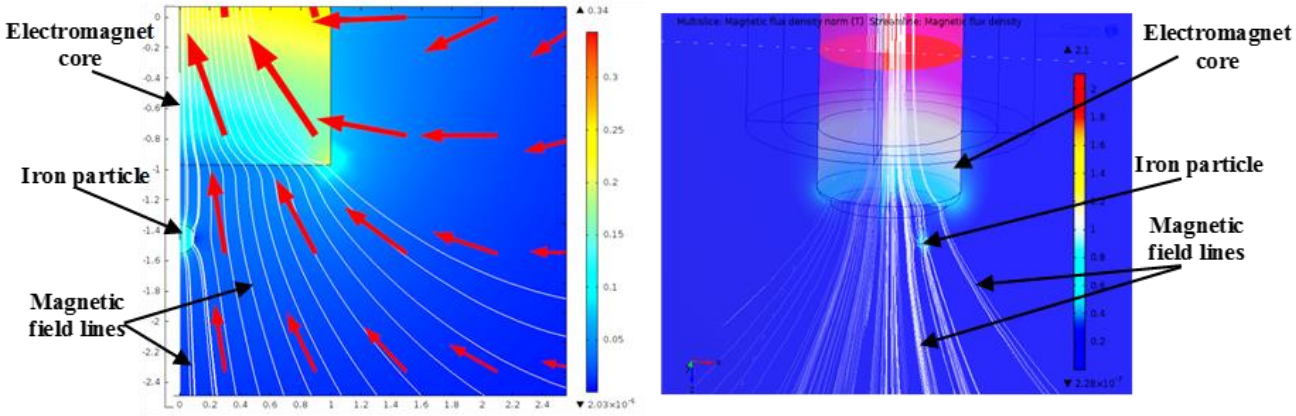

Figure 5. 13: Variation of the magnetic field lines when they pass through the iron particle.

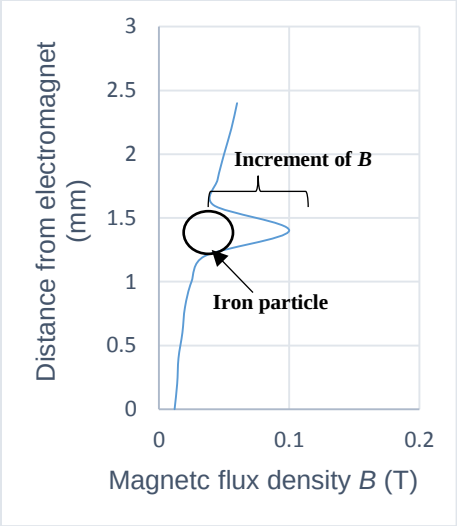

Figure 5. 14: The increment of the magnetic flux density B within the iron particle.

5.5.2. Best configuration of the electromagnets to maximize B_{xy} component

The variation of magnetic flux density, B, in the working area was studied and analyzed for different configurations of electromagnets to identify the best configuration. The best configuration means the one that can make the component of B in a tangential direction, $B_{xy,}$ greater than the component of B in a normal direction, B_z. Thus, the tangential force component, F_{mt}, will be greater than the normal force component, F_{mz}.

This is important to make the particles on the workpiece surface move tangential according to the rotation of the magnetic field to accomplish the finishing process. As shown in Figure 5.15, the electromagnets are aligned along the X axis. It can be readily noticed that the B_z component is greater than B_x and B_y, and as a result, it is greater than the B_{xy} component.

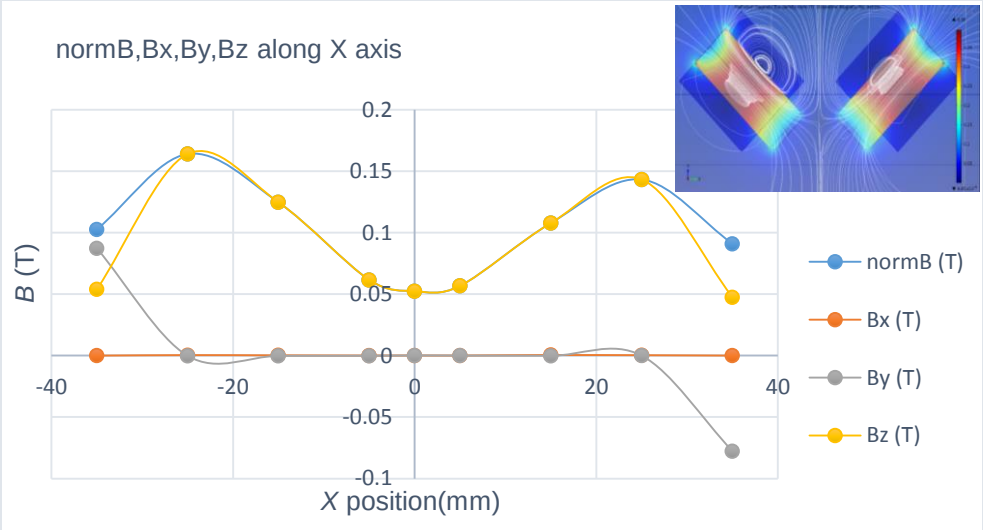

Figure 5. 15: Variation of B values with respect to the position along X axis for the two electromagnets aligned along X axis.

When the electromagnets are aligned along the perpendicular axes, one on the *X* axis and the other on the *Y* axis, as shown in Figure 5.16, the B_{xy} component will be greater than B_z especially when the particles move along the trajectory (according to the red dashed line).

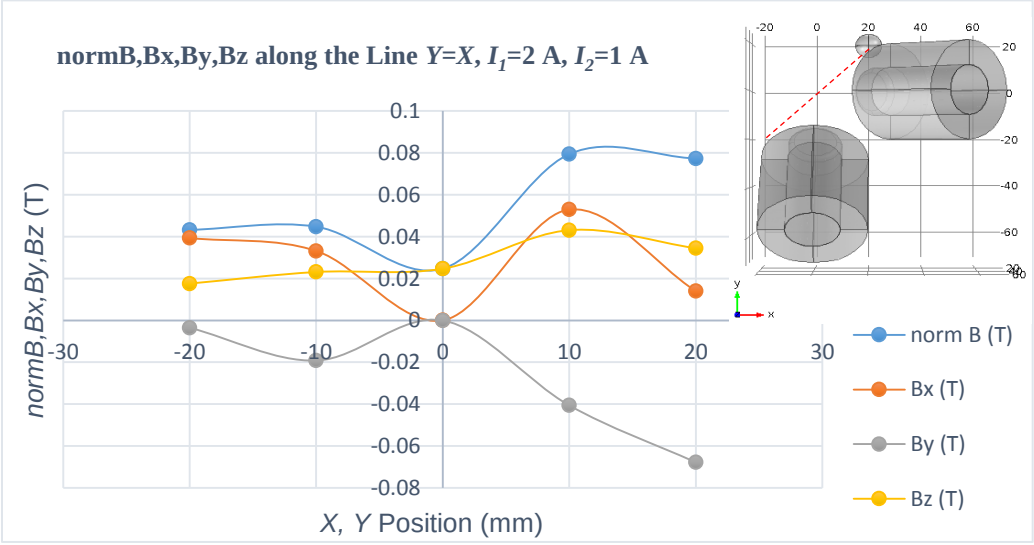

Figure 5. 16: Variation of B values with respect to the position along the red dashed line for the two electromagnets aligned on X and Y axes.

5.6. Analysis of cutting forces and metal removal

The metal removal mechanism in magnetic abrasive finishing can be considered to be a Micro-cutting or a Nano-cutting process due to the minute chips formed [43]. The applied magnetic field in the working gap with the presence of MAPs produced a Flexible Magnetic Abrasive Brush (FMAB) as shown in Figure 5.17. The FMAB acts just like a multi cutting edge tool, or the grinding wheel in a grinding process.

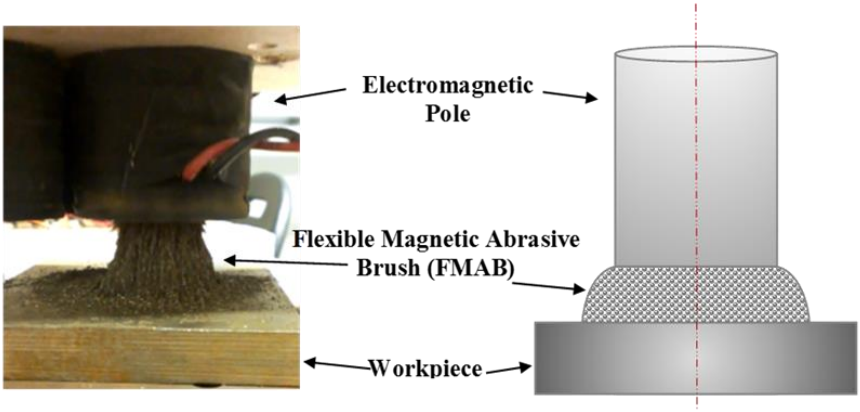

Figure 5. 17: The Flexible Magnetic Abrasive Brush (FMAB).

The movement of the FMAB on the workpiece surface produces grooves, and the volume of these grooves is equal to the volume of the removed material or the formed chips [14].

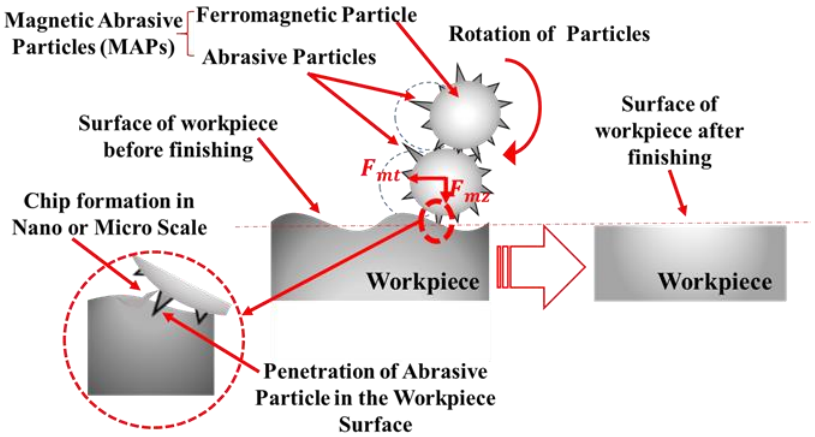

Figure 5. 18: Schematic of (MAF) with details of forces on a single Abrasive Particle.

The magnetic field generated by the angled electromagnet produces two components of magnetic force: the tangential component (F_{mt}), which is parallel to the working surface; and the normal component (F_{mz}), which is perpendicular to the working surface, as shown in Figure 5.18. The normal component, (F_{mz}), forces the cutting edges of MAPs to penetrate the workpiece surface, whereas the tangential component (F_{mt}) acts as a shearing force on the surface of the workpiece and forms the Micro-chips due to the motion trajectory of the MAPs. Therefore, a new surface will be produced due to the metal layer being removed from the workpiece surface as shown in Figure 5.18.

5.6.1. Modeling of the normal component (F_{mz})

The magnetic force F_m according to equation (5.17) is:

$$F_m = \mu o\ v(M.\nabla)H$$

And the extension of equation (5.17) is:

$$F_m = \mu o\ v[\left(Mx\frac{\partial Hx}{\partial x} + My\frac{\partial Hx}{\partial y} + Mz\frac{\partial Hx}{\partial z}\right),$$

$$\left(Mx\frac{\partial Hy}{\partial x} + My\frac{\partial Hy}{\partial y} + Mz\frac{\partial Hy}{\partial z}\right),$$

$$\left(Mx\frac{\partial Hz}{\partial x} + My\frac{\partial Hz}{\partial y} + Mz\frac{\partial Hz}{\partial z}\right)] \quad (5.20)$$

So the normal component of the magnetic force is:

$$F_{mz} = \mu o\ v\left[\left(Mx\frac{\partial Hz}{\partial x} + My\frac{\partial Hz}{\partial y} + Mz\frac{\partial Hz}{\partial z}\right)\right] \quad (5.21)$$

This component acts in a vertical direction (Z direction), and it is responsible for penetrating the abrasive particles into the workpiece surface.

The polishing pressure $\boldsymbol{P}$ can be evaluated from [64]:

$$P = \frac{B^2}{2\mu_o}\left(1 - \frac{1}{\mu_r}\right) \quad (5.22)$$

And $\boldsymbol{B}$, which represents the magnetic flux density in the working area, can be calculated as:

$$B = \frac{\mu_o NI}{g} \tag{5.23}$$

where μ_o is the magnetic permeability of vacuum ($4\pi \times 10^{-7}$), N is the number of turns in the electromagnet coil, I, is the magnetizing current, and g is the working air gap. So, for N =1000 turns, I =1.4 A, g =3mm, B= 0.586 T, and P= 0.136 MP_a.

Also the normal component of the magnetic force can be considered as [64]:

$$F_{mz} = PA \tag{5.24}$$

where ***A*** is the contact area of the flexible magnetic abrasive brush (FMAB) with the workpiece surface.

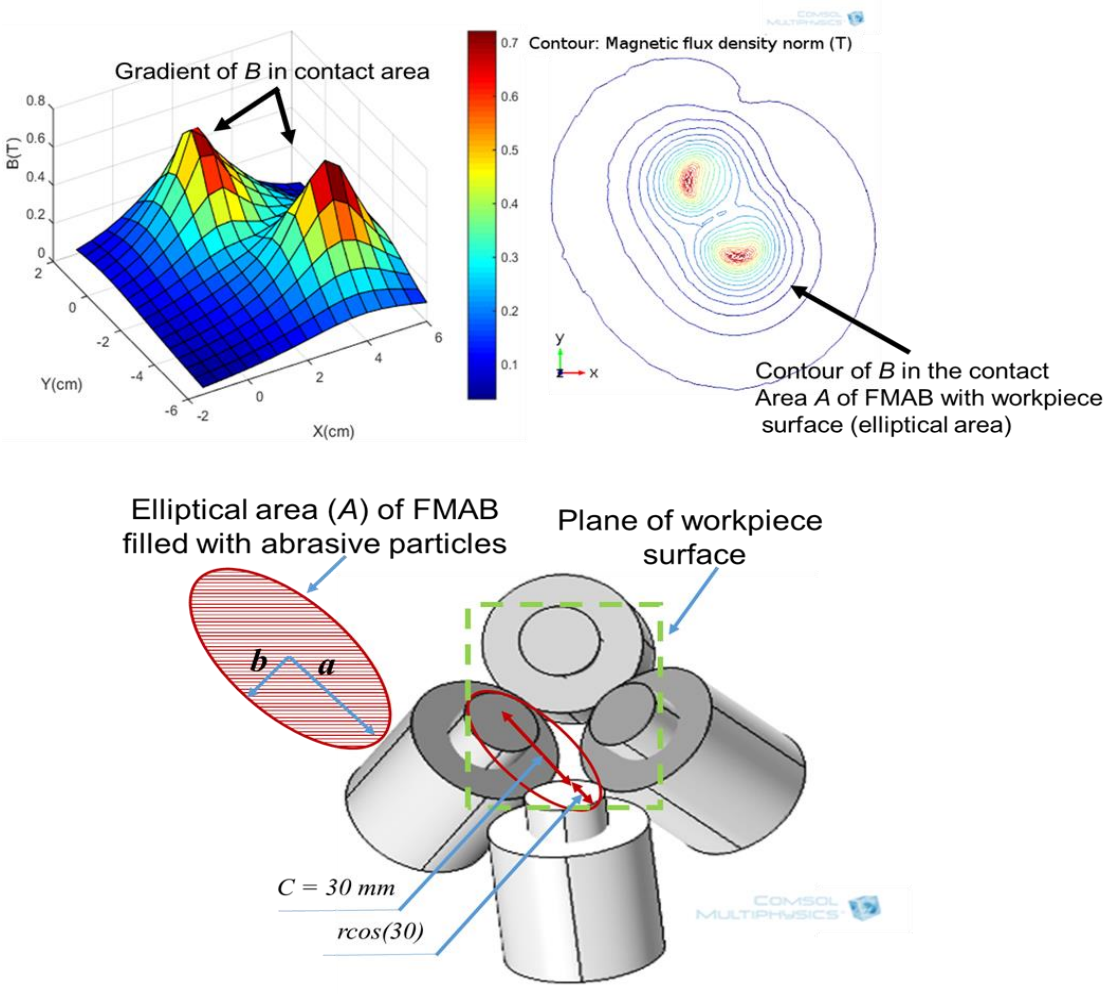

Figure 5. 19: Schematic of the area A of (FMAB) according to the cantor of magnetic field distribution.

As shown in Figure 5.19, the area $\boldsymbol{A}$ can be considered an elliptical area if only two adjacent electromagnets are energized. Therefore:

$$A = \pi ab = \pi \left(\frac{c}{2} + r cos\theta\right) r \tag{5.25}$$

where $\boldsymbol{C}$ is the distance measured from center to center for adjacent electromagnets of the system setup configuration and it is equal to 30 mm, $\boldsymbol{r}$ is the radius of the extended core equal to 1mm, and $\theta = 30°$ is the alignment angle of the electromagnet with the *Z* axis (vertical axis). In order to simplify the calculation, *b* could be considered equal to *r*. So:

$$A = \pi \left(\frac{30}{2} + 1 \times \cos 30\right) \times 1 = 49.90\ mm^2$$

Therefore,

$$F_{mz} = PA = 0.136\ \text{MPa} \times 49.90\ mm^2 = 6.786\ N$$

and the normal component of the magnetic force on each abrasive particle f_{mz} can be evaluated as:

$$f_{mz} = \frac{F_{mz}}{n_a} \tag{5.26}$$

where $\boldsymbol{n_a}$ is the number of the active abrasive particles which are in touch with the surface of the work-piece. This can be obtained from:

$$n_a = \frac{A}{\frac{\pi}{4} d_{map}^2} \tag{5.27}$$

where $\boldsymbol{d_{map}}$ is the diameter of a single magnetic abrasive particle (MAP), and it can be obtained according to the mesh size. For example, if $\boldsymbol{d_{map}} = 0.1\ mm$ (140 U.S Mesh), then:

$$n_a = \frac{49.90\ mm^2 A}{\frac{\pi}{4} 0.1^2} = 6353.46 \approx 6354 \text{ particles}$$

$$f_{mz} = \frac{F_{mz}}{n_a} = \frac{6.786}{6354} = 0.001\ N$$

5.6.2. Modeling of the Tangential component (F_{mt})

The tangential force component F_{mt}, which acts in a horizontal direction parallel to the workpiece surfaces, is responsible for removing material from the workpiece. This component represents the force components in the *x*-*y* plane, which are F_{mx} and F_{my}. Therefore, the tangential force component can be evaluated as:

$$F_{mt} = \sqrt{F_{mx}^2 + F_{my}^2} \tag{5.28}$$

where,

$$F_{mx} = \mu o\ v \left[\left(Mx\frac{\partial Hx}{\partial x} + My\frac{\partial Hx}{\partial y} + Mz\frac{\partial Hx}{\partial z}\right)\right] \tag{5.29}$$

$$F_{my} = \mu o\ v \left[\left(Mx\frac{\partial Hy}{\partial x} + My\frac{\partial Hy}{\partial y} + Mz\frac{\partial Hy}{\partial z}\right)\right] \tag{5.30}$$

and the tangential component of the magnetic force on each abrasive particle f_{mt} can be evaluated as:

$$f_{mt} = \frac{F_{mt}}{n_a} \tag{5.31}$$

5.6.3. Modeling of abrasive particle

The modeling of the abrasive particle depends on the shape and geometry of the particle. Some of the previous studies considered a tetrahedral shape for the abrasive particle [14], [64]. Figure 5.20 illustrates a microscopic image for Aluminum Oxide abrasive particles which are used in this study.

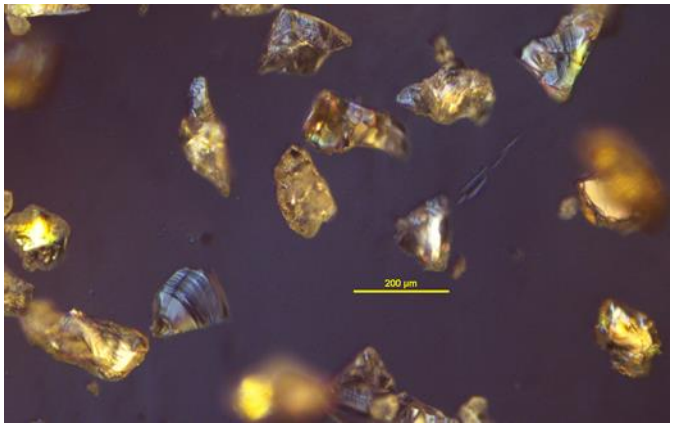

Figure 5. 20: Aluminum Oxide abrasive particle.

Particles in this model have been considered as identical tetrahedral grains, and the penetration model is illustrated in Figure 5.21 [64].

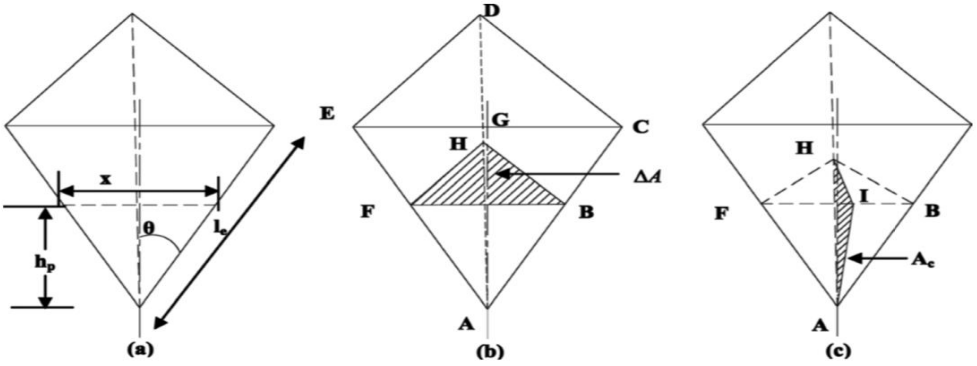

Figure 5. 21: Penetration of a tetrahedral magnetic abrasive particle: (a) Depth of penetration, (b) Projected area of indentation, and (c) Projected area of penetration [64].

In Figure 5.21 above, $\Delta \boldsymbol{A}$ represents the projected area of indentation, $\boldsymbol{A_c}$ is the projected area due to penetration which shears off the peaks of the workpiece material, and $\boldsymbol{h_p}$ is the depth of penetration on the inclined face of the abrasive particle. Nano-hardness tests are usually used to understand the role of the various abrasives particles in the metal removal processes, as illustrated in Figure 5.22. The depth of penetration can be determined as follows:

$$\tan\theta = \frac{x}{2h_p} \tag{5.31}$$

$$\Delta A = Area\ of\ \Delta BFH = \frac{\sqrt{3}}{4}x^2 \tag{5.33}$$

$$f_z = H_d \Delta A = H_d \frac{\sqrt{3}}{4}x^2 = H_d \frac{\sqrt{3}}{4} \times 4h_p^2 tan^2\theta \tag{5.34}$$

$$h_p^2 = \frac{1}{\sqrt{3}} \frac{f_{mz}}{h_d} \frac{1}{tan^2\theta} \tag{5.35}$$

$$h_p = \frac{0.577}{tan\theta} \sqrt{\frac{f_{mz}}{H_d}} \tag{5.36}$$

Therefore, for $f_{mz} = 0.001N$,

$$h_p = \frac{0.577}{tan60} \sqrt{\frac{0.001}{200 \times 10^6}} = 7.45 \times 10^{-7} m$$

Figure 5.23 shows an example of the relationship between the indentation load and the penetration depth.

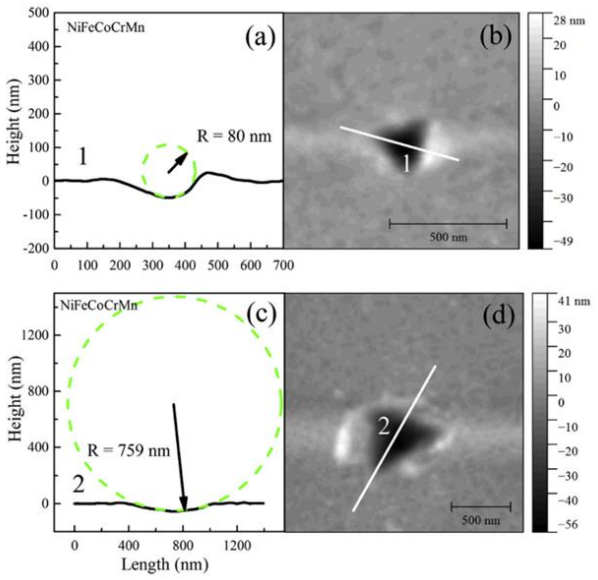

Figure 5. 22: A nanohardness test illustrates the indentation profiles of different radii [65].

Accordingly, many models are proposed to explain the mechanism of the interaction between the abrasive particle and the finished surface. It can be noticed that most of these models are based on controlling the main parameters such as the finishing pressure, sliding velocity, and the geometry of the scratch that formed on the workpiece surface [66].

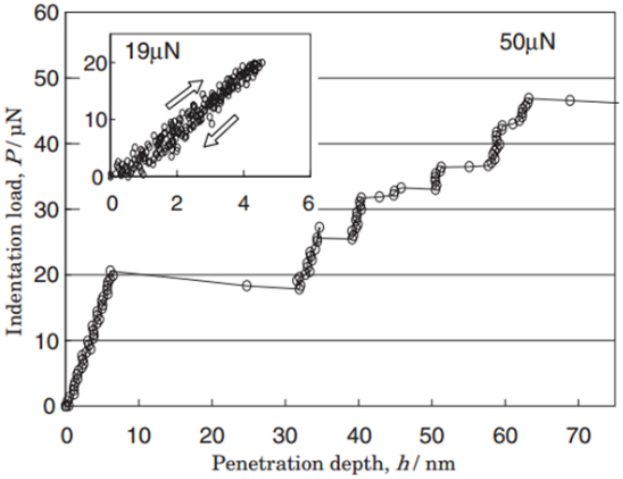

Figure 5. 23: Example of the variation of penetration depth with the indentation load [67].

The normal force for a single abrasive particle can be estimated depending on the hardness of the workpiece material H_d as [64]:

$$f_{mz} = Hd\,\Delta A \tag{5.37}$$

Also $\boldsymbol{A_c}$ can be estimated as [24]:

$$A_c = \frac{3f_{mz}}{4H_d} \tag{5.38}$$

5.7. Metal Removal

The rotation of the magnetic field causes a rotation of the MAPs. When the cutting edges of the abrasive particles are in mechanical contact with the surface of the workpiece and the magnetic force is a sufficient amount, the material will be removed as illustrated in Figure 5.24.

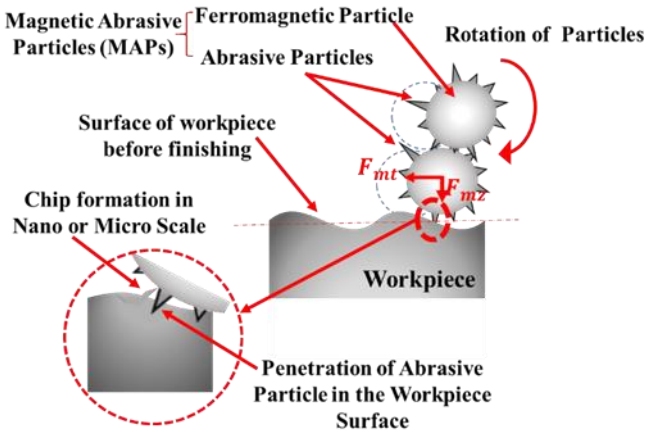

Figure 5. 24: Forces on a single abrasive particle.

The abrasive particles should be under the effect of both components of the magnetic force, the normal component and the tangential component. The tangential component should be equal to or greater than $\boldsymbol{f_c}$, which represents the cutting force required to produce a micro-chip by removing metal from the surface of the workpiece. $\boldsymbol{f_c}$ depends on the projected area $\boldsymbol{A_c}$ in Figure 4.24c, and another important mechanical property of the workpiece material, shear strength (τ_s) [5].

Therefore,

$$\boldsymbol{fc} = \tau_s A_c \tag{5.39}$$

This cutting force, in order to remove the material, should be more than the plastic deformation resistance of the workpiece material. Otherwise, the abrasive particle cannot remove the material and it might just rotate on the surface with a reduction in the depth of indentation [24], as shown in Figure 5.24.

Therefore, three expectations can be predicted for removing the material in the magnetic abrasive finishing process [5]:

a. $\boldsymbol{fc} = f_{mt}$ (5.40)

This represents an equilibrium situation: when the removal process can be started.

b. $\boldsymbol{fc} < f_{mt}$ (5.41)

Material is removed in this situation.

c. $\boldsymbol{fc} > f_{mt}$ (5.42)

This situation means no cutting can occur due to the insufficient depth of penetration of an abrasive cutting edge, and the abrasive can merely rotate.

Therefore, when:

$$f_{mz} = \frac{F_{mz}}{n_a} = \frac{6.786}{6354} = 0.001\ N$$

and the material of the workpiece used is Aluminum, the shear strength τ_s for the workpiece material is 207 MPa, and the hardness H_d is 107 Vickers. Therefore, A_c can be estimated as:

$$A_c = \frac{3f_{mz}}{4H_d} = (3 \times 0.001)/(4 \times 107 \times 9.807) = 7.147 \times 10^{-13}\ m^2$$

The required cutting force can be estimated from:

$$\boldsymbol{fc} = \tau_s A_c = 207 \times 10^6 \times 7.147 \times 10^{-13} = 0.0001\ N$$

The value of $\boldsymbol{fc}$ was compared with the value of $\boldsymbol{f_{mt}}$, which was obtained from the analytical solution and it was approximately 0.0002 *N*, as shown in Figure 5.25, which means $\boldsymbol{fc} < \boldsymbol{f_{mt}}$ and the material is removed.

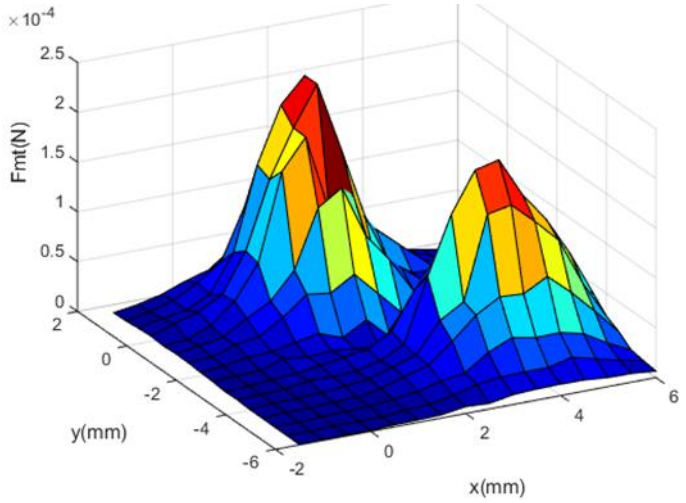

Figure 5. 25: The variation of force tangential component on the surface of the workpiece.

The required cutting force was also compared with the calculated tangential component from the equation:

$$F = \mu o \, v(M.\nabla)H$$

where the values of $(M.\nabla)H$ were obtained by finite element solution from COMSOL Multiphysics® version 5 simulation software. All the values approximately match each other, as illustrated in Figure 5.26.

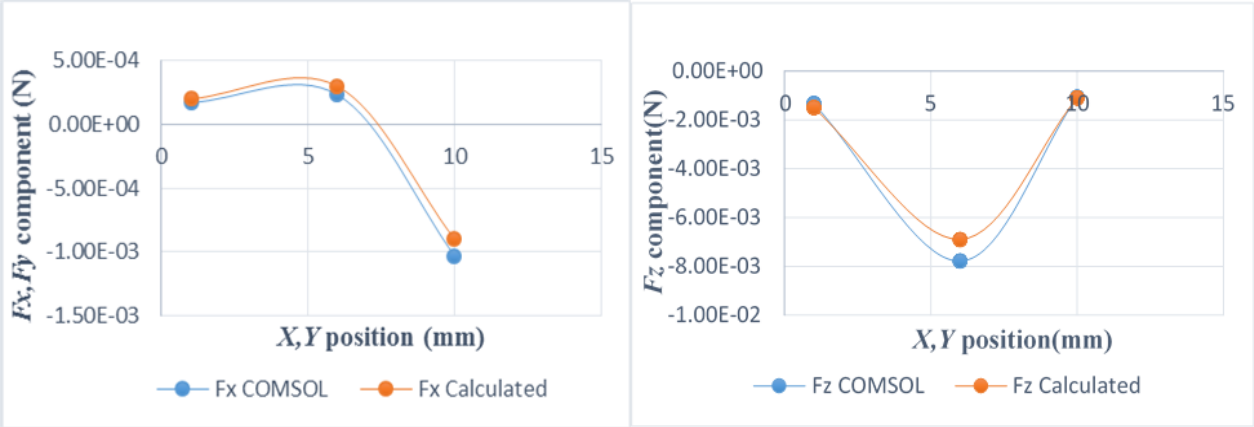

Figure 5. 26: Comparison between calculated and simulation values of force component.

5.8. Conclusion

This chapter described the main components of the system and the essential function of each component. In addition, it has explained the fundamental models used to represent the relationship between the main parameters of the Magnetic Abrasive Finishing (MAF) process. The Finite Element Method was used to find the parameter solutions and the model was started with classical Maxwell's equations as the governing set. Furthermore, the theory presented and applied herein remained applicable with the introduction of scaling factors that reduce expected field component magnitudes for the analytical and simulation results in order to bring them in line with those of the experiments. Processing of experimental results was proven successful via verification of the curve fit results checked against experimental iron core data. The results generated the same level of acceptable error for both the norm of the magnetic field as well as the adjusted components. Polynomial curve fitting was adequate for the norm, whereas sum of sines proved more adequate for components.

This chapter further analyzed the variation of the magnetic field (B) in the working gap with respect to the magnetization effect of the particles and the electromagnets' angle of alignment. The main target was to generate a rotating magnetic field which would be able to carry MAPs and perform the finishing process with a sufficient amount of magnetic force (cutting force). The magnetic force had a normal component, F_{mz}, and a tangential component, F_{mt}.

It was further presented that the normal component which was applied to a single abrasive particle, f_{mz}, should be sufficient to force the abrasive particle to penetrate the workpiece surface. This component depends on the hardness (H_d) of the workpiece material and the projected area of indentation ($\Delta \boldsymbol{A}$), as in equation (5.54). The tangential component which is applied to a single abrasive particle, f_{mt}, should be sufficient to shear the material tangentially. This component should be greater than the required cutting force, fc, which depends on the shear strength of the workpiece material (τ_s) and the projected sheared area ($\boldsymbol{A}_c$), as in equation (5.56).

The best configuration of the electromagnets which can be satisfied with these conditions was analyzed in this chapter. The best configuration means the one that can make the component of B in a tangential direction, B_{xy}, greater than the component of B in a normal direction, B_z. Thus, the tangential force component, F_{mt}, will be greater than the normal force component, F_{mz}. This is important to make the particles on the workpiece surface move tangentially according to the rotation of the magnetic field and accomplish the finishing process.

It was found that the best configuration can be obtained when the electromagnets are aligned along the perpendicular axis, one on the X axis and the other on the Y axis as shown in Figure 5.16, with the angle of alignment $\theta = 30^{\circ}$ for each electromagnet with respect to the normal direction, as shown in Figure 5.19. The B_{xy} component should be greater than B_z especially when each two neighboring electromagnets are energized together within the duty cycle.

Applying these setup conditions, to perform experiments and test the proposed concept showed that the surface roughness of an Aluminum specimen, for example, can be improved from 328.83 nm to 278.45 nm.

Chapter 6

Fuzzy Logic Prediction Model

6.1. Introduction

The conventional method of identifying specific finishing parameters to attain a precise surface roughness basically requires a trial and error approach. The main deficiencies of this approach are the time-consumed and the inability to include combinations of all parameters while providing a reliable predicting model of the surface roughness and examining all process parameters in as few as possible experimental trials [67]. Hence, using the conventional mathematical and analytical techniques to predict the process performance of finishing processes may not give optimal and highly accurate results [68]. Advanced computing techniques, such as fuzzy logic, genetic algorithm, particle swarm optimization, and simulated annealing have been successfully used to overcome the limitations of conventional methods, due to their ability to model and predict phenomena and analyze non-linear and multi-dimensional engineering and functional problems [69].

Fuzzy logic can be considered as an identifying system technique. It is usually used for monitoring and diagnostics of machining processes because it is able to model the input-output relationship efficiently and overcome the problems of non-linearity and the probability of uncertainty [70]. Many studies have been conducted previously applying this technique to estimate surface roughness during milling and turning of different materials [71]. Lo [72] applied a fuzzy logic model to predict the surface roughness in the milling process. The model prediction accuracy was around 96%. Ramesh et al. [73] conducted a fuzzy logic model to predict the cutting parameters in turning titanium alloy and controlling the cutting forces. Unune et al. [68] applied a fuzzy logic artificial intelligence method to predict the average surface roughness and metal removal rate during the machining process of Nimonic 80A using an abrasive-mixed electro-discharge diamond surface grinding (AMEDDSG) technique. The agreement between the experimental results and the fuzzy logic model was 93.89%. Kanish et al. [74] developed a fuzzy logic model to predict the improvement of surface roughness of SS316L material using the Magnetic Field Assisted Abrasive Micro Finishing (MFAAF) method. The maximum deviation between the developed predicted model and the experimental results was around 7.16%. Frad et al. [75] proposed an adaptive neuro-fuzzy inference system to predict the process characteristics based on experimental observation during application of the Dry Wire Electrical Discharge Machining process on an Al–SiC metal matrix composite. They used Analysis of

Variances (ANOVA) to identify significant factors and correlate relationship between process inputs and output.

Thus, the intricate and nested relationship between the machining parameters in Magnetic Abrasive Finishing (MAF) makes the selection of the proper parameters a difficult task. This problem can be overcome by using the fuzzy logic technique and its ability to use the characteristic function replacement of a membership function with the ranging of values between (0 to 1) to obtain the best solution and optimize the process parameters [76].

6.2. Experiments Parameters

The process parameters and their levels that are used in the experiments are illustrated in Table 6.1. The input parameters in this process are the applied voltage, frequency of energizing the electromagnets, abrasive particle size, and operating time. Additionally, the output parameters are the average surface roughness (Ra) and reduction percentage of surface roughness (%RS). Taguchi systematic approach was used to design the experiments to optimize the process parameters of finishing an aluminum 6061 sample.

Table 6.1: Parameters and Levels used in the experiments

Notation	Process Parameters	Unit	Levels			Observed Value	
			L	M	H	Average Surface Roughness (μm)	Reduction Percentage of Surface Roughness
A	Applied Voltage	V	20	25	30		
B	Frequency	Hz	2	6	10		
C	Time	min	15	30	60		
D	Particle Size	μm	100	75	37		

L: low, M: medium, H: high

Taguchi L9 orthogonal array has been chosen for running the experiments with four parameters and three levels, as illustrated in Table 6.2. Three levels were selected for each input finishing factor, as shown in Table 6.1. The Ra and %RS were chosen as observed values. The experiments were conducted using Al-6061-T6 alloy samples. To accurately obtain the surface roughness measurement, a Laser Scanning Confocal Microscope was used to measure the surface roughness of the samples before and after the finishing process and obtain Ra values. Then, %RS was calculated based on the before and after Ra values. In order to get accurate results, the single measurement was repeated three times, then the mean value was chosen as an observed value (Appendix C). Figure 6.1 shows the morphology of an Al sample surface

before and after the finishing process using the SMAF technique with machining parameters. The values of the average surface roughness before the finishing process were 12.35 µm (a) and 11.62 µm (c). These values were improved after implementing the finishing process to 6.21 µm (b) and 8.16 µm (d). Machining conditions for (a) were applied voltage 30 V, frequency 2 Hz, operating time 60 min, and size of particles 75 µm, while for (c) were applied voltage 20 V, frequency 2 Hz, operating time 15 min, and size of particles 100 µm. It can be observed that the SMAF process results in better surface and narrower profile cavities. Thus, it can be inferred that the SMAF technique will lead to better machining performance.

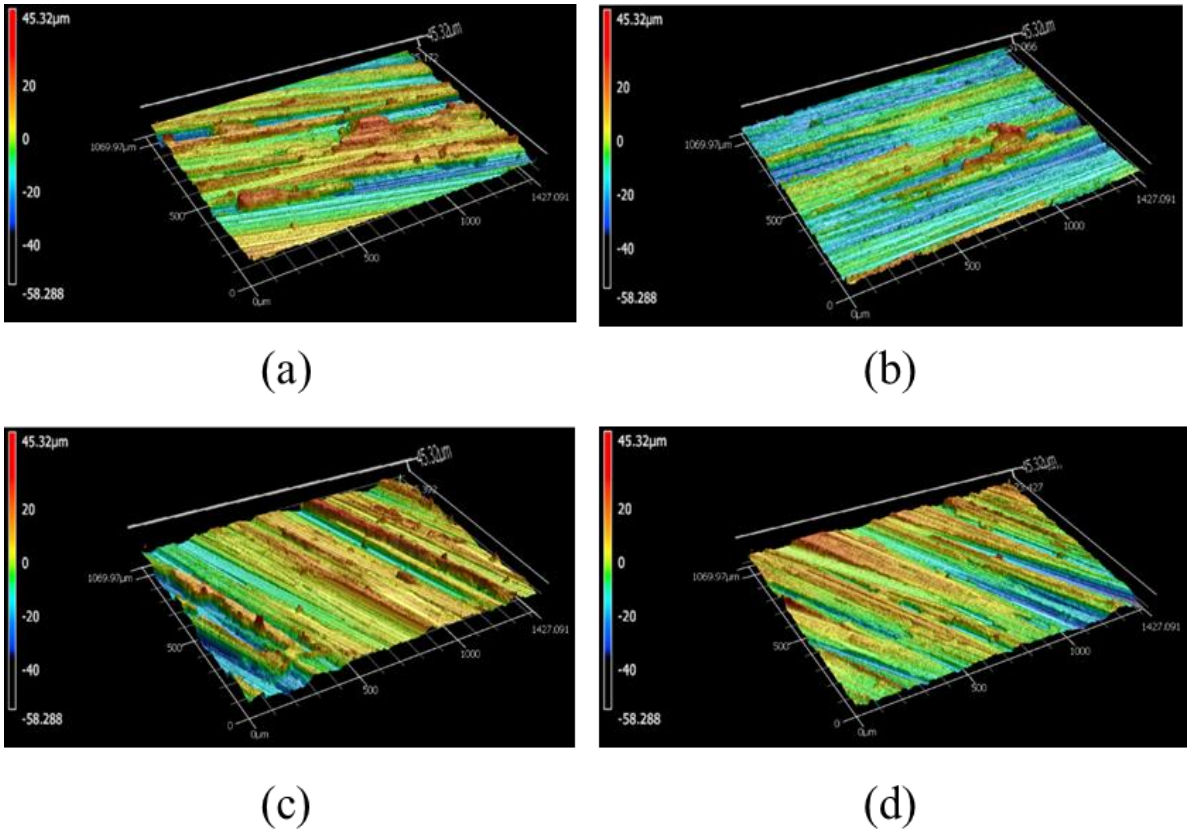

Figure 6. 1: The morphology of Al sample surface (a) and (c) before, and (b) and (d) after.

6.3. Taguchi Method

To study the general performance of any process or system, experiments have been conducted to identify the effective parameters based on the results of these experiments. The conventional method used to evaluate system parameters is a trial and error approach, which means too many trials should be applied in order to obtain the optimal results. Later, a full factorial experiment approach was used as an alternative to the first approach. One of the advantages of this approach is its ability to study all possibilities for obtaining optimal parameters of the process. However, both of these approaches need to conduct a large number of trials to get the optimal results, which means high cost in terms of time and money [77].

In order to fix these problems, Taguchi method was developed. It is an experimental design technique used to optimize system characteristics, or product qualities, and reduce the system performance sensitivity by evaluating the optimal parameter settings [78]. Taguchi technique employs the concept of the orthogonal array (OA) and signal to noise ratio (SN ratio) to identify the optimal parameters and conditions for the process. The advantage of applying the orthogonal array concept is reduction of the number of experimental trials to study the combination between the parameters and achieve the optimal conditions. This approach ensures that all parameters with all levels will be equally trialed. In the current study, Taguchi Systematic Approach (TSA) was used to design the experiments to optimize the process parameters of finishing an aluminum 6061 sample. Moreover, Taguchi method was applied in conjunction with fuzzy logic technique to model the SMAF process and predict the operation performance in finishing the aluminum specimens. Table 6.1 illustrates the finishing parameters used in the experiments. Taguchi L9 and L25 orthogonal arrays were selected for designing the experiments. Taguchi L9 OA was chosen for running the experiments with four input parameters and three levels, as illustrated in Table 6.2, while Taguchi L25 OA was chosen to build the fuzzy logic predicted model with four input parameters and five levels.

The experimental layout according to Taguchi L9 orthogonal array for the measured values of Ro (the initial value of the surface roughness), Ra (the average value of the surface roughness of finished surface after the machining process), and the calculated values of %RS are illustrated in Table 6.3. %RS was calculated as $(\frac{Ro-Ra}{Ro} \times 100\%)$.

Table 6.2: Experimental layout using an L9 orthogonal array

No	Process Parameters				Observed Value	
	Applied Voltage (A)	Frequency (B)	Time (C)	Particle Size (D)	Average Surface Roughness (μm)	Reduction Percentage of Surface Roughness
1	L	L	L	L		
2	L	M	M	M		
3	L	H	H	H		
4	M	L	M	H		
5	M	M	H	L		
6	M	H	L	M		
7	H	L	H	M		
8	H	M	L	H		
9	H	H	M	L		

Table 6.3: Experimental layout and results based on Taguchi L9 OA

No.	App. Volt.	Freq. Hz	Time min	Par. Size μm	Ro μm	Ra μm	%RS
1	20	2	15	100	11.6212	8.1623	29%
2	20	6	30	75	11.3981	8.5327	25%
3	20	10	60	37	12.1763	8.1158	33%
4	25	2	30	37	11.9318	7.6306	36%
5	25	6	60	100	12.1380	7.6897	36.6%
6	25	10	15	75	10.9118	7.8501	28%
7	30	2	60	75	12.3555	6.2170	49.6%
8	30	6	15	37	12.7799	8.1030	36.6%
9	30	10	30	100	12.3535	7.54346	39%

6.4. Fuzzy Logic

Fuzzy logic is one of the most important computational techniques that can be used to describe and model the input-output relationship of any process. It has become a common tool which usually is applied in modeling a wide spectrum of machining processes [76]. In fuzzy logic, linguistic terms and rules are usually used to describe the input-output relationship and develop subset membership functions to modify

numerical variable problems. There exists a willingness to assign membership functions to recognized forms. These recognized forms generally represent linear and nonlinear functions. Triangular, trapezoidal, left-shoulder, and right-shoulder are examples of the linear membership functions. Likewise, for the nonlinear membership functions, standard Gaussian or Sigmoid type curves are usually used [79]. Fuzzy logic technique has an ability to use the characteristic function replacement of a membership function with a range of values between (0 to 1) to obtain the best solution and optimize the process parameters. Also, the possibilities offered in fuzzy logic give an amount of a subset's probability to belong to another subset [76]. Further, fuzzy logic utilizes the accumulated experience and background knowledge based on practice instead of theoretical approaches [68], [80]. To simulate nonlinear systems, fuzzy logic considers the effects and physical combination of all variables.

The fuzzy logic artificial intelligence model offers a precise prediction of finishing performance because it is a continuous transformation from true to false conditions. It employs this continuous conversion of the subset membership to change the numeric variables to fuzzy linguistic regions. Thus, this technique uses the conventional language to define the variables and utilizes the fuzzy linguistic rules to describe the parameter relationships, to avoid dealing with mathematical functions and numeric variables [76].

In this study, a fuzzy logic technique was used to select better finishing parameters and predict the average surface roughness (Ra) and reduction percentage of surface roughness (%RS) during the finishing process using SMAF. The input parameters in this process, as mentioned, are the applied voltage, frequency of energizing the electromagnets, abrasive particle size, and operating time. Additionally, the output parameters are Ra and %RS. The input and output parameters were used to build the structure of the fuzzy logic prediction model, shown in Table 6.4.

Table 6.4: Parameters and levels used for the prediction model

Observed value	Factor	Run# 1	Run# 2	Run# 3	Run# 4	Run# 5
Surface Roughness (μm)	Applied Voltage (V)	20	22	25	27	30
	Frequency (Hz)	2	4	6	8	10
	Time (minute)	15	23	30	45	60
	Particle Size (μm)	37	56	75	88	100

To define the input and output parameters in the fuzzy logic model, fuzzy expression and fuzzy linguistic variables were used. As illustrated in Table 6.5, for the input parameters, five membership functions were used for each parameter: very low (VL), low (L), medium (M), high (H), and very high (VH). These

membership functions were also used for the output variable %RS. Whereas, for the Ra output variable, excellent (E), good (G), average (Av), bad (Ba), and rough (R) were selected as membership functions.

Table 6.5: Fuzzy linguistic and variables characteristics of the parameters

Parameters	Linguistic variable	Range
Applied voltage [V]	VL,L,M,H,VH	20-30 [V]
Frequency [Hz]	VL,L,M,H,VH	2-10 [Hz]
Time [min]	VL,L,M,H,VH	15-60[min]
Particle size [µm]	VL,L,M,H,VH	37-100 [µm]
Average surface roughness [µm]	E [excellent], G [good], A [average], B [bad], R [rough]	6.21-8.53 [µm]
Percentage of surface roughness reduction	VL,L,M,H,VH	25%-49%

Based on the obtained experimental results which were achieved in Table 6.3, and using obtained experience and background knowledge, the Taguchi L25 orthogonal array was chosen, and designed to build the fuzzy logic predicted model decidedly using four input parameters and five levels, as shown in Table 6.4. The reason behind using L25 instead of L9 Taguchi orthogonal array to develop a fuzzy logic prediction model was to increase the accuracy and obtain a higher smoothness in the membership function. MATLAB software fuzzy toolbox was used to adjust the linguistic variable range with respect to the corresponding membership functions and compute the results of this model. Tables (6.6 and 6.7) show the linguistic variable range of the input and output parameters associated with the membership functions.

Table 6.6: Input factors and levels for the prediction model

Parameter	Symbol	VL	L	M	H	VH
Applied voltage [V]	A	20	22	25	27	30
Frequency [Hz]	B	2	4	6	8	10
Time [min]	C	15	23	30	45	60
Particle size [µm]	D	37	56	75	88	100

Table 6.7: Output factors and levels for the prediction model

	E	G	Av	Ba	R
Average surface roughness [µm]	6.0 – 7.0	7.1 – 7.4	7.5 – 7.6	7.7 – 7.9	8.0 – 8.5
Percentage of surface roughness reduction	VL	L	M	H	VH
	0.20 – 0.29	0.30 – 0.35	0.36 – 0.39	0.40 – 0.44	0.45 – 0.50

6.5. Membership Function

To develop an accurate model using the fuzzy logic technique, a membership function must be chosen carefully. A membership function can be defined as a description of the input values distribution of probabilities with respect to the particular function or degree of membership within the range of 0 to 1. The framed forms of the linear membership functions are triangular, trapezoidal, left-shoulder, and right-shoulder. On the other hand, standard Gaussian and Sigmoid type curves represent the well-known forms of the nonlinear membership functions [79].

In this study, the standard Gaussian membership functions were utilized to describe the fuzzy set for the input parameters (applied voltage, frequency, operating time, and particle size), as demonstrated in Figure 6.2. Meanwhile, triangular membership functions were chosen for the output parameters (average surface roughness and percentage of surface roughness reduction), as illustrated in Figure 6.3. Use of the standard Gaussian membership functions for the input parameters allowed smoothness in the membership functions and increased the prediction accuracy. Nevertheless, the triangular membership functions were chosen for the output parameters due to their linearity and the capability of describing the function behavior precisely. Moreover, the number of the unknown output parameters of the membership function for the triangular function is three which is less than that of the trapezoidal membership function (which is four). Therefore, using a triangular membership function for the output parameters provided a better agreement with the experimental results, as it required fewer trials to achieve the value of the consequent parameters.

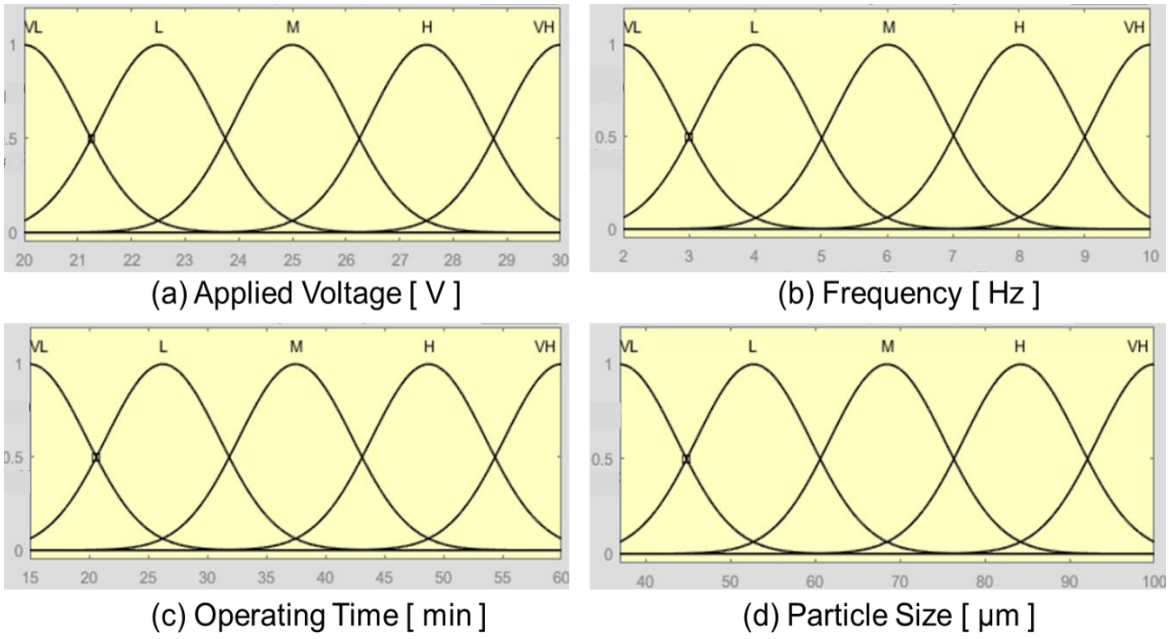

Figure 6. 2: Gaussian membership function for input parameters (a) applied voltage (b) frequency (c) time (d) particle size.

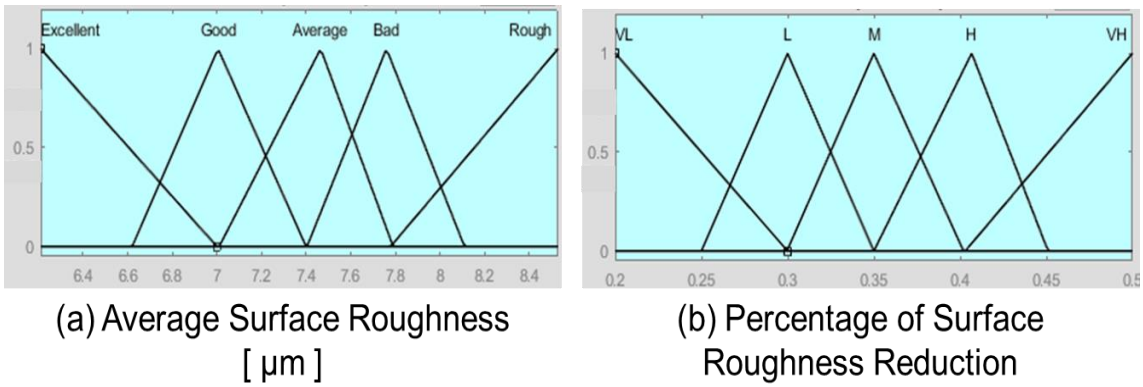

Figure 6. 3: Triangular membership function for output parameters (a) average surface roughness (b) percentage of surface roughness reduction.

The formula used to define the linguistic terms of the Gaussian membership function, was [81]:

$$\mu_A^i(x) = \exp\left(-\frac{(c_i - x)^2}{2\sigma_i^2}\right) \tag{6.1}$$

where $\mu_A^i(x)$ represents the membership function (MF) for the fuzzy set *A* which ranges between (0 and 1), and c_i and σ_i are the center and width of the i^{th} fuzzy set A^i, respectively, as demonstrated in Figure 6.4.

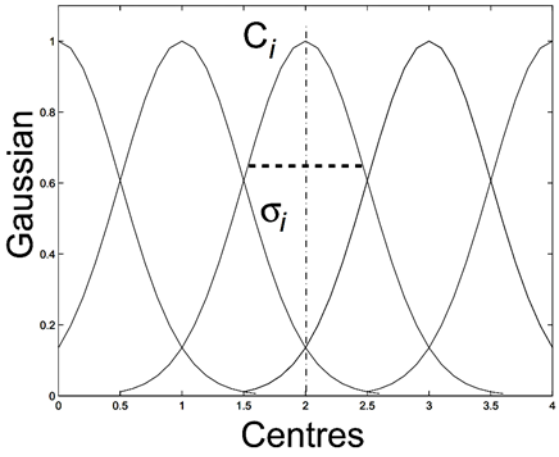

Figure 6. 4: Gaussian parameters [81].

Similarly, the formula of the triangular membership function which is used to characterize the output term is defined by three parameters (*a*, *b*, *c*) as:

$$f(x; a, b, c) = \begin{cases} 0, & x \le a \\ \dfrac{x-a}{b-a} & a \le x \le b \\ \dfrac{c-x}{c-b} & b \le x \le c \\ 0, & c \le x \end{cases} \tag{6.2}$$

where *a*, *b*, and *c* represent the triangular fuzzy triplet and can be used to calculate the three points of the triangular membership function on the X axis. The input-output numerical values are represented by linguistic terms, which can be obtained by designing membership functions (MF) of the fuzzy set variables. Linguistic variable terms such as very low (VL), low (L), medium (M), high (H), and very high (VH) represent the input variables of applied voltage, frequency, operating time, and particle size. Also, this representation was considered for one of the two output variables, the percentage of surface roughness reduction. The other output variable, average surface roughness, was represented by using membership functions including excellent (E), good (G), average (Av), bad (Ba), and rough (R). Table 6.8 summarizes the input-output variables and levels according to L25 Taguchi OA.

Table 6.8: Input and Output factors and levels for the prediction model according to L25 Taguchi OA

Exp. No.	Input Variables					Output Variables	
	Volt	Freq.	Time	Part	R_o	Ra	%RS
1	20	2	15	37	11.6212	8.1323	0.3002
2	20	4	23	56	11.5923	8.1712	0.2951
3	20	6	30	75	11.3981	8.4832	0.2557
4	20	8	45	88	12.1162	8.3262	0.3128
5	20	10	60	100	11.5214	8.0916	0.2976
6	22	2	23	75	11.7215	7.7213	0.3412
7	22	4	30	88	11.6854	7.8325	0.3297
8	22	6	45	100	12.0145	7.7925	0.3514
9	22	8	60	37	11.8578	7.6897	0.3515
10	22	10	15	56	11.6987	7.8114	0.3322
11	25	2	30	75	11.9318	7.5306	0.3688
12	25	4	45	37	11.6358	7.6538	0.3422
13	25	6	60	56	12.1380	7.6897	0.3664
14	25	8	15	75	11.7254	7.7025	0.3430
15	25	10	23	88	10.9124	7.7992	0.2852
16	27	2	45	56	11.8245	6.7598	0.4283
17	27	4	60	75	11.5985	7.1857	0.3804
18	27	6	15	88	11.7584	7.6835	0.3465
19	27	8	23	100	12.0157	8.0541	0.3296
20	27	10	30	37	11.2485	8.2012	0.2709
21	30	2	60	88	12.3555	6.1817	0.4996
22	30	4	15	100	10.9857	8.0030	0.2715
23	30	6	23	37	12.6979	7.9103	0.3770
24	30	8	30	56	11.7215	7.5368	0.3570
25	30	10	45	75	11.6857	7.2943	0.3757

6.6. Structure of Fuzzy Rules

This model contains fuzzy rules based on sets of IF-THEN statements to describe the relationship between the input and output parameters. IF-THEN statements for 25 rules of 4 input parameters applied voltage (A), frequency (B), operating time (C), and particle size (D) with 2 output parameters, average surface roughness (Ra) and reduction percentage of the surface roughness (RS%) were taken under consideration. Table 6.9 demonstrates IF-THEN statements for 25 fuzzy logic rules based on the conditions illustrated in Table 6.8.

Table 6.9: Rules for the fuzzy logic prediction model according to L25 Taguchi OA

Rule number	If statements (input parameters)				Then statement (response variable)	
	A	B	C	D	%RS	Ra
1	VL	VL	VL	VL	L	R
2	VL	L	L	L	VL	R
3	VL	M	M	M	VL	R
4	VL	H	H	H	L	R
5	VL	VH	VH	VH	VL	R
6	L	VL	L	M	L	Ba
7	L	L	M	H	L	B
8	L	M	H	VH	L	B
9	L	H	VH	VL	L	Av
10	L	VH	VL	L	L	Ba
11	M	VL	M	M	M	Av
12	M	L	H	VL	L	Av
13	M	M	VH	L	M	Av
14	M	H	VL	M	L	Ba
15	M	VH	L	H	VL	Ba
16	H	VL	H	L	H	E
17	H	L	VH	M	M	G
18	H	M	VL	H	L	Av
19	H	H	L	VH	L	Ba
20	H	VH	M	VL	VL	R
21	VH	VL	VH	H	VH	E
22	VH	L	VL	VH	VL	R
23	VH	M	L	VL	M	Ba
24	VH	H	M	L	L	Av
25	VH	VH	H	M	M	G

The fuzzy logic output was obtained from these fuzzy rules by applying the concept of maximum-minimum compositional process. This concept can be clarified throughout the following example.

Suppose that A, B, C, and D represent four input parameters of the fuzzy logic model, then the output fuzzy logic membership functions will be [76]:

$$\mu_{X_0Y_0}(E)(F) = [\mu_{L_1}(A) \wedge \mu_{M_1}(B) \wedge \mu_{N_1}(C) \wedge \mu_{O_1}(D) \wedge \mu_{X_1}(E)\mu_{Y_1}(F) \vee \ldots$$
$$\times \quad \mu_{L_i}(A) \wedge \mu_{M_i}(B) \wedge \mu_{N_i}(C) \wedge \mu_{O_i}(D) \wedge \mu_{X_i}(E)\mu_{Y_i}(F) \tag{6.3}$$

where $\wedge$ is the maximum and $\vee$ is the minimum operation and L_i, M_i, N_i, and O_i are fuzzy subsets distinctive by their corresponding membership functions, μ_{L_i}, μ_{M_i}, μ_{O_i}, μ_{X_i}, μ_{Y_i}, respectively. The corresponding membership functions, as previously mentioned, are standard Gaussian for the input variables and triangular for the output variables.

6.7. Defuzzification

Defuzzification process can be defined as an interpretation of fuzzy set information into numerical data. This means generating a precise numerical value from the fuzzy quantity. It is considered an essential and crucial part of the fuzzy logic approach because the fuzzification and fuzzy system procedures provide a systematic description of the fuzzy set region and real-valued scalar region [76]. Many methods are usually employed for the defuzzification process, such as centroid, center of sum, center of largest area, weighted average, and mean of max [82]. However, the commonly used defuzzification techniques are mean of maximum, and center of area [83].

6.7.1. Mean of Maximum (MOM)

In this technique, the average of the output values which have the highest degrees of possibility are calculated to generate one crisp number. The formula used to determine the MOM defuzzification technique is:

$$MOM(A) = \sum_{j=1}^{k} \frac{x_j}{k} \tag{6.4}$$

where x_j represents the point at which the membership function is maximum (with highest possibility degree), and *K* is the number of times the output distribution reaches the maximum level, as shown in Figure6.5.

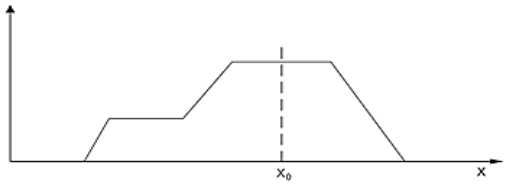

Figure 6.5 : Demonstrated example of MOM.

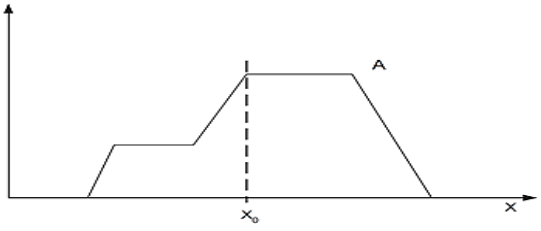

Figure 6.6: Demonstrated example of COA.

6.7.2. Center of Area (COA)

The center of area technique, which is also called the center of gravity technique, is based on determining the center point of the objected fuzzy area by calculating the weighted mean of the output fuzzy area. In this method, the area under the scaled membership functions is calculated within the range of the output variable and the best compromise between multiple output linguistic terms can then be obtained, as illustrated in Figure 6.6. The formula used to determine the COA defuzzification method is:

$$COA(A) = \frac{\int_{x_{min}}^{x_{max}} \mu_A(x) \times x dx}{\int_{x_{min}}^{x_{max}} \mu_A(x) dx} \tag{6.5}$$

where $\mu_A(x)$ represents weight for value x (the value of the linguistic variable), and x_{min} and x_{max} represent the range of the linguistic variable.

Choosing the proper method is paramount as it can affect the accuracy of the model. In this model, the mean of max defuzzification method was selected due to its ability to provide accurate results with a high level of acceptance.

6.8. Results

In this section, the results of the average surface roughness and percentage of surface roughness reduction which were predicted by the fuzzy logic model were as shown in Figure 6.7 and Figure 6.8, respectively. Figure 6.7 (a) shows the variation of the average surface roughness (Ra) predicted by the fuzzy logic model with respect to the variation of applied voltage and particle size. The results show that Ra decreases with increasing of the applied voltage, and the best average surface roughness can be obtained by using low applied voltage (20 V) with medium particle size (70-80 µm).

Figure 6.7 (b) demonstrates that the predicted value of Ra varies with applied voltage and time, and it increases with the decreasing of the applied voltage. The best combination of the applied voltage and operating time which can produce a best Ra is the low value of applied voltage (20 V) and the middle value of the operating time (30-40 min). The variation of Ra with respect to the applied voltage and frequency of energizing the electromagnets was as illustrated in Figure 6.7 (c) and it was obvious that the best Ra can be achieved with the low value of applied voltage (20 V) and the middle value of frequency (6-8 Hz).

Otherwise, the variation of the predicted value of the reduction percentage of the surface roughness (%RS) with respect to the input parameters (applied voltage, frequency, operating time, and particle size) was as illustrated in Figure 6.8. Here it was seen that %RS increases with the increasing of the applied voltage, operating time, and particle size however, it decreases with the increasing of frequency. The best value of %RS can be obtained with the highest value of voltage (30 V), long operating time (60 min), large particle size (100 µm), and low frequency (2 Hz).

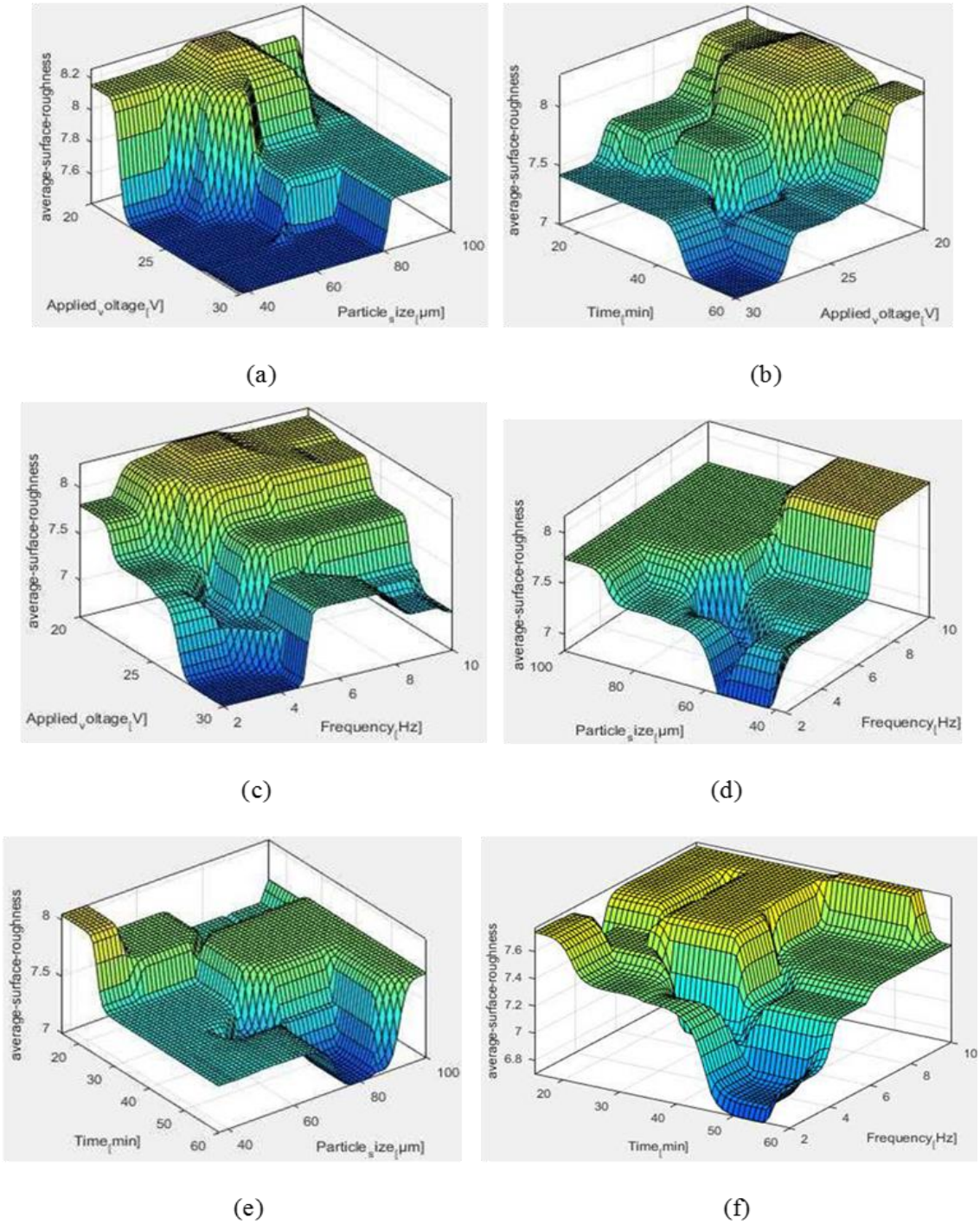

Figure 6. 7: Predicted average surface roughness by fuzzy logic with respect to parameters changing (a) applied voltage and particle size, (b) applied voltage and time, (c) applied voltage and frequency, (d) particle size and frequency, (e) time and particle size, (f) time and frequency.

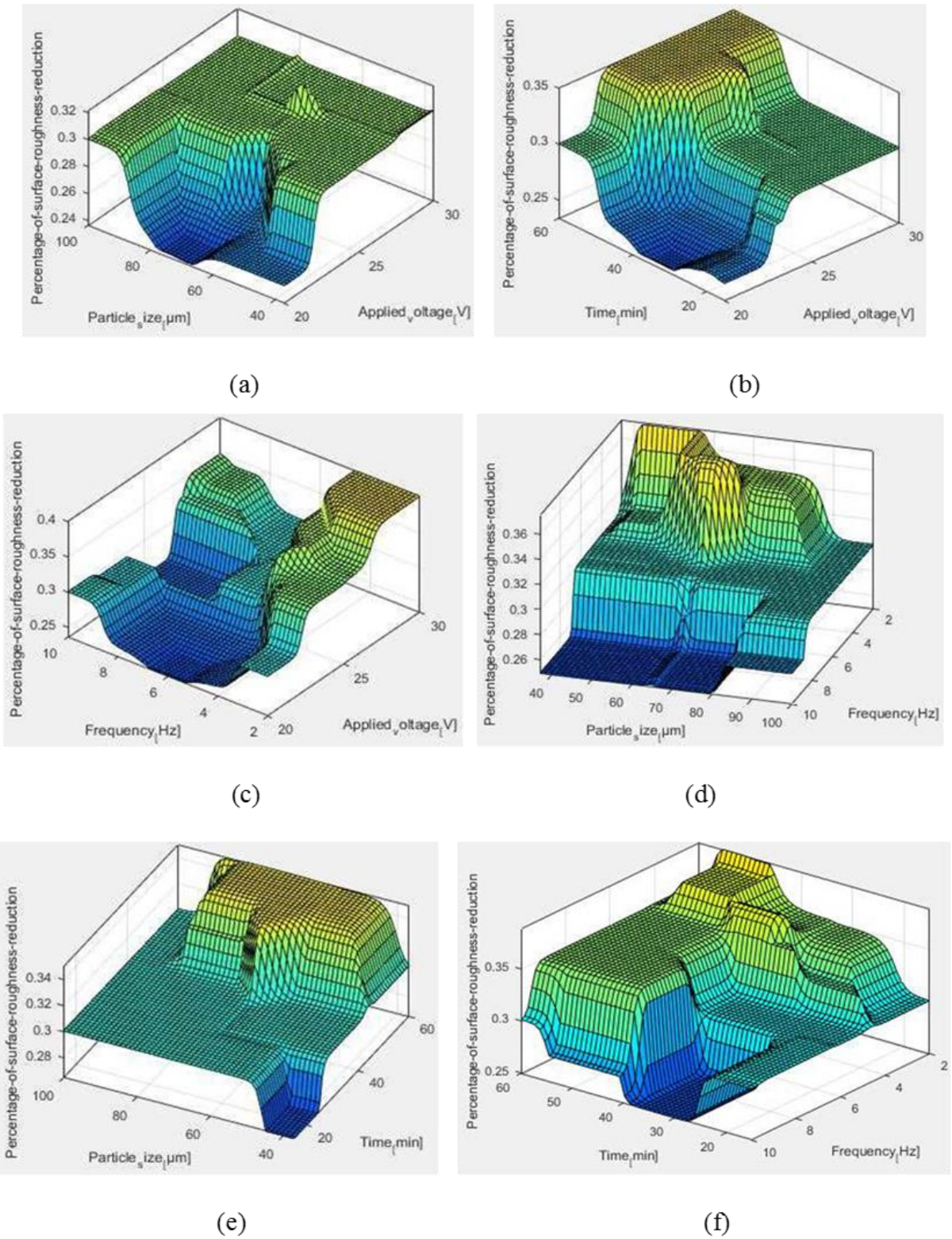

Figure 6. 8: Predicted reduction percentage of surface roughness by fuzzy logic with respect to parameter changing (a) applied voltage and particle size, (b) applied voltage and time, (c) applied voltage and frequency, (d) particle size and frequency, (e) time and particle size, (f) time and frequency.

6.9. Fuzzy logic Model Accuracy and Error

The accuracy and error rate of the developed predicted fuzzy model must be examined. To do so, the experimental results of Taguchi L9 OA were compared with the results of the predicted model under the same conditions. The Ra and %RS values, which were determined experimentally based on the design of experiments approach using Taguchi L9 OA, were compared with the predicted values obtained from the proposed fuzzy logic model for the same corresponding conditions. Table 6.10 shows the experimental conditions of the input parameters according to Taguchi L9 OA, the output findings obtained experimentally and predictively, and the error percentage along with the accuracy of the predicted model.

Table 6.10: Accuracy and error percentage of the fuzzy logic prediction model according to L9 Taguchi OA

Exp.#	Input Parameters				Output Parameters							
	Applied Voltage	Freq.	Time	Particle Size	Ra				%RS			
					Measu.	Pred.	Error	Accy.	Measu.	Pred.	Error	Accy.
1	20	2	15	100	8.1624	7.8916	0.0328	96.34%	29%	29%	0	96%
2	20	6	30	75	8.5327	7.9833	0.0640	94.15%	25%	27%	0.07	89%
3	20	10	60	37	8.1158	7.9166	0.0238	97.06%	33%	29%	0.13	87%
4	25	2	30	37	7.6306	7.3916	0.0312	96.89%	36%	31%	0.14	86%
5	25	6	60	100	7.6897	7.605	0.0097	98.54%	36.6%	31%	0.17	83%
6	25	10	15	75	7.8502	7.726	0.0157	98.72%	28%	28%	0	92%
7	30	2	60	75	6.2171	7.033	0.1325	87.15%	49.6%	35%	29	71%
8	30	6	15	37	8.1030	7.583	0.0637	93.64%	36.6%	30%	19	81%
9	30	10	30	100	7.5434	7.55	0.0013	96.91%	39%	30%	24	77%
Overall Error and Accuracy							0.0565	95%			0.136	84.95%

The variation between the experimental and predicted values, which represents the error percentage, *Er*, was determined by using eq. (6.6).

$$Er = \frac{|x_m - x_p|}{x_m} \times 100\% \tag{6.6}$$

where x_m denotes the measured value, and x_p denotes the predicted. Similarly, accuracy of the model, Ac, was obtained using eq. (6.7) in which *N* denotes the number of the datasets trialed.

$$Ac = \frac{1}{N}\sum_{i=1}^{n}\left(1 - \frac{|x_m - x_p|}{x_m}\right) \times 100\% \tag{6.7}$$

The overall accuracy and error percentage were obtained using the root-mean-square average (RMS Average), which represents the square root of the arithmetic mean of the squares of the data, as illustrated in eq. (6.8).

$$RMS\ Average = \sqrt{\frac{1}{N}\sum_{i=1}^{N} x_i^2} \tag{6.8}$$

Thus, the error percentage and model accuracy were obtained using the measured and predicted values of Ra and %RS. The results demonstrated that the average percentage error and accuracy for Ra were 5.65% and 95%, respectively. The small error indicated that the proposed predicted fuzzy model could be used to predict the Ra for the SMAF process and the results could be trusted. Further, the average percentage error and accuracy for %RS were 13.6% and 84.95%, respectively. In spite of the results of %RS not being as accurate as the results of Ra, they are still acceptable. This deviation of %RS could possibly have been caused by a combination of both measurement error and the indefiniteness of fuzzy model parameters. Or using a triangular (linear) membership function to represent the output parameters may not be appropriate.

6.10. Parametric Effects

The results of the proposed fuzzy logic model could also be used to clarify the effects of process input parameters on the output parameters individually. In this section, the experimental results shown in Figure (6.7 and 6.8) are used to investigate the influence of the input parameters (applied voltage, frequency, operating time, and particle size) on the output parameters (average surface roughness and reduction percentage of surface roughness), and generally to evaluate the finishing process performance.

6.10.1. Applied Voltage

The experimental results of using SMAF showed that as the applied voltage changed from a lower to higher value, the average surface roughness improved, effectively. This outcome was confirmed previously in the literature and implies increasing of the magnetic force in the working zone. Thus, the higher the applied voltage, the lower Ra was. Similarly, applied voltage had a significant effect on the reduction percentage of the surface roughness. Increasing the applied voltage led to increasing the %RS due to increasing of the difference between the initial and final values of the surface roughness.

6.10.2. Frequency of electromagnet energizing

The frequency of energizing the electromagnet, as an input parameter, had an impact on the output parameters, Ra and %RS. To achieve a better understanding of the impact of this parameter, the relationship between the frequency of energizing and velocity of the abrasive particles needed to be clarified. The frequency of energizing the electromagnet represented the frequency of the magnetic field rotation, which was produced due to the frequent activation of the electromagnets. Consequently it represented the rotating frequency of the magnetic abrasive particles, and rather, it was considered to be the velocity of the abrasive particles.

In SMAF, the movement of the magnetic abrasive particles is in the XY-Plane. Thus, it can be assumed that the initial position (at $t = 0$) of a particle located at the X-axis with radius r_i from the center is (r_i, 0). Therefore, position of the rotating particle at any time would be [84]:

$$X = r_i \cos(\omega t) \tag{6.9}$$

$$Y = r_i \sin(\omega t) \tag{6.10}$$

where r_i is the distance between the particle and the center point, ω is the angular velocity of the particle, and t represents time. To determine the particle velocity in the X-direction $v_x\,(t)$, and Y-direction $v_y\,(t)$, equations (9) and (10) should be differentiated with respect to the time t.

$$v_x(t) = \frac{dX}{dt} = -r_i\,\omega \sin(\omega t) \tag{6.11}$$

$$v_y(t) = \frac{dY}{dt} = -r_i\ \omega co\ s(\omega t) \tag{6.12}$$

Therefore, the resultant velocity *v (t)*, as a function of *t* can be expressed as:

$$v(t) = \sqrt{(v_x(t))^2 + (v_y(t))^2} = r_i\ \omega \tag{6.13}$$

Also, it is well-known in basic physics that the relationship between frequency f and angular velocity ω is:

$$\omega = 2\pi f \tag{6.14}$$

This means frequency affects the velocity of the magnetic abrasive particles. Accordingly, it had an impact on the average surface roughness and reduction percentage of the surface roughness. It is observable in Figures (6.7 and 6.8) that increasing frequency leads to decreasing the surface improvement. The reason behind this was low frequency values help the portion of abrasive particles to form a uniform flexible magnetic abrasive brush moving in the same pattern on the surface of the workpiece. This promoted, in terms of energy conservation, the maintaining of particle energies to perform the finishing process.

Otherwise, high frequency values should provide, theoretically, an additional energy to the particles. However, in the current case, increasing frequency would affect the magnetization factor of the ferromagnetic particles and prevent their uniformity. Consequently, the flexible magnetic abrasive brush needs to be nonuniform and the particles need to move irregularly on the workpiece surface. This affected the performance of the finishing process negatively, and this could be recognized in the experimental results of Ra and %RS.

6.10.3. Operating Time

The operating time had a significant impact in producing a desirable finished surface. According to the fuzzy logic predicted model, increasing the operating time helped to improve the quality of the finished surface. Figures (6.7 and 6.8) illustrate that the average surface roughness improved with the increasing of the machining time. Similarly, the reduction percentage of the surface roughness also increased with the increasing of the machining time. This meant that the difference between the initial value of the surface roughness and the final value was increasing, and was due to the fact that in this finishing method, longer operating time meant more material being removed. Hence, the workpiece surface improved and a precise final surface could be achieved.

6.10.4. Particle Size

The relationship between the size of abrasive particles and the final surface characteristics can be clarified using the fuzzy logic predicted model. Generally, larger particle size affects the value of average surface roughness negatively, while the smaller one tends to produce a better surface and improve the average surface roughness, as shown in Figures (6.7 and 6.8). This was due to the fact that increasing the particle size meant increasing the magnetic pressure. This led to increasing of the penetration of the particle into the workpiece surface. Accordingly, the depth of cut would be increased as well as produce wider scratch grooves on the surface of the workpiece. In this case, the metal removal rate might be increased, but the profile of the workpiece surface showed more irregularities and greater non-uniformity.

6.11. Conclusions

The main target of this study was to develop a fuzzy logic model for predicting the output parameters of the SMAF process based on experimental results. A fuzzy logic model using 25 fuzzy rules was developed to predict the average surface roughness and the reduction percentage of the surface roughness for a given input set of applied voltage, frequency-of-energizing the electromagnet, operating time, and size of abrasive particles. Taguchi L9 orthogonal array was chosen for designing the experiments with four input parameters and three levels, while Taguchi L25 orthogonal array was used to build the fuzzy logic predicted model with four input parameters and five levels.

The experiments were conducted using Al-6061-T6 alloy samples. To accurately obtain the surface roughness measurement, a Laser Scanning Confocal Microscope was used to measure the surface roughness of the samples before and after the SMAF finishing process and obtain Ra values. The proposed fuzzy model was able to predict the output parameters (Ra, and %RS). To verify the model performance, the predicted values obtained from the fuzzy model as output values were compared with the experimental results of the corresponding input values. The data of the experiments was in good agreement with the predicted results. The accuracy of the predicted model for the computed and experimental results were shown as 95% for Ra, and 84.95% for % RS.

Chapter 7

Implementations of SMAF Technique

7.1. Introduction

The proposed technique needs to be tested to examine its validation in dealing with different materials and different geometries. For this reason, the SMAF technique has been applied to accomplish the surface finishing process for a thin film material, a ceramic based composite material, the internal surface of an aluminum tube, tiny channels, and a flat slab of Titanium and Inconel, samples.

7.2. Thin Film Material

Recently, many industrial and engineering applications, such as micro-system and micro- electronic technologies, utilize thin film metal structures in order to improve their performance and increase their efficiency. A thin film material can be defined as a metal layer with a thickness that does not exceed a few micrometers [85]. Production and implementation of thin film materials requires, for some applications, machining or finishing operations. Machining of these tiny structures can be considered an essential challenge. The production of thin solar panels, for example, requires a finishing process prior to the assembly operation. Magnetic abrasive finishing is usually used for this kind of finishing process [86]. As a potential application of the developed system, the SMAF technique was used to modify the surface roughness of a sheet of aluminum foil, an example of a thin film material, shown in Figure 7.1.

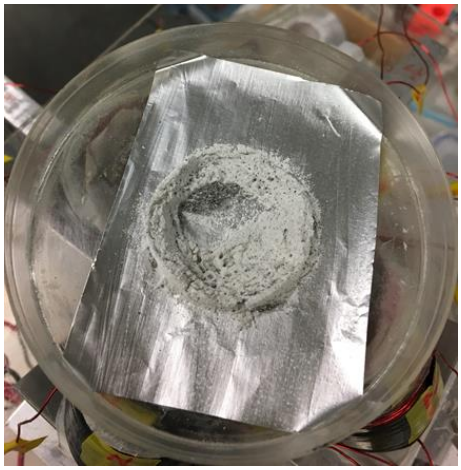

Figure 7. 1: Applying SMAF to modify the surface roughness of aluminum foil.

The results show that this technique was able to be used for this kind of material. The surface roughness of the aluminum sheet was improved by 32%. As illustrated in Figure 7.2, the average surface roughness before the finishing process was 1.41 µm, and it is improved to 0.96 µm after the process. The finishing conditions were, 20 V for the applied voltage, 2 Hz for the frequency, 60 min for the operating time, and the particle size was 37 µm.

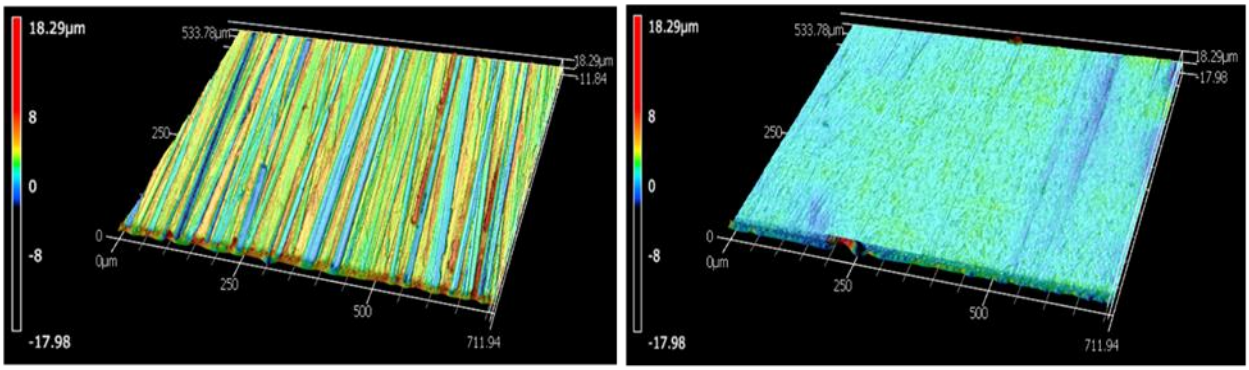

(a) (b)

Figure 7. 2: 3D photographs of finished surface of aluminum foil (a) before and (b) after finishing process.

7.3. Composite Material

Many industrial applications use composite materials due to their superior characteristics, such as high-strength, wear resistance, stability of mechanical properties at high-temperatures, and low cost. However, most composite materials are considered to have high hardness resulting in their difficult machining [87]. Thus they require nonconventional precision machining techniques. Polycrystalline samples of lanthanum modified bismuth titanate ceramics with composition $Bi_{3\cdot25}La_{0\cdot75}Ti_3O_{12}$ (BLT) are representative of these class of materials, shown in Figure 7.3.

Figure 7. 3: Applying SMAF to modify the surface roughness of BLT slab.

This ceramic material (BLT) is used by a research team at the University of Waterloo to develop a two-way mm-wave phased array antenna system. The BLT slab dimensions must be about 1 mm × 3 mm × 0.25 mm [88]. Due to some design and fabrication limitations, the surface roughness of the BLT slab needs to be improved without causing any damage to the surface or subsurface of the sample. The SMAF technique was used and it was able to improve the surface roughness from 37.52 nm (before the process) to 28.90 nm (after the process), as illustrated in Figure 7.4. The finishing conditions were, 20 V for the applied voltage, 2 Hz for the frequency, 60 min for the operating time, and the particle size was 37 µm.

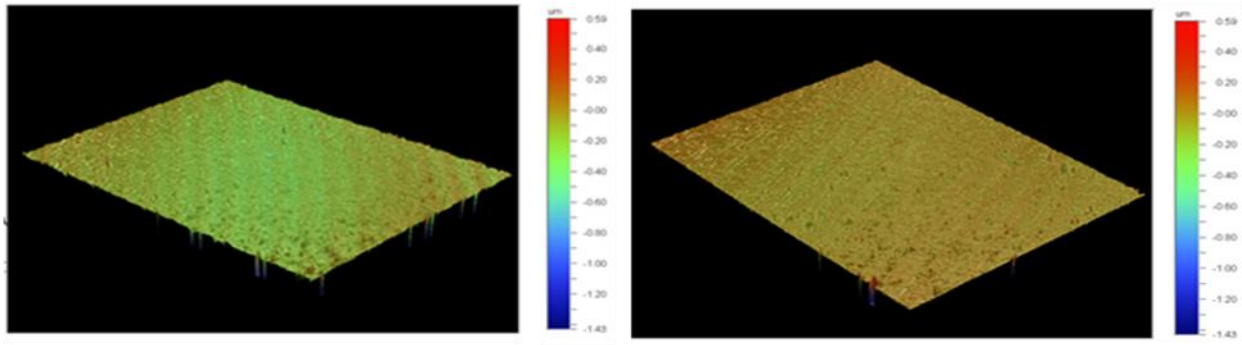

(a) (b)

Figure 7. 4: 3D photographs of finished surface of BLT slab (a) before and (b) after finishing process.

7.4. Internal Surface of a Thin Tube

Finishing the internal surface of a thin tube can be considered a challenging task due to it having a hard-to-reach area. Fuel pipes and high pressure liquid pipes are examples of the components which have internal surfaces that need to be improved [89]. Using nonconventional finishing processes, such as magnetic abrasive finishing, could be the best choice to accomplish this task. In order to test the ability of the SMAF technique to deal with such aspects, it was applied to finish the internal surface of an aluminum pipe with a diameter of 10 mm, as shown in Figure 7.5. The finishing conditions were, 20 V for the applied voltage, 2 Hz for the frequency, 60 min for the operating time, and the particle size was 75 µm.

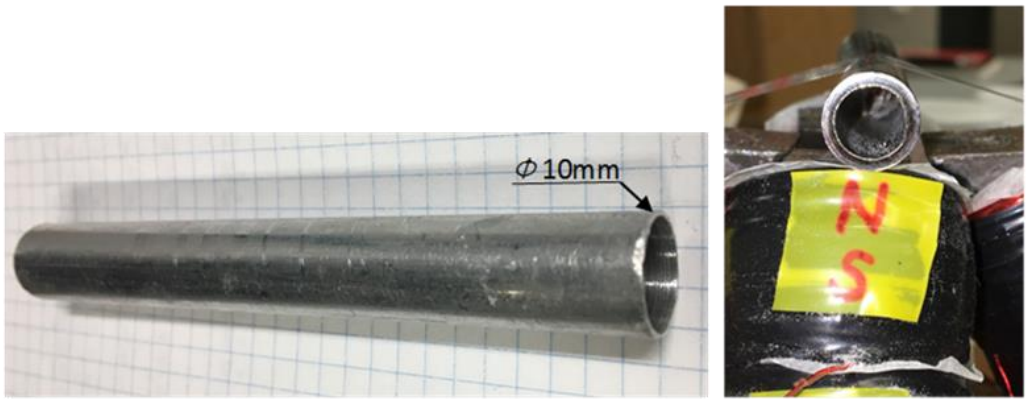

Figure 7. 5: Applying SMAF to modify the surface roughness of an aluminum tube.

The results show that the internal surface roughness was improved by 43%. The average surface roughness before the finishing process was 2.8 µm and it is improved to 1.6 µm after the process, as illustrated in Figure 7.6.

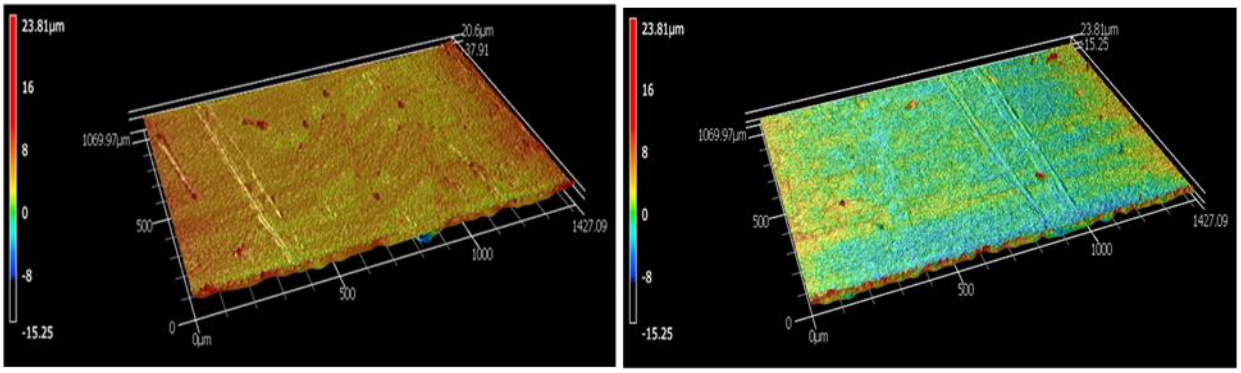

Figure 7. 6: 3D photographs of the internal finished surface of aluminum tube (a) before and (b) after finishing process.

7.5. Tiny Channels

Surface finish processing for a tiny channel can be described as a difficult and complicated process in terms of the mechanism and cost. Micro-total analysis systems (micro-TAS) chips for medical implementations [90] and Fresnel lenses for PV systems [91], are examples of the applications that need to produce tiny channels with high accuracy surface roughness. To examine the ability of the SMAF technique to accommodate the tiny channels, this technique was applied to finish a surface of 2 mm × 2 mm U-shaped groove of an aluminum slab, illustrated in Figure 7.7.

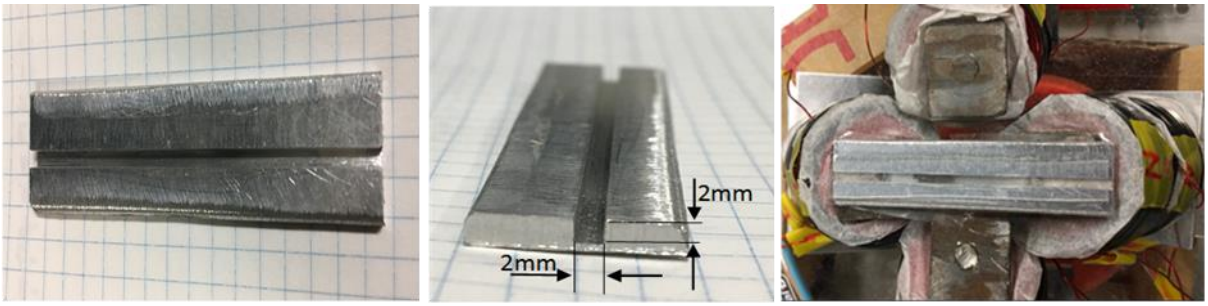

Figure 7. 7: Applying SMAF to modify the surface roughness of an aluminum U-shaped groove.

The results show that the surface roughness of the U-shaped groove was improved by 40%. The average surface roughness before the finishing process was 5.67 µm and it is improved to 3.41 µm after the process, as illustrated in Figure 7.8.

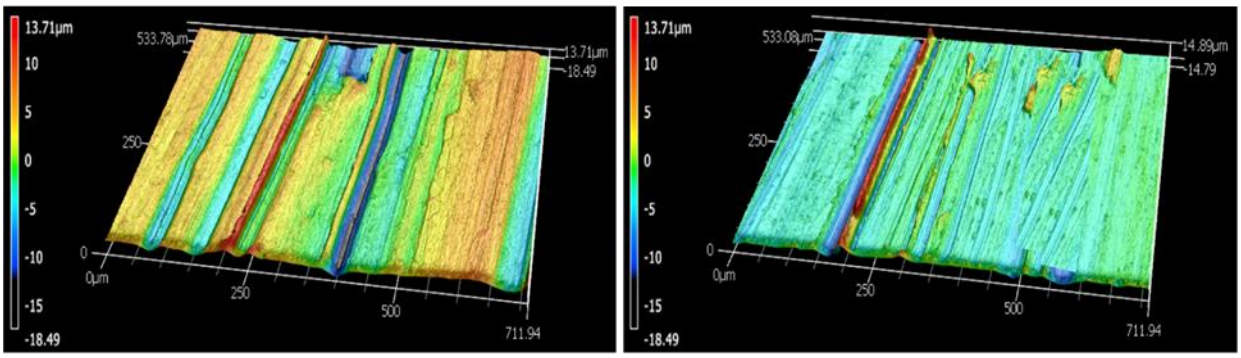

Figure 7. 8: 3D photographs of the finished surface of aluminum U-shaped groove (a) before and (b) after finishing process.

7.6. Special Materials

Some materials which are described as “hard-to-machine” materials due to their extreme toughness and work hardening characteristic, such as Titanium and Inconel, were also subjected to a surface finishing process using the SMAF technique.

7.6.1. Titanium

Figure 7.9 shows the Titanium sample during the surface finishing process using the SMAF method. The finishing conditions were 20 V for the applied voltage, 2 Hz for the frequency, and 60 min for the operating time. For the abrasive particle size, two kinds of aluminum oxide were used, 100 µm in the first 30 min, and then 75 µm in the second 30 min.

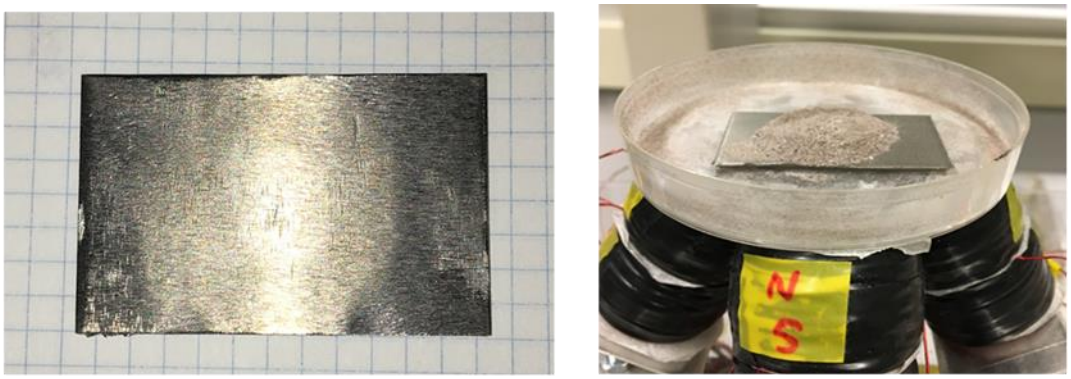

Figure 7. 9: Applying SMAF to modify the surface roughness of Titanium sample.

The results show that the surface roughness of the Titanium sample was improved by 53%. The average surface roughness before the finishing process was 4.156 µm and it was improved to 1.94 µm after the process, as illustrated in Figure 7.10.

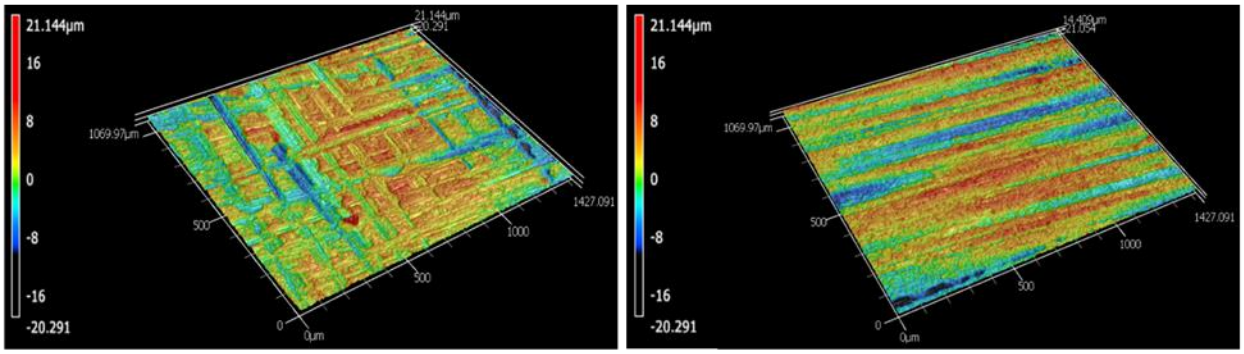

(a) (b)

Figure 7. 10: 3D photographs of the finished surface of Titanium sample (a) before and (b) after finishing process.

7.6.2. Inconel

Figure 7.11 shows 3D photographs of the finished surface of the Inconel sample after applying the SMAF method. The results show that the surface roughness of the Inconel sample was improved by 61%. The average surface roughness before the finishing process was 34 µm and it was improved to 13 µm after the process. The finishing conditions were 20 V for the applied voltage, 2 Hz the frequency, and 90 min for the operating time. For the abrasive particle size, two kinds of aluminum oxide were used, 100 µm in the first 45 min and then 75 µm in the second 45 min.

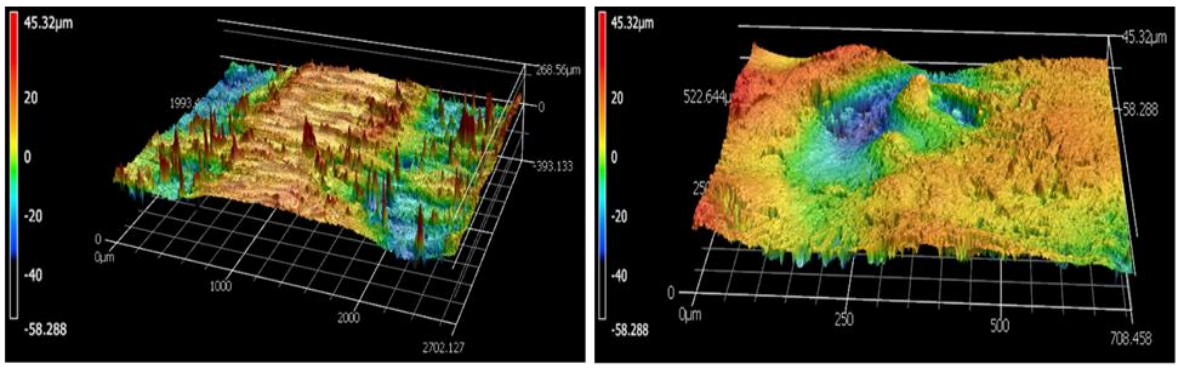

(a) (b)

Figure 7. 11: 3D photographs of the finished surface of Inconel sample (a) before and (b) after finishing process.

7.7. Conclusion

To examine the performance of the proposed technique, SMAF was applied to perform the finishing process for different materials, and different shapes and geometries. First, SMAF was tested to finish a thin film sheet of aluminum foil where it was able to improve the surface roughness by32%. The average surface roughness before the finishing process was 1.41 µm, and it was improved to 0.96 µm after the process.

Further, the SMAF technique was applied to improve the surface roughness of a composite material sample of BLT slab where it was able to improve the surface roughness from 37.52 nm (before the process) to 28.90 nm (after the process).

Moreover, the proposed finishing method was applied to finish an internal surface of 10 mm diameter aluminum tube where the experimental results showed that the internal surface roughness was improved by 43%. The average surface roughness before the finishing process was 2.8 µm and it was improved to 1.6 µm after the process.

Also, SMAF was tested to treat a U-shaped 2 mm × 2 mm tiny channel of an aluminum slab. The results showed that the surface roughness of the U-shaped groove was improved by 40%. The average surface roughness before the finishing process was 5.67 µm and it was improved to 3.41 µm after the process.

Additionally, the proposed technique was applied to perform a surface finishing process for "hard-to-machine" materials, Titanium and Inconel. The results show that the surface roughness of the Titanium sample was improved by 53%. The average surface roughness before the finishing process was 4.156 µm and it was improved to1.94 µm after the process. Whereas, for the Inconel sample the improvement was about 61%. The average surface roughness before the finishing process was 34 µm and it was improved to 13 µm after the process.

Based on the obtained experimental results, the SMAF technique was able to deal efficiently with different kinds of materials as well as complicated shapes and geometries.

Chapter 8

Conclusions and Future Work

8.1. Thesis Conclusions

In this thesis, a stationary apparatus of magnetic abrasive finishing was designed, fabricated and successfully tested. The proposed finishing system using a rotary magnetic field, with stationary electromagnets and workpiece. The mechanism of producing a rotary magnetic field is based on manipulating the electromagnets' excitation current has also been explained. This approach eliminates any mechanical motion of the electromagnets and the workpiece, to make the system more controllable and reliable.

The four-coil configuration aligned by 30̊ with the Z-axis was the best choice to carry out the experiments. The best configuration was the one that could make the component of the magnetic field, *B*, in the tangential direction, B_{xy}, greater than the component in the normal direction, B_z. Thus, the tangential magnetic force component, F_{mt}, was greater than the normal force component, F_{mz}. This was important in order to make the particles on the workpiece surface move tangentially according to the rotation of the magnetic field and accomplish the finishing process.

In the current study, electromagnet optimal design was investigated to maximize the finishing force in the working area. A parametric study was carried out to optimize the geometry of the electromagnet using a finite element simulation. The electromagnet volume was fixed as *50* cm^3 due to some technical limitations regarding to the power supply and L298 Dual Full-Bridge Drive capacities. The optimum coil parameters were found to be (α=3 and β=2.5) and the Fabry factor (Geometry factor) was G=0.175. Coil length was *l* = 2.5 cm and the iron core length *lc* = 3.5 cm with outer and inner diameter of 1.5 cm and 0.5 cm, respectively.

A new approach was conducted to measure the magnetic force experimentally using an ATI force sensor. The results were verified using a finite element simulation with percentage error of 3.5%.

The variation of temperature in the interfering zone between the workpiece (Titanium specimen) and the magnetic abrasive particles was also measured to observe the temperature increase during the finishing process. Thermal camera was used and the measurements showed that the variation during the operation

running time (60 mins) was just 14˚C, (23 – 37˚C). This change would have an insignificant effect on the surface characteristics and quality.

A fuzzy logic model was developed to predict the output parameters of the SMAF process based on experimental results. The fuzzy model using 25 fuzzy rules was developed to predict the average surface roughness and the reduction percentage of the surface roughness for a given input set of applied voltage, frequency-of-energizing of the electromagnet, operating time, and size of abrasive particles. The Taguchi orthogonal array technique was chosen for designing the experiments to build the fuzzy logic predicted model with four input parameters and five levels. The experiments were conducted using Al-6061-T6 samples. To accurately obtain the surface roughness measurement, a Laser Scanning Confocal Microscope was used to measure the surface roughness of the samples before and after the SMAF finishing process and obtain Ra values. The proposed fuzzy model was able to predict the output parameters (Ra, and %RS). To verify the model performance, the predicted values obtained from the fuzzy model as output values were compared with the experimental results of the corresponding input values. The data of the experiments was in good agreement with the predicted results. The accuracy of the predicted model for the computed and experimental results were shown as 95% for Ra, and 84.95% for % RS.

To examine the performance of the proposed technique, SMAF was applied to perform the finishing process for different materials, and different shapes and geometries. First, SMAF was tested to finish a thin film sheet of aluminum foil where it was able to improve the surface roughness by 32%. Then, SMAF was applied to improve the surface roughness of a composite material sample of BLT slab where it was able to improve the surface roughness by 23%. Also, the proposed finishing method was applied to finish an internal surface of 10 mm diameter aluminum tube where the experimental results showed that the internal surface roughness was improved by 43%.

Further, SMAF was tested to treat a U-shaped 2 mm × 2 mm tiny channel of an aluminum slab. The results showed that the surface roughness of the U-shaped groove was improved by 40%. Additionally, the proposed technique was used to perform a surface finishing process for “hard-to-machine” materials, Titanium and Inconel. The results showed that the surface roughness of the Titanium sample was improved by 53% and the Inconel approximately 61%. Based on the obtained experimental results, the SMAF technique was able to deal efficiently with different kinds of materials as well as complicated shapes and geometries.

8.2. Future research

The developed SMAF technique has already shown its capability in achieving a good surface finishing for different applications. However, a number of future work items have been identified related to the proposed method in order to achieve a further potential improvement, as follows:

- Magnetorheological fluid can be incorporated in the present SMAF process which can help to improve the finished surface quality, and hence better surface texture can be expected.
- The current case represents a small-scale model. A large-scale model is necessary to study, in order to obtain better results and attempt to apply this technique on different applications.
- It is further recommended to study the combination effect of the magnetic particles with the abrasive particles. In this study, just iron particles with an average diameter of 120 μm was used with three different particle sizes of aluminum oxide; 37, 75, and 100 μm.
- Also, to obtain a better understanding of the effect of the magnetic abrasive particles on the finished surface, it is recommended to use different kinds of abrasive particles such as silicon carbide, boron nitride, and diamond, in addition to aluminum oxide.

References

[1] Li, W., Li, X., Yang, S. and Li, W., 2018. A newly developed media for magnetic abrasive finishing process: Material removal behavior and finishing performance. *Journal of Materials Processing Technology*, *260*, pp.20-29.

[2] S. Dhull, Harwider, and R.S. Walia, Jan. 2016. Experimental study of process parameters for magnetic assisted AFM incorporating the drill bit helical flow effect. *International Journal of Research (IJR),* vol. 3, no. 1, pp. 676-684.

[3] Yamaguchi, H., Srivastava, A.K., Tan, M.A., Riveros, R.E. and Hashimoto, F., 2012. Magnetic abrasive finishing of cutting tools for machining of titanium alloys. *CIRP Annals-Manufacturing Technology*, *61*(1), pp.311-314.

[4] Wu, J., Zou, Y. and Sugiyama, H., 2016. Study on finishing characteristics of magnetic abrasive finishing process using low-frequency alternating magnetic field. *The International Journal of Advanced Manufacturing Technology*, *85*(1-4), pp.585-594.

[5] V.K. Jain. "Micro manufacturing process". CRCpress, Taylor & Francis Group. 2013.

[6] Zou, Y., 2012. Internal finishing of micro tubes by the magnetic abrasive finishing. *J Jpn Soc Abras Technol*, *56*(2), pp.86-89.

[7] Kang, J., 2012. *Development of high-speed internal finishing and cleaning of flexible capillary tubes by magnetic abrasive finishing* (Doctoral dissertation, University of Florida).

[8] Gietzelt, T. and Eichhorn, L., 2012. Mechanical micromachining by drilling, milling and slotting. In *Micromachining Techniques for Fabrication of Micro and Nano Structures*. InTech.

[9] Hashimoto, F., Yamaguchi, H., Krajnik, P., Wegener, K., Chaudhari, R., Hoffmeister, H.W. and Kuster, F., 2016. Abrasive fine-finishing technology. *CIRP Annals*, *65*(2), pp.597-620.

[10] Japan Society for Abrasive Technology, 1995. Sessaku Kensaku Kenma Yogo Jiten, [*Dictionary of Cutting, Grinding, and Polishing*]. Kogyo Chosakai Publishing, Tokyo. (in Japanese).

[11] Marinescu, I.D., Rowe, W.B. and Dimitrov, B., 2012. *Tribology of abrasive machining processes*. William Andrew.

[12] Klocke, F., 2003, November. Modelling and simulation of grinding processes. In *1st European conference on Grinding*.

[13] V.K.Jain., 2002. "Advanced Machining Processes". New Delhi: Allied Publishers.

[14] Jayswal, S.C., Jain, V.K., and Dixit, P.M., 2005. Modeling and simulation of magnetic abrasive finishing process. *International Journal of Advanced Manufacturing Technology*. Vol. 26: pp.477–490.

[15] Jain, N.K. and Jain, V.K., 2001. Modeling of material removal in mechanical type advanced machining processes: a state-of-art review. *International Journal of Machine Tools and Manufacture*, *41*(11), pp.1573-1635.

[16] American National Standard Institute (ANSI), 1985. Surface Texture (Surface Roughness, Waviness, and Lay) B46. 1. *American Society of Mechanical Engineers, New York*, p. 43.

[17] Tseng, T.L.B., Konada, U. and Kwon, Y.J., 2016. A novel approach to predict surface roughness in machining operations using fuzzy set theory. *Journal of Computational Design and Engineering*, *3*(1), pp.1-13.

[18] Jain, V.K., 2008. Abrasive-based nano-finishing techniques: an overview. *Machining Science and Technology*, *12*(3), pp.257-294.

[19] Shinmura, T., Takazawa, K. and Hatano, E., 1985. Study on Magnetic-Abrasive Process. Application to Plane Finishing. *Bull. Jpn. Soc. Precis. Eng.*, *19*(4), pp.289-291.

[20] Shinmura, T. and Aizawa, T., 1989. Study on magnetic abrasive finishing process (Development of plane finishing apparatus using a stationary type electromagnet). *Bulletin of the Japan Society of Precision Engineering*, *23*(3), pp.236-239.

[21] Shinmura, T. and Yamaguchi, H., 1995. Study on a new internal finishing process by the application of magnetic abrasive machining: internal finishing of stainless steel tube and clean gas bomb. *JSME international journal. Ser. C, Dynamics, control, robotics, design and manufacturing*, *38*(4), pp.798-804.

[22] Yamaguchi, H. and Shinmura, T., 2000. Study of an internal magnetic abrasive finishing using a pole rotation system: Discussion of the characteristic abrasive behavior. *Precision Engineering*, *24*(3), pp.237-244.

[23] Yamaguchi, H. and Shinmura, T., 2004. Internal finishing process for alumina ceramic components by a magnetic field assisted finishing process. *Precision Engineering*, *28*(2), pp.135-142.

[24] Mori, T., Hirota, K. and Kawashima, Y., 2003. Clarification of magnetic abrasive finishing mechanism. *Journal of Materials Processing Technology*, *143*, pp.682-686.

[25] Wang, Y. and Hu, D., 2005. Study on the inner surface finishing of tubing by magnetic abrasive finishing. *International Journal of Machine Tools and Manufacture*, *45*(1), pp.43-49.

[26] Yamaguchi, H., Shinmura, T. and Sekine, M., 2005. Uniform internal finishing of SUS304 stainless steel bent tube using a magnetic abrasive finishing process. *Journal of manufacturing Science and Engineering*, *127*(3), pp.605-611.

[27] Yamaguchi, H., Shinmura, T. and Ikeda, R., 2007. Study of internal finishing of austenitic stainless steel capillary tubes by magnetic abrasive finishing. *Journal of Manufacturing Science and Engineering*, *129*(5), pp.885-892.

[28] Lin, C.T., Yang, L.D. and Chow, H.M., 2007. Study of magnetic abrasive finishing in free-form surface operations using the Taguchi method. *The International Journal of Advanced Manufacturing Technology*, *34*(1-2), pp.122-130.

[29] Yamaguchi, H. and Hanada, K., 2008. Development of spherical magnetic abrasive made by plasma spray. *Journal of Manufacturing Science and Engineering*, *130*(3), p.031107.

[30] Kwak, J.S., 2009. Enhanced magnetic abrasive polishing of non-ferrous metals utilizing a permanent magnet. *International Journal of Machine Tools and Manufacture*, *49*(7-8), pp.613-618.

[31] Kang, J., George, A. and Yamaguchi, H., 2012. High-speed internal finishing of capillary tubes by magnetic abrasive finishing. *Procedia CIRP*, *1*, pp.414-418.

[32] Kurobe, T. and Imanaka, O., 1984. Magnetic field-assisted fine finishing. *Precision Engineering*, *6*(3), pp.119-124.

[33] Yamaguchi, H. and Shinmura, T., 1999. Study of the surface modification resulting from an internal magnetic abrasive finishing process. *Wear*, *225*, pp.246-255.

[34] Jain, V.K., Kumar, P., Behera, P.K. and Jayswal, S.C., 2001. Effect of working gap and circumferential speed on the performance of magnetic abrasive finishing process. *Wear*, *250*(1-12), pp.384-390.

[35] Chang, G.W., Yan, B.H. and Hsu, R.T., 2002. Study on cylindrical magnetic abrasive finishing using unbonded magnetic abrasives. *International Journal of Machine Tools and Manufacture*, *42*(5), pp.575-583.

[36] Singh, D.K., Jain, V.K. and Raghuram, V., 2004. Parametric study of magnetic abrasive finishing process. *Journal of materials processing technology*, *149*(1-3), pp.22-29.

[37] Yin, S. and Shinmura, T., 2004. Vertical vibration-assisted magnetic abrasive finishing and deburring for magnesium alloy. *International Journal of Machine Tools and Manufacture*, *44*(12-13), pp.1297-1303.

[38] Jha, S. and Jain, V.K., 2004. Design and development of the magnetorheological abrasive flow finishing (MRAFF) process. *International Journal of Machine Tools and Manufacture*, *44*(10), pp.1019-1029.

[39] Singh, D.K., Jain, V.K., Raghuram, V. and Komanduri, R., 2005. Analysis of surface texture generated by a flexible magnetic abrasive brush. *Wear*, *259*(7-12), pp.1254-1261.

[40] Singh, D.K., Jain, V.K. and Raghuram, V., 2006. Experimental investigations into forces acting during a magnetic abrasive finishing process. *The International Journal of Advanced Manufacturing Technology*, *30*(7-8), pp.652-662.

[41] Girma, B., Joshi, S.S., Raghuram, M.V.G.S. and Balasubramaniam, R., 2006. An experimental analysis of magnetic abrasives finishing of plane surfaces. *Machining science and Technology*, *10*(3), pp.323-340.

[42] Shinmura, T., Hatano, E. and Takazawa, K., 1986. The development of magnetic-abrasive finishing and its equipment by applying a rotating magnetic field. *Bulletin of JSME*, *29*(258), pp.4437-4443.

[43] Shinmura, T., 1992. A new internal finishing process of a non-ferromagnetic tubing by applying a rotating magnetic field. *Int. J. JSPE*, *26*(4), p.302.

[44] Storr, W. (n.d.). Basic Electronics Tutorials. [Online], from http://www.electronicstutorials.ws/electromagnetism/magnetic-hysteresis.html. [Accessed: August 25, 2014].

[45] STMicroelectronics. (2000, January). L298 Dual Full Bridge Driver - STMicroelectronics. [Online], from STMicroelectronics: http://www.st.com/stwebui/ static/technical/document. [Accessed: June 15, 2014].

[46] Hausmair, K., Chi, S., Singerl, P. and Vogel, C., 2013. Aliasing-free digital pulse-width modulation for burst-mode RF transmitters. *IEEE Transactions on Circuits and Systems I: Regular Papers*, *60*(2), pp.415-427.

[47] Jain, V.K., 2009. *Advanced machining processes*. Allied publishers.

[48] Ganguly, V., Schmitz, T., Graziano, A. and Yamaguchi, H., 2013. Force Measurement and Analysis for Magnetic Field–Assisted Finishing. *Journal of Manufacturing Science and Engineering*, *135*(4), p.041016.

[49] Kala, P. and Pandey, P.M., 2014. Experimental study on finishing forces in double disk magnetic abrasive finishing process while finishing paramagnetic workpiece. *Procedia Materials Science*, *5*, pp.1677-1684.

[50] Tatarkin, E., Ikonnikov, A., Schrayner, T. and Grebenkov, R., 2015. Modeling of the Magnetic Abrasive Machining Process of Flat Surface Workpieces on Numerically Controlled Machine Tools. In *Applied Mechanics and Materials* (Vol. 788, pp. 69-74). Trans Tech Publications.

[51] Mishra, V., Goel, H., Mulik, R.S. and Pandey, P.M., 2014. Determining work-brush interface temperature in magnetic abrasive finishing process. *Journal of Manufacturing Processes*, *16*(2), pp.248-256.

[52] Kumar, G. and Yadav, V., 2009. Temperature distribution in the workpiece due to plane magnetic abrasive finishing using FEM. *The International Journal of Advanced Manufacturing Technology*, *41*(11-12), pp.1051-1058.

[53] Hou ZB, Komanduri R. Magnetic field assisted finishing of ceramics – part III. On the thermal aspects of magnetic abrasive finishing (MAF) of ceramic rollers. J Tribol (ASME) 1998; 120: 660 –7.

[54] Mishra, V., Goel, H., Mulik, R.S. and Pandey, P.M., 2014. Determining work-brush interface temperature in magnetic abrasive finishing process. *Journal of Manufacturing Processes*, *16*(2), pp.248-256.

[55] Furlani, E.P., 2001. *Permanent magnet and electromechanical devices: materials, analysis, and applications*. Academic press.

[56] Jha, S. and Jain, V., 2006. Modeling and simulation of surface roughness in magnetorheological abrasive flow finishing (MRAFF) process. *Wear*, *261*(7-8), pp.856-866.

[57] Nathan Ida, Engineering Electromagnetics, Springer, New York, 2004 (Chapter 9).

[58] Tumanski, S., 2007. Induction coil sensors—A review. *Measurement Science and Technology*, *18*(3), p.R31.

[59] D. Bruce Montgomery, Solenoid Magnet Design: *The Magnetic and Mechanical Aspects of Resistive and Superconducting Systems.* Wiley and Interscience, 1969.

[60] Zalnezhad, E., Sarhan, A.A. and Hamdi, M., 2013. A fuzzy logic based model to predict surface hardness of thin film TiN coating on aerospace AL7075-T6 alloy. *The International Journal of Advanced Manufacturing Technology*, *68*(1-4), pp.415-423.

[61] Mulay, L.N., 1963. Magnetic Susceptibility. *Wiley-Interscience, New York.*

[62] Jefimenko, O.D., 1966. Electricity and magnetism. *Appleton-Century-Crofts, New York.*

[63] Yin, S. and Shinmura, T., 2004. A comparative study: polishing characteristics and its mechanisms of three vibration modes in vibration-assisted magnetic abrasive polishing. *International Journal of Machine Tools and Manufacture*, *44*(4), pp.383-390.

[64] Mulik, R.S. and Pandey, P.M., 2012. Experimental investigations and modeling of finishing force

and torque in ultrasonic assisted magnetic abrasive finishing. *Journal of Manufacturing Science and Engineering*, *134*(5), p.051008.

[65] Wu, D., Jang, J.S.C. and Nieh, T.G., 2016. Elastic and plastic deformations in a high entropy alloy investigated using a nanoindentation method. *Intermetallics*, *68*, pp.118-127.

[66] Cheneler, D. and Bowen, J., 2013. Degradation of polymer films. *Soft Matter*, *9*(2), pp.344-358.

[67] Yoshida, M., Sumomogi, T., Endo, T., Maeta, H. and Kino, T., 2007. Nanoscale evaluation of strength and deformation properties of ultrahigh-purity aluminum. *Materials transactions*, *48*(1), pp.1-5.

[68] Unune, D.R., Barzani, M.M., Mohite, S.S. and Mali, H.S., 2018. Fuzzy logic-based model for predicting material removal rate and average surface roughness of machined Nimonic 80A using abrasive-mixed electro-discharge diamond surface grinding. *Neural Computing and Applications*, *29*(9), pp.647-662.

[69] Maher, I., Ling, L.H., Sarhan, A.A. and Hamdi, M., 2015. Improve wire EDM performance at different machining parameters-ANFIS modeling. *IFAC-PapersOnLine*, *48*(1), pp.105-110.

[70] Zalnezhad, E. and Sarhan, A.A., 2014. A fuzzy logic predictive model for better surface roughness of Ti–TiN coating on AL7075-T6 alloy for longer fretting fatigue life. *Measurement*, *49*, pp.256-265.

[71] Ooi, M.E., Sayuti, M. and Sarhan, A.A., 2015. Fuzzy logic-based approach to investigate the novel uses of nano suspended lubrication in precise machining of aerospace AL tempered grade 6061. *Journal of Cleaner Production*, *89*, pp.286-295.

[72] Lo, S.P., 2003. An adaptive-network based fuzzy inference system for prediction of workpiece surface roughness in end milling. *Journal of Materials Processing Technology*, *142*(3), pp.665-675.

[73] Ramesh, S., Karunamoorthy, L. and Palanikumar, K., 2008. Fuzzy modeling and analysis of machining parameters in machining titanium alloy. *Materials and Manufacturing Processes*, *23*(4), pp.439-447.

[74] Kanish, T.C., Kuppan, P., Narayanan, S. and Ashok, S.D., 2014. A fuzzy logic based model to predict the improvement in surface roughness in magnetic field assisted abrasive finishing. *Procedia Engineering*, *97*, pp.1948-1956.

[75] Fard, R.K., Afza, R.A. and Teimouri, R., 2013. Experimental investigation, intelligent modeling and multi-characteristics optimization of dry WEDM process of Al–SiC metal matrix composite. *Journal of Manufacturing Processes*, *15*(4), pp.483-494.

[76] Barzani, M.M., Zalnezhad, E., Sarhan, A.A., Farahany, S. and Ramesh, S., 2015. Fuzzy logic based model for predicting surface roughness of machined Al–Si–Cu–Fe die casting alloy using different additives-turning. *Measurement*, *61*, pp.150-161.

[77] Weng, W.C., Yang, F. and Elsherbeni, A., 2007. Electromagnetics and antenna optimization using Taguchi's method. *Synthesis Lectures on Computational Electromagnetics*, *2*(1), pp.1-94.

[78] Singh, A., Datta, S. and Mahapatra, S.S., 2011. Application of TOPSIS in the Taguchi method for optimal machining parameter selection. *Journal for Manufacturing Science & Production*, *11*(1-3), pp.49-60.

[79] Garibaldi, J.M. and John, R.I., 2003, May. Choosing membership functions of linguistic terms. In *Fuzzy Systems, 2003. FUZZ'03. The 12th IEEE International Conference on*(Vol. 1, pp. 578-583). IEEE.

[80] Shabgard, M.R., Badamchizadeh, M.A., Ranjbary, G. and Amini, K., 2013. Fuzzy approach to select machining parameters in electrical discharge machining (EDM) and ultrasonic-assisted EDM processes. *Journal of Manufacturing Systems*, *32*(1), pp.32-39.

[81] Bouchon-Meunier, B., Dotoli, M. and Maione, B., 1996. On the choice of membership functions in a mamdani-type fuzzy controller.

[82] Zimmermann, H.J., 1996. Fuzzy control. In *Fuzzy Set Theory—and Its Applications* (pp. 203-240). Springer, Dordrecht.

[83] Tseng, T.L.B., Konada, U. and Kwon, Y.J., 2016. A novel approach to predict surface roughness in machining operations using fuzzy set theory. *Journal of Computational Design and Engineering*, *3*(1), pp.1-13.

[84] Li, W., Li, X., Yang, S. and Li, W., 2018. A newly developed media for magnetic abrasive finishing process: material removal behavior and finishing performance. *Journal of Materials Processing Technology*.

[85] Chen, Y. and McIntyre, P.C., 2007. Lead zirconate titanate ferroelectric thin film capacitors: effects of surface treatments on ferroelectric properties. *Applied Physics Letters*, *91*(7), p.072910.

[86] Kang, C.W. and Huang, H., 2017. Deformation, failure and removal mechanisms of thin film structures in abrasive machining. *Advances in Manufacturing*, *5*(1), pp.1-19.

[87] Kim, T.W., Kang, D.M. and Kwak, J.S., 2010. Application of magnetic abrasive polishing to composite materials. *Journal of mechanical science and technology*, *24*(5), pp.1029-1034.

[88] Al-Saedi, H., Abdel-Wahab, W.M., Gigoyan, S., Taeb, A. and Safavi-Naeini, S., 2017. A low-cost wideband phase shifter for two-way mm-wave phased array antenna system. *International Journal of Microwave and Wireless Technologies*, pp.1-10.

[89] Sooraj, V.S. and Radhakrishnan, V., 2014. Fine finishing of internal surfaces using elastic abrasives. *International Journal of machine tools and manufacture*, *78*, pp.30-40.

[90] Takebayashi, Y., Hirogaki, T., Aoyama, E., Ogawa, K. and Melkote, S.N., 2014. Application of Magnetic Polishing With Ball Nose Shaped Tool for Microchannel Shape. *Journal of Micro and Nano-Manufacturing*, *2*(2), p.021009.

[91] Wang, Y., Wu, Y. and Nomura, M., 2016. Feasibility study on surface finishing of miniature V-grooves with magnetic compound fluid slurry. *Precision Engineering*, *45*, pp.67-78.

[92] "Sources of magnetic fields," web.mit.edu, n. d. [Online], pages 7 - 9, 35 – 39. Available: https://ocw.mit.edu/, (MIT open courseware) [Accessed: February, 2018].

[93] Dombroski, D.M., "Feasibility study of ferromagnetic particulate path diversion in additive manufacturing," M. A. Sc. thesis, MME, Univ. of Waterloo, Waterloo, ON, Canada, 2018, [Available in UWSpace, http://hdl.handle.net/10012/13209].

[94] J. Simpson, J. Lane, C. Immer, R. Youngquist, "Simple analytic expressions for the magnetic field of a circular current loop," *ntrs.nasa.gov*, January 1, 2001. [NASA technical reports server, Online]. Available: https://ntrs.nasa.gov/search.jsp?R=20010038494. [Accessed: February, 2018].

Appendix A

List of Publications

- Al-Dulaimi, T. and Khamesee, M.B., 2016, June. Formation and Control of a Rotating Magnetic Field in Magnetic Abrasive Finishing. In *ASME 2016 Conference on Information Storage and Processing Systems* (pp. V001T07A005-V001T07A005). American Society of Mechanical Engineers.
- Al-Dulaimi, T. and Khamesee, M.B., 2017. A stationary apparatus of magnetic abrasive finishing using a rotating magnetic field. *Microsystem Technologies*, *23*(11), pp.5185-5191.
- Al Mashagbeh, M., Al-Dulaimi, T. and Khamesee, M.B., 2017. Design and optimization of a novel magnetically-actuated micromanipulator. *Microsystem Technologies*, *23*(8), pp.3589-3600.

Papers under Review

- Al-Dulaimi, T. Al Mashagbeh, M. and Khamesee, M.B., A Novel Surface Finishing Approach Using a Stationary Magnetic Abrasive Finishing Apparatus. Submitted to the *International Journal of Machining and Machinability of Materials.*
- Al-Dulaimi, T. and Khamesee, M.B., A Prediction Model for the Average Surface Roughness and Reduction Percentage of Surface Roughness in Stationary Apparatus of Magnetic Abrasive Finishing. Submitted to the *Journal of Manufacturing Processes*.

Appendix B

On-axis and off-axis Magnetic Field Formula

B.1. On-axis of a single loop

The magnetic field at a distance ***z***, on the axis of a single loop of wire, with radius ***a***, carrying a current of ***I*** is presented, as illustrated in Figure A.1 [92].

$$B = \frac{\mu_0 I a^2}{2(a^2 + z^2)^{3/2}} \tag{B. 1}$$

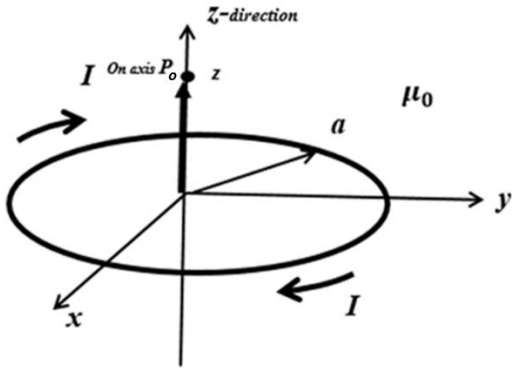

Figure B.1: Schematic of a single current loop on-axis geometry [93].

B.2. On-axis of a multi-turn single layer solenoid

Applying Biot-Savart to a multi-turn single layer solenoid of length (*l*) and number of turns (*N*), as shown in Figure B.2:

$$dB = \hat{z}\frac{\mu_0 \frac{NI}{l} a^2}{2[a^2 + (z - z')^2]^{3/2}} dz' \tag{B. 2}$$

The quantity of current flowing through a loop having a thickness dz'at a height $z'$is dI.

$$dI = I\left(\frac{N}{l}\right) dz' \tag{B. 3}$$

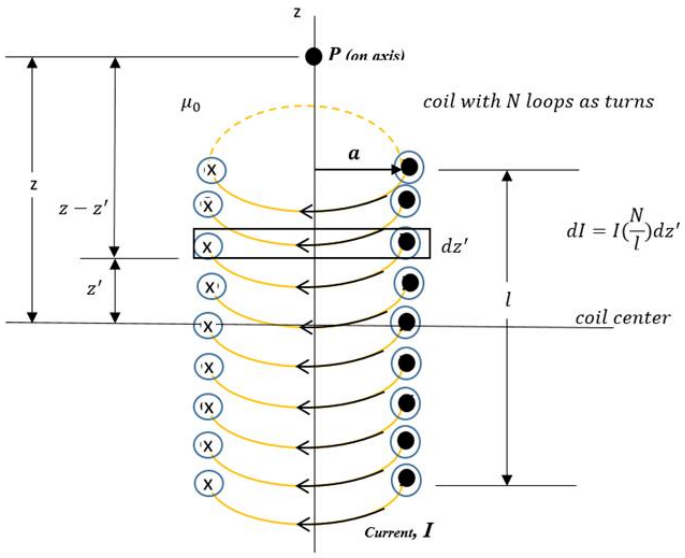

Figure B.2: Schematic of a multi-turn coil geometry [93].

The integration of equation (B.2) is:

$$B = \hat{z} \int_{-l/2}^{l/2} \frac{\mu_0 \frac{NI}{l} a^2}{2[a^2 + (z - z')^2]^{3/2}} dz' = \hat{z}\mu_0 \frac{NI}{2l} a^2 \int_{-l/2}^{l/2} \frac{dz'}{[a^2 + (z - z')^2]^{3/2}} \quad \text{(B. 4)}$$

B.3. Off-axis of a single loop

To quantify the magnitude of the magnetic field of a point located off-axis of a single loop, many analytical approaches can be used, such as Spherical and Elliptical approaches.

- Spherical

As illustrated in Figure A.3, a circular loop of radius ***R*** lying in the ***x-y*** plane carrying a steady current ***I***, the magnetic field at point $\boldsymbol{P_o}$ off the axis of symmetry is of interest.

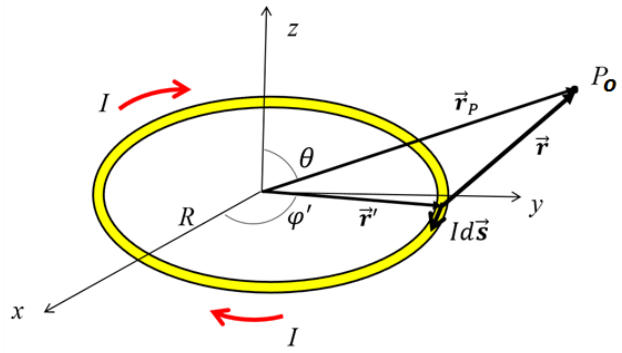

Figure B.3: Schematic of a single current loop magnetic field off axis of symmetry [92].

$$B_r = \frac{\mu_0 I R^2 \cos\theta}{4\pi} \int_0^{2\pi} \frac{d\varphi'}{(R^2 + r^2 - 2rR\sin\theta\sin\varphi')^{3/2}} \tag{B.5}$$

$$B_\theta(r,\theta) = \frac{\mu_0 I R}{4\pi} \int_0^{2\pi} \frac{(r\sin\varphi' - R\sin\theta)d\varphi'}{(R^2 + r^2 - 2rR\sin\theta\sin\varphi')^{3/2}} \tag{B.6}$$

The variable r is defined as follows with θ and φ' as shown in Figure B.3.

$$r = |\vec{r}| = \sqrt{(-R\cos\varphi')^2 + (y - R\sin\varphi')^2 + z^2} = \sqrt{R^2 + y^2 + z^2 - 2yR\sin\varphi'} \tag{B.7}$$

- Elliptic

To describe the magnetic field of point $\boldsymbol{P_o}$ as illustrated in Figure B.1 according to the complete elliptical integrals, the magnetic field components are [94]:

$$B_x = \frac{Cxz}{2\alpha^2\beta\rho^2}[(a^2 + r^2)E(k^2) - \alpha^2 K(k^2)] \tag{B.8}$$

$$B_y = \frac{Cyz}{2\alpha^2\beta\rho^2}[(a^2 + r^2)E(k^2) - \alpha^2 K(k^2)] = \frac{y}{x}B_x \tag{B.9}$$

$$B_z = \frac{C}{2\alpha^2\beta}[(a^2 - r^2)E(k^2) + \alpha^2 K(k^2)] \tag{B.10}$$

where $K(k^2)$ is the complete elliptic integral function, of the first kind, and $E(k^2)$ is the complete elliptic integral function, of the second kind and the following substitutions were made for simplicity:

$$\rho^2 \equiv x^2 + y^2 \tag{B.11}$$

$$r^2 \equiv x^2 + y^2 + z^2 \tag{B.12}$$

$$\alpha^2 \equiv a^2 + r^2 - 2a\rho \tag{B.13}$$

$$\beta^2 \equiv a^2 + r^2 + 2a\rho \tag{B.14}$$

$$k^2 \equiv 1 - \frac{\alpha^2}{\beta^2} \tag{B.15}$$

$$\gamma \equiv x^2 - y^2, from\ which\ \rho \geq 0, r \geq 0 \tag{B.16}$$

$$C \equiv \mu_0 \frac{I}{\pi}, from\ which\ \rho \geq 0, r \geq 0 \tag{B.17}$$

Appendix C
Experimental results for L9 Taguchi approach

Experimental results for L9 Taguchi approach, repeating each set of input parameters 3 times. The output results of the surface roughness for each trial are (Ra_1, Ra_2, and Ra_3). Rs_o represents the initial value of the surface roughness before the finishing process. *Ra* represents the average surface roughness of the 3 trials.

Table C.1: Experimental results of L9 Taguchi approach.

No.	*App. Volt.*	*Freq. Hz*	*Time min*	*Par. Size µm*	RS_0 *µm*	Ra_1 *µm*	Ra_2 *µm*	Ra_3 *µm*	*Ra µm*
1	20	2	15	100	11.6212	7.9376	7.4885	9.0607	8.1623
2	20	6	30	75	11.3981	8.6488	8.1344	8.8149	8.5327
3	20	10	60	37	12.1763	8.4085	9.0425	6.8964	8.1158
4	25	2	30	37	11.9318	7.4253	6.9902	8.4763	7.6306
5	25	6	60	100	12.1380	9.3871	6.8430	6.8390	7.6897
6	25	10	15	75	10.9118	7.9248	7.8167	7.8090	7.8501
7	30	2	60	75	12.3555	5.6026	5.6124	7.4361	6.2170
8	30	6	15	37	12.7799	7.9763	7.8970	8.4355	8.1030
9	30	10	30	100	12.3535	7.4237	6.3139	8.8926	7.5434